Using atmospheric observations to quantify annual biogenic carbon dioxide fluxes on the Alaska North Slope

Luke D. Schiferl[1,2], Jennifer D. Watts[3], Erik J. L. Larson[4], Kyle A. Arndt[3,5,6], Sébastien C. Biraud[7], Eugénie S. Euskirchen[8], Jordan P. Goodrich[5,9], John M. Henderson[10~~9~~], Aram Kalhori[5,11], Kathryn McKain[12~~10~~,13~~11~~], Marikate E. Mountain[10~~9~~], J. William Munger[2], Walter C. Oechel[5,14~~12~~], Colm Sweeney[12~~10~~], Yonghong Yi[15~~13~~,16~~14~~], Donatella Zona[5,17~~15~~], and Róisín Commane[1,18~~16~~]

[1]Lamont-Doherty Earth Observatory, Columbia University, Palisades, New York, USA.
[2]Harvard John A. Paulson School of Engineering and Applied Sciences, Cambridge, Massachusetts, USA.
[3]Woodwell Climate Research Center, Falmouth, Massachusetts, USA.
[4]Department of Organismic and Evolutionary Biology, Harvard University, Cambridge, Massachusetts, USA.
[5]Department of Biology, San Diego State University, San Diego, California, USA.
[6]Earth Systems Research Center, Institute for the Study of Earth, Oceans, and Space, University of New Hampshire, Durham, New Hampshire, USA.
[7]Lawrence Berkeley National Laboratory, Berkeley, California, USA.
[8]Institute of Arctic Biology, University of Alaska Fairbanks, Fairbanks, Alaska, USA.
[9]Ministry for the Environment, Wellington, New Zealand.
[10~~9~~]Atmospheric and Environmental Research, Inc., Lexington, Massachusetts, USA.
[11]GFZ German Research Centre for Geosciences, Potsdam, Germany.
[12~~10~~]Global Monitoring Laboratory, Earth System Research Laboratories, NOAA, Boulder, Colorado, USA.
[13~~11~~]Cooperative Institute for Research in Environmental Sciences, University of Colorado, Boulder, Colorado, USA.
[14~~12~~]Department of Geography, University of Exeter, Exeter, United Kingdom.
[15~~13~~]Joint Institute for Regional Earth System Science and Engineering, University of California, Los Angeles, California, USA.
[16~~14~~]College of Surveying and Geo-Informatics, Tongji University, Shanghai, China.
[17~~15~~]Department of Animal and Plant Sciences, University of Sheffield, Western Bank, Sheffield, United Kingdom.
[18~~16~~]Department of Earth and Environmental Sciences, Columbia University, New York, New York, USA.

Correspondence to: Luke D. Schiferl (schiferl@ldeo.columbia.edu)

Abstract. The continued warming of the Arctic could release vast stores of carbon into the atmosphere from high-latitude ecosystems, especially from thawing permafrost. Increasing uptake of carbon dioxide (CO_2) by vegetation during longer growing seasons may partially offset such release of carbon. However, evidence of significant net annual release of carbon from site-level observations and model simulations across tundra ecosystems has been inconclusive. To address this knowledge gap, we combined top-down observations of atmospheric CO_2 concentration enhancements from aircraft and a tall tower, which integrate ecosystem exchange over large regions, with bottom-up observed CO_2 fluxes from tundra environments and found that the Alaska North Slope is not a consistent net source or net sink of CO_2 to the atmosphere (ranging from –6 to +6 TgC yr^{-1} for 2012–2017). Our analysis suggests that significant biogenic CO_2 fluxes from unfrozen terrestrial soils, and likely inland waters, during the early cold season (September–December) are major factors in determining the net annual carbon balance of the North Slope, implying strong sensitivity to the rapidly warming freeze-up period. At the regional level, we find no evidence for previously reported large late cold season (January–April) CO_2 emissions to the atmosphere during the study

period. Despite the importance of the cold season CO_2 emissions to the annual total, the interannual variability of the net CO_2 flux is driven by the variability in growing season fluxes. During the growing season, the regional net CO_2 flux is also highly sensitive to the distribution of tundra vegetation types throughout the North Slope. This study shows that quantification and characterization of year-round CO_2 fluxes from the heterogeneous terrestrial and aquatic ecosystems in the Arctic using both site-level and atmospheric observations is important to accurately project the earth system response to future warming.

1 Introduction

The Arctic surface air temperature is warming at twice the rate of the global average (Box et al., 2019; Meredith et al., 2019). Continued thawing of Arctic permafrost has the potential to release vast stores of carbon into the atmosphere, thereby further accelerating warming (Schuur et al., 2015; Hugelius et al., 2014). In the biosphere, the net CO_2 flux is the balance between uptake of CO_2 by vegetation through photosynthesis (negative net CO_2 flux indicates removal from the atmosphere) and release of CO_2 into the atmosphere by plant and microbial respiration (positive net CO_2 flux indicates a source to the atmosphere). Arctic growing seasons are short (~3 months), and the long, cold season dominates the seasonal cycle. The transition between the growing and cold seasons is marked by the soil zero-curtain period, when belowground temperatures of the active layer above frozen permafrost remain near freezing; the active layer is insulated by snow and ice at the surface and warmed by the latent heat release of freezing water (Outcalt et al., 1990). During the zero-curtain period, soil respiration can remain active in deeper soils for weeks to months after the end of the growing season (Zona et al., 2016; Romanovsky and Osterkamp, 2000). As the climate warms, the active layer above permafrost deepens, thawed soils become wetter, a larger volume of soil remains unfrozen for a longer period of time, and the duration of the zero-curtain period plays an increasingly important role in determining the net carbon exchange in Arctic ecosystems (Kim et al., 2012; Arndt et al., 2019). Recent work has shown a significant cold season source of CO_2 from Arctic ecosystems, including more than 70% increase in October–December CO_2 concentration enhancements in the past 40 years, consistent with an increase in cold season respiration, which is not well represented in earth system models (Commane et al., 2017; Natali and~~&~~ Watts et al., 2019). Neglecting these processes could lead to large underestimation of CO_2 emissions, biasing current and future climate projections.

Tundra ecosystems, characterized by frozen soils covered in low shrubs, sedges, grasses, and mosses, make up approximately 50% of the Arctic landscape (Raynolds et al., 2019). Lacking trees, the magnitude of net CO_2 uptake in tundra during the growing season is relatively small and may be offset by emissions from respiration that can continue well into the cold season (Watts et al., 2021). In the past, year-round CO_2 flux measurements from tundra ecosystems were rare due to difficulties in maintaining instrumentation under remote and extreme cold conditions (Euskirchen et al., 2017; Kittler et al., 2017; Goodrich et al., 2016). Long-term year-round CO_2 concentration measurements have been made in the Arctic at a small number of tall towers, which have been situated to sample clean marine air off the ocean (Jeong et al., 2018; Worthy et al., 2009). While aircraft provide greater spatial coverage over land than these towers, they tend to operate for short durations, and their temporal coverage is limited by weather and visibility during the cold season (Chang et al., 2014; Commane et al., 2017;

Miller et al., 2016). However, the recent increase in availability of observations of gas fluxes and concentrations within a particular tundra region, the Alaska North Slope (Fig. 1a), is making it possible to better conduct year-round multi-scale assessments of tundra ecosystems, with the aim of improving our understanding of CO_2 sink/source activity and carbon budgets in these environments.

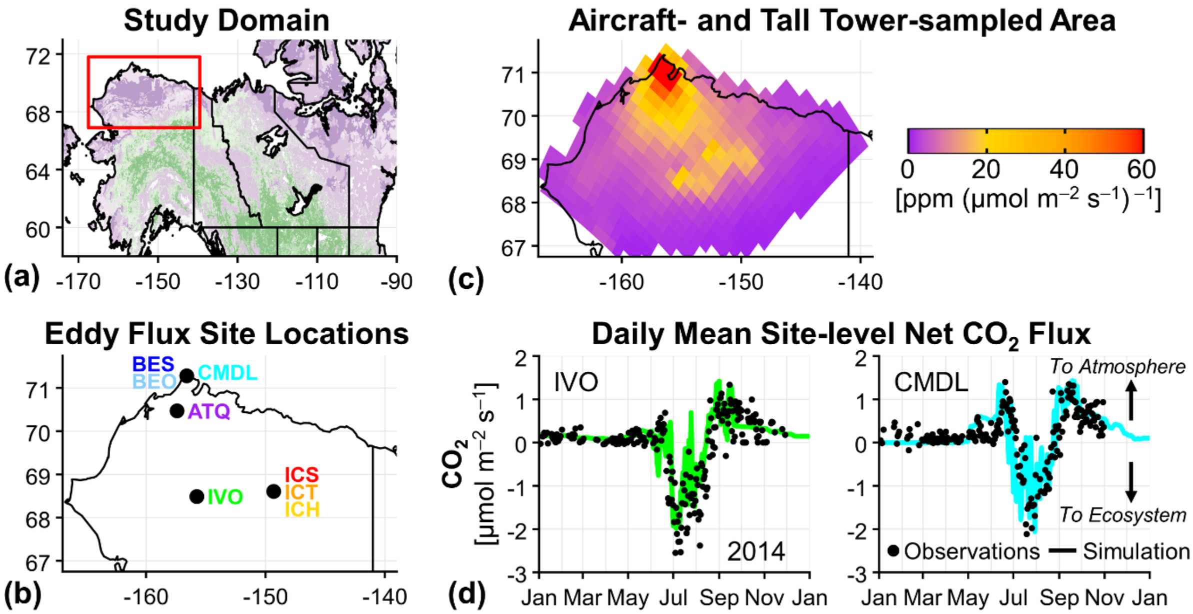

Figure 1. Alaska North Slope study region, eddy flux site locations, area sampled by aircraft and tower, and example results from the eddy flux site measurement-model comparison. **(a)** North Slope region (red box) within Alaska and northwestern Canada. Tundra areas shown in purple and boreal forest areas shown in green (Luus et al., 2017). **(b)** Location of eddy flux measurement sites on the Alaska North Slope used in this analysis. **(c)** Ten-day WRF-STILT footprints used to sample CO_2 flux models, summed for all aircraft and tall tower CO_2 observations used in this analysis. Colors represent values greater than 0 and are saturated at 60 ppm (μmol m^{-2} s^{-1})$^{-1}$. Maximum value near Utqiaġvik, Alaska is 324 ppm (μmol m^{-2} s^{-1})$^{-1}$. **(d)** Timeseries of observed (black dots) and simulated (colored lines) site-level daily mean net CO_2 flux for 2014 at IVO (left) and CMDL (right) eddy flux measurement sites, where site-level TVPRM net CO_2 flux simulations are driven by NARR meteorology and the CSIF SIF product. Positive net CO_2 flux values indicate CO_2 fluxes into the atmosphere throughout this study. A comparison for all eight eddy flux sites is provided in Fig. S1 in Supplement.

Currently, observations and models do not agree on the sign of the annual net CO_2 flux across the Alaska North Slope region. Site-level measurements and atmospheric observations suggest this region is a net CO_2 source (Commane et al., 2017; Oechel et al., 2014; Euskirchen et al., 2017). However, a comparison of process-based models of the North Slope found large variability in the sign and magnitude of the net CO_2 flux with an approximately neutral regional annual net CO_2 flux multi-model mean of –3.5 ± 67 TgC yr^{-1} (Fisher et al., 2014). In a more recent study, Tao et al. (2021) found an annual net CO_2 flux range of –9 to 12 TgC yr^{-1} for the years 2010–2016, with only 2014 being an annual net CO_2 source. Extrapolating from site-level CO_2 flux measurements to regional budgets is difficult due to the extreme heterogeneity of tundra ecosystems in the North Slope and a lack of spatial and seasonal representativeness by existing flux monitoring sites (Pallandt et al., 2022).

In this study, we compare *bottom-up* flux estimates with *top-down* atmospheric observations from aircraft and a tall tower using an integrated modeling approach to quantify the CO_2 budget sign and magnitude of the Alaska North Slope. Our framework first applies a bottom-up approach to understand Arctic tundra ecosystem CO_2 fluxes, constrained by site-level observations, using an empirical model ensemble of CO_2 fluxes derived from eddy flux measurements representing varied tundra ecosystems within the region. We then apply top-down information gained from regional CO_2 concentration enhancement observations measured by a tall tower and aircraft, which sample the atmosphere-biosphere exchange throughout the Alaska North Slope, to evaluate the range of potential CO_2 fluxes identified by the bottom-up model ensemble for 2012–2017. This evaluation also identifies the ecosystem parameterizations, vegetation distributions, and environmental drivers that best characterize the observed spatial and temporal distribution of biogenic CO_2 in the atmosphere across the region. By developing regional CO_2 budgets constrained by both atmospheric observations and ecosystem environmental responses, we can better project how Arctic tundra ecosystems will respond to climate change on annual and decadal timescales.

2 Materials and methods

2.1 Observed CO_2 concentrations and fluxes on the Alaska North Slope

2.1.1 Atmospheric CO_2 concentration observations

We use a suite of CO_2 concentration observations from various sources on the North Slope for our analysis. The United States (US) National Oceanic and Atmospheric Administration (NOAA) Barrow Atmospheric Baseline Observatory (BRW) tall tower near Utqiaġvik, Alaska has made continuous in situ CO_2 concentration measurements since 1973 (Sweeney et al., 2016). The US Department of Energy (DOE) Atmospheric Radiation Measurement Climate Research Facility Airborne Carbon Measurements V (ARM-ACME V) airborne campaign measured CO_2 concentrations sub-weekly from June to September 2015 over the North Slope (Biraud et al., 2016; Tadić et al., 2021). The US National Aeronautics and Space Administration (NASA) Arctic-Boreal Vulnerability Experiment (ABoVE) Arctic Carbon Atmospheric Profiles (Arctic-CAP) airborne campaign flew throughout Alaska and northwestern Canada approximately every month from May to November 2017 (Sweeney and McKain, 2019; Sweeney et al., 2022). CO_2 concentration observations from the NASA Carbon in Arctic Reservoirs Vulnerability Experiment (CARVE) flights for 2012–2014 are incorporated into the Commane et al. (2017) optimized CO_2 fluxes used in our analysis below. The NOAA/US Coast Guard collaborative Alaska Coast Guard (ACG) flights have also made aircraft CO_2 concentration measurements in the region, but these coastal flights observe only limited spatial coverage of the North Slope, and we do not use them here.

For the NOAA BRW tower, we use hourly CO_2 concentration observations with wind direction from the land (135°–202.5° clockwise w.r.t. north) and ocean sectors (0°–45°), avoiding Utqiaġvik anthropogenic activity, with wind speed > 2.5 m s^{-1} (Fig. S2) (Commane et al., 2017; Sweeney et al., 2016). We only use land sector observations from the cold season (defined here as September–April) since seasonal wind patterns do not favor transport from those directions during the growing season (defined here as May–August). For the ARM-ACME V and ABoVE Arctic-CAP aircraft campaign observations, we group averaged sampling points into 50 m vertical bins after removing data influenced by combustion sources such as anthropogenic activity and biomass burning events.~~,~~ These combustion sources of CO_2 are expected to be small (<1 TgC yr^{-1} on the North Slope, see Table S1) during our study period. They are not accounted for in biogenic CO_2 flux models, however, and must be removed from our analysis when observed.~~indicated by~~ We remove time periods with elevated~~ or varying~~ carbon monoxide (CO) concentration~~s~~ above 150 ppb, as in ~~(~~Chang et al.~~,~~ (2014) and ~~(~~Commane et al.~~,~~ (2017), which indicates local combustion sources. Time periods with highly variable CO concentrations (ΔCO > 40 ppb) indicate complex mixing of more remote combustion sources and are also removed (Chang et al., 2014). The~~se~~ remaining grouped sampling points correspond to the available Lagrangian atmospheric transport modeling system simulations (WRF-STILT (Henderson et al., 2015), see below): ARM-ACME V points are calculated every 50 m vertically below 1 km, every 100 m vertically above 1 km, and every 10 km horizontally from 1 s observations, and ABoVE Arctic-CAP points are matched every 20 s from averaged 10 s observations. To ensure these points observe the Alaska North Slope, we only use points with at least 70% of the total 10-day WRF-STILT simulated surface influence occurring in our regional domain.

2.1.2 Eddy covariance CO_2 flux tower observations

We also use up to five years (2013–2017) of year-round observations of net CO_2 flux from eight eddy covariance tower sites (for 32 total site-years) representing an array of tundra ecosystems throughout the Alaska North Slope (Figs. 1b, S1, Table S2~~1~~ in Supplement). These half-hourly eddy flux measurements of net CO_2 flux are not gap-filled to avoid introducing additional uncertainties. Three of the sites are located near Imnavait Creek along a wetness gradient from valley to hilltop: wet sedge tundra (ICS), moist acidic tussock tundra (ICT) and dry heath tundra (ICH) (Euskirchen et al., 2017, 2012). The other sites include tussock tundra at Ivotuk (IVO), wet polygonised tundra at Atqasuk (ATQ), and three sites near Utqiaġvik: wetland tundra (BES), wet polygonised tundra (BEO), and moist tundra (CMDL) (Zona et al., 2016; Arndt et al., 2020).

2.2 Observed atmospheric CO_2 concentration enhancement calculation

We calculate the observed *top-down* atmospheric CO_2 concentration enhancement (ΔCO_2) for the North Slope region for every land-sector hour at the NOAA BRW tower and for every 50 m of vertical distance transited during the airborne campaigns (ARM-ACME V, ABoVE Arctic-CAP). The observed ΔCO_2 [units: ppm] generated by the North Slope ecosystem is calculated relative to the background concentration without influence from this region such that:

$$\text{observed } \Delta CO_2 = \text{observed } [CO_2] - \text{background } [CO_2] \quad (1)$$

following previous work (Sweeney et al., 2016; Commane et al., 2017; Jeong et al., 2018).

The background CO_2 concentrations at the NOAA BRW tower are determined by smoothing the 10-day mean of the observed ocean sector concentrations using spline fitting to produce a daily CO_2 background concentration. We calculate the uncertainty of these background concentrations by both 1) varying the starting hour of the 10-day mean calculation prior to spline fitting and 2) randomly sub-selecting 50% the ocean sector concentrations 1000 times. The interval that contains 95% of these 240,000 fits represents our daily background uncertainty. Figure S2 shows the ocean sector concentrations, resulting background concentration, and uncertainty described here.

To determine the background CO_2 concentrations for the ARM-ACME V and ABoVE Arctic-CAP aircraft campaigns, we isolate aircraft observations without surface influence from the North Slope using the WRF-STILT footprints as done for larger regions in Chang et al. (2014) and Commane et al. (2017). These observed CO_2 concentrations represent the state of the air before it interacts with the surface in the study region. The regional backgrounds vary by the direction from which the air enters the domain. For example, the backgrounds from the south and from over land generally experience CO_2 drawdown prior to those from over the Arctic Ocean. The time- and directional-dependent backgrounds we use are shown in Fig. S3. We apply the uncertainty from the NOAA BRW tower background to the aircraft backgrounds as a reasonable representation of the variability associated with available background CO_2 concentration data.

2.3 Simulated atmospheric CO_2 concentration enhancement calculation

To understand how landscape interactions with the atmosphere (through CO_2 flux) influenced the observed CO_2 concentrations across space and time, we calculate the corresponding simulated ΔCO_2 [units: ppm] by transporting *bottom-up* biogenic CO_2 fluxes to each observation site such that:

$$\text{simulated } \Delta CO_2 = \text{simulated } CO_2 \text{ flux} \times \text{simulated footprint} \qquad (2)$$

In this calculation, we multiply the hourly simulated CO_2 flux [μmol CO_2 m^{-2} s^{-1}] by the footprint [ppm (μmol CO_2 m^{-2} s^{-1})$^{-1}$] for that hour starting at the observation point, backward in time for each hour up to ten days, where the footprint quantifies the influence of the land surface on the concentration observed at a measurement point. The simulated ΔCO_2 is then the sum of these hours.

We use expected CO_2 fluxes based on a variety of bottom-up model approaches which represent North Slope ecosystems. Year-round bottom-up estimates of net CO_2 fluxes (defined by the models as net ecosystem exchange, NEE) are obtained from the Tundra Vegetation Photosynthesis and Respiration Model (TVPRM) ensemble, and from existing model output from Luus et al. (2017) and Commane et al. (2017). Independent bottom-up estimates of belowground CO_2 emissions (= NEE) for the cold season (net CO_2 uptake = 0) were obtained from Natali and~~&~~ Watts et al. (2019) and Watts et al. (2021). The TVPRM model ensemble development process is described in Sect. 2.4, and the other CO_2 flux models, including their native spatial and temporal resolutions, are listed in Table S3~~2~~.

The footprints are generated by~~calculated from~~ the Lagrangian atmospheric transport modeling system, WRF-STILT (Stochastic Time-Inverted Lagrangian Transport model driven by Weather Research and Forecasting model meteorology (Henderson et al., 2015)). In this system, WRF meteorological fields are first generated for the study region and time period (v3.5.1 for ARM-ACME V and NOAA BRW tower footprints used here, v3.9.1 for ABoVE Arctic-CAP footprints). STILT then uses the WRF meteorology to estimate the contribution of surface fluxes to the atmospheric concentration at a specified time and place, called a receptor, by calculating the amount of time air (represented by a distribution of particles) spends in the lower half of the boundary layer at a given location. The WRF-STILT model configurations from ~~(~~Henderson et al.~~,~~ (2015) have been used extensively in numerous previous papers to study greenhouse gas fluxes using observations from aircraft and towers in Alaska, including on the North Slope (e.g., ~~(~~Chang et al., 2014; Miller et al., 2016; Zona et al., 2016; Commane et al., 2017; Karion et al., 2015; Hartery et al., 2018). An evaluation by ~~(~~Henderson et al.~~,~~ (2015) for WRF v.3.4.1 and v3.5.1 showed that their polar WRF configuration performs well against surface observations of air temperature and wind speed in Alaska and that WRF-STILT can capture the shape and approximate depth of greenhouse gases in the column. ~~(~~Zona et al.~~,~~ (2016) note that WRF planetary boundary layer ventilation rates may be biased in the fall (and winter) when heat fluxes are low, but this error is difficult to assess quantitatively. For this study, we use receptors set to correspond with the tower and aircraft CO_2 concentration observations. The footprints (and their corresponding measurements) for these receptors sample air from throughout the North Slope but are concentrated more heavily toward the area around the NOAA BRW tower (Fig. 1c).

For calculating simulated ΔCO_2 from the TVPRM ensemble, we grid the distribution of WRF-STILT particles and their corresponding surface influence to the spatial resolution of the meteorological reanalysis products driving the model. The CO_2 flux models used for comparison to the TVPRM ensemble are similarly treated using 0.5°-gridded 10-day WRF-STILT footprints, which are available on a circumpolar grid poleward of 30°N. The simulated CO_2 fluxes from Luus et al. (2017), Natali and~~&~~ Watts et al. (2019), and Watts et al. (2021) are regridded to 0.5° spatial resolution. For the models by Natali and~~&~~ Watts et al. (2019) and Watts et al. (2021), which only estimate monthly CO_2 fluxes, we apply a constant flux for that month. Since the ends of our defined cold season (September–April) include transitional periods when some biogenic plant activity does occur (hence belowground CO_2 emissions $\neq$ NEE), for the Natali and~~&~~ Watts et al. (2019) and Watts et al. (2021) bottom-up scenarios, we add in estimates of photosynthesis and plant respiration fluxes from the TVPRM ensemble for April and September.

2.4 Empirically simulated biogenic CO_2 fluxes from tundra ecosystems

We develop the TVPRM as an ensemble of ecosystem-resolved models that represent a more extensive range of potential tundra ecosystem functional relationships, environmental drivers, and scaling assumptions than available from other CO_2 flux models. For this study, TVPRM generates a set of spatially and temporally varying CO_2 flux maps for a six-year period (2012–2017) at 30 × 30 km spatial and 1 hr temporal resolution for the Alaska North Slope.

TVPRM is driven by parameterized functional relationships for soil respiration (R_{soil}), plant respiration (R_{plant}), and photosynthesis (gross primary productivity (GPP)), which are described by:

$$R_{soil} = \alpha_s \times T_s + \beta_s \tag{3}$$

$$R_{plant} = \alpha_a \times T_a + \beta_a \tag{4}$$

$$GPP = \lambda \times T_{scale} \times SIF \times PAR \times \frac{1}{1+\frac{PAR}{PAR_0}} \tag{5}$$

$$T_{scale} = \frac{(T_a - T_{min})(T_a - T_{max})}{(T_a - T_{min})(T_a - T_{max}) - (T_a - T_{opt})^2} \tag{6}$$

The simulated hourly CO_2 fluxes [units: µmol CO_2 m^{-2} s^{-1}] are determined as responses to light and heat: R_{soil} is a function of near-surface soil temperature (T_s) [°C]; R_{plant} is a function of air temperature (T_a) [°C]; and GPP is a function of a temperature scalar (T_{scale}) and photosynthetically active radiation (PAR) [µmol photon m^{-2} s^{-1}], with solar-induced chlorophyll fluorescence

(SIF) [mW m^{-2} nm^{-1} sr^{-1}] used to define the seasonal cycle of photosynthetic capacity. T_s depths are determined by reanalysis product and listed in Table S4~~3~~. T_{scale} ranges from 0 to 1 based on the position of T_a on the continuum between minimum temperature (T_{min} = 0°C), maximum temperature (T_{max} = 40°C), and optimal temperature (T_{opt} = 15°C). NEE is then calculated as:

$$NEE = R_{soil} + R_{plant} - GPP \quad (7)$$

with positive NEE values indicating a net source of CO_2 into the atmosphere and negative NEE values meaning net movement of CO_2 into the biosphere. We use NEE to be synonymous with net CO_2 flux. Using SIF, which correlates to photosynthetic activity (Porcar-Castell et al., 2014; Yang et al., 2015), in the modeling framework provides an advantage over indices such as enhanced vegetation index (EVI) due to the limited canopy and evergreen nature of tundra ecosystems (Luus et al., 2017).

The parameter values (α_s, β_s, α_a, β_a, λ, PAR_0) for the site-level relationships used by TVPRM are determined first using the observed net CO_2 fluxes from the eddy flux sites (see Sect. S1 in Supplement). We determine the site-level parameters separately for each combination of reanalysis product (NARR (Mesinger et al., 2006) and ERA5 (Hersbach et al., 2020)), which provide T_a, T_s, and PAR, and SIF product (GOME-2 (Joiner et al., 2016), GOSIF (Li and Xiao, 2019), and CSIF (Zhang et al., 2018)) that will later be used to generate the regional TPVRM ensemble (Tables S4~~3~~–S5~~4~~, see Sects. S2–S3). Additional α_s and β_s parameters are determined using T_s from the Remote Sensing driven Permafrost Model (RS-PM (Yi et al., 2019, 2018)) to test its implementation in TPVRM. RS-PM uses tailored input for Alaska permafrost zones, such as downscaled snow depth and aircraft-observed soil dielectric constants and was developed and tested using T_s and active layer thickness measurements from the North Slope. RS-PM also produces T_s at higher vertical resolution in the near-surface than the reanalysis products to capture subsurface heterogeneity in unfrozen soil, ~~includes drivers and processes such as soil moisture and snow cover that more explicitly control the T_s throughout the soil column~~ which is important to ~~better~~ represent the zero-curtain throughout the freezing and thawing periods in Alaska~~than the reanalysis products~~.

Using the median parameter value sets for each site, we simulate the TVPRM net CO_2 flux for our study period at every site location to perform a cross-site evaluation (Fig. S1). These simulated net CO_2 fluxes perform well against the net CO_2 flux observations at their corresponding sites (Figs. 1d, S4, see Sect. S4). This process also identifies two distinct ecosystem groups: "inland", predominately graminoid and shrub tundra (ICS, ICT, ICH, IVO), and "coastal", predominately wetland tundra (ATQ, BES, BEO, CMDL), based on the similar simulated CO_2 flux responses to the meteorology- and SIF-determined functional relationships within each group demonstrated by the cross-site evaluation (Fig. S1).

The net CO_2 flux for each meteorological grid box in our study domain is then calculated using the site-level functional relationships for both tundra groups. These fluxes are weighted by the spatial distribution of inland and coastal tundra from three different vegetation maps (CAVM (Walker et al., 2005), RasterCAVM (Raynolds et al., 2019), and ABoVE LC (Wang et al., 2020), Fig. S5, Table S6~~5~~, see Sect. S5) to produce the regionally scaled TVPRM net CO_2 flux. By varying the choice of representative inland and coastal tundra sites, meteorological reanalysis product, vegetation map, and SIF product, we generate 288 different simulations (members) of net CO_2 flux (referred to here as the unconstrained TVPRM ensemble) for each grid box across the region for each of the six study years. Monthly and annual regional net CO_2 flux values are calculated as the area-weighted sum of all grid boxes simulated in our domain. Notable changes since the previous iteration of this empirical CO_2 flux model (Commane et al., 2017; Luus et al., 2017) include the expansion of the model to include multiple ensemble members to account for variability and uncertainty in model formulation, the use of additional site-years of CO_2 flux observations (with increased data coverage over the cold season), more inclusive data filtering methods, and much higher temporal (1-, 4-, and 8-day rather than monthly) and spatial (0.01° and 0.05° rather than 0.5°) resolution SIF datasets. We compare TVPRM to the previous model version by Luus et al. (2017) and its CARVE-informed optimization by Commane et al. (2017) in Sect. 3.3.

2.5 Evaluation Framework

We use the atmospheric CO_2 concentration observations to evaluate the many tundra ecosystem parameterizations, vegetation distributions, and environmental drivers that represent the net CO_2 flux on the North Slope over various spatial and temporal scales. For this assessment, we compare the observed ΔCO_2, which are the observed CO_2 concentration changes driven by regional CO_2 fluxes, with the simulated ΔCO_2 determined by combining the regional biogenic CO_2 flux models with the atmospheric transport model.

To compare the regional observed ΔCO_2 and simulated ΔCO_2, we calculated the coefficient of determination (R^2) as the square of the Pearson correlation coefficient for all points. The slope (m) is determined by ordinary least squares using the median of each 10% bin of ordered observed and corresponding simulated net CO_2 flux. The normalized mean bias (NMB) of all points is defined as $\frac{\sum(\text{simulated} - \text{observed})}{\sum \text{observed}}$. The root-mean-square error (RMSE) of all points is defined as $\sqrt{(\text{simulated} - \text{observed})^2}$.

These comparisons enable us to constrain the regional net CO_2 flux on the Alaska North Slope. First, we identify the year-round empirically driven net CO_2 fluxes from the TVPRM ensemble (TVPRM Unconstrained) which are most consistent with the CO_2 concentration observations from the two aircraft campaigns and at the tower (TVPRM Constrained) (Sects. 3.1–3.2). Then, noting the large range in potential cold season CO_2 fluxes, we compare our constrained TVPRM member with CO_2 fluxes from previous studies (Sect. 3.3). Finally, we suggest and quantify sources of the missing CO_2 flux observed during the early cold season (defined here as September–December) and incorporate those fluxes into our net CO_2 budget (TVPRM Constrained + Additional Zero Curtain Emissions (ZC) and Inland Water Fluxes (IW)) (Sect. 3.4). This analysis provides a unique regional net CO_2 flux quantification for the North Slope that is verified using atmospheric observations and can also be explained from an ecological and physical perspective.

3. Results

3.1 Evaluation of unconstrained empirical net CO_2 flux model ensemble

3.1.1 Using aircraft-observed CO_2 enhancements

The observed ΔCO_2 during the ARM-ACME V (June–September 2015) and ABoVE Arctic-CAP (May–November 2017) airborne campaigns show a strong seasonal uptake pattern throughout the growing season (Figs. 2a–2b). The frequent flights during ARM-ACME V (multiple flights per week) observe the transition from early to peak growing season uptake (observed ΔCO_2 = –11 ppm) and on into cold season respiration, which results in net CO_2 source conditions in September (+5 ppm). While less frequent, the ABoVE Arctic-CAP flights begin at the end of the cold season, extend later into following cold season, and cover a larger area of the North Slope. Peak growing season uptake observed by the ABoVE Arctic-CAP flights (–14 ppm) is slightly stronger than for during ARM-ACME V, and by November, the ABoVE Arctic-CAP flights observe a strong CO_2 source throughout the North Slope (+10 ppm). The difference in observed ΔCO_2 during peak growing season uptake between 2015 and 2017 is likely similar to the uncertainty in the respective values and could be due to differences in areas of the North Slope sampled between years.

The magnitude and timing of the observed net CO_2 uptake throughout the growing season is generally well represented by the empirical net CO_2 flux model ensemble (TVPRM Unconstrained, Figs. 2a–2b, S6). The median coefficients of determination (R^2) and ordinary least squares slopes between the observed and simulated ΔCO_2 for this time are 0.54 and 0.41 for ARM-ACME V and 0.82 and 0.72 for ABoVE Arctic-CAP, respectively. Only for the July observations during the ABoVE Arctic-CAP campaign do many members of the CO_2 flux trend toward an underestimate of net CO_2 uptake, with all points showing a much larger range in simulated values compared to ARM-ACME V. The net CO_2 release tends to be overestimated by the TVPRM ensemble during the ABoVE Arctic-CAP seasonal transitions in May and September, but during November the observed R_{soil} ~~respiration~~ is consistently underestimated.

303

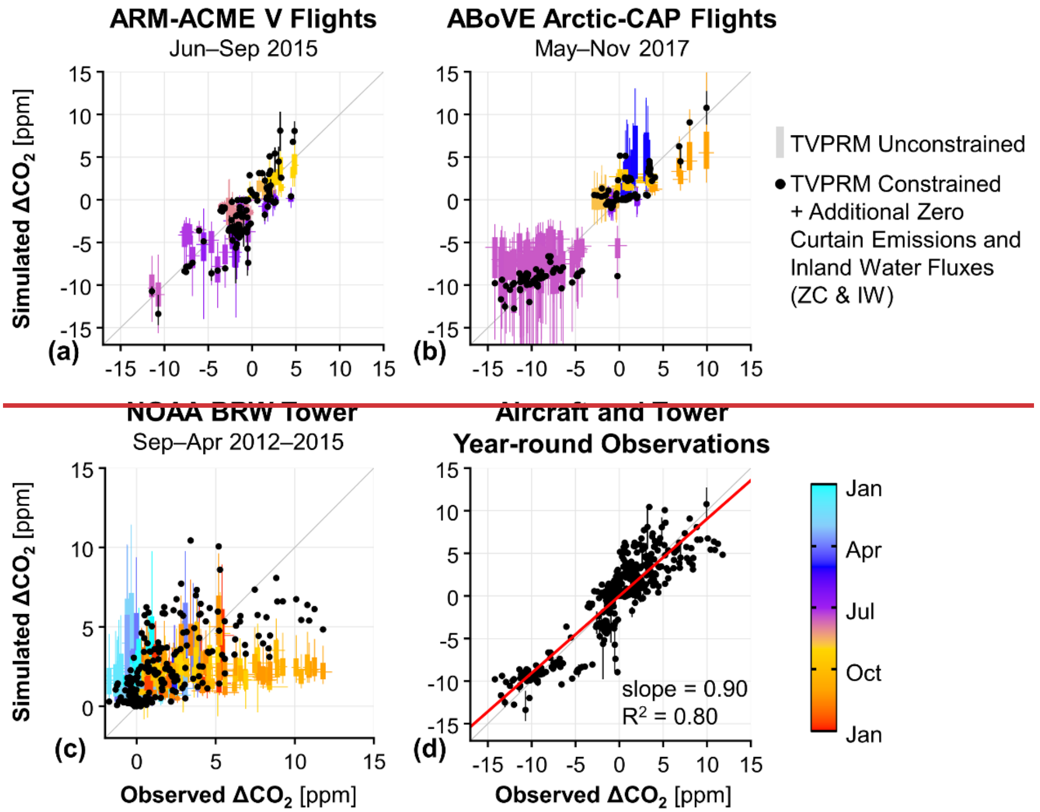

ARM-ACME V Flights
Jun–Sep 2015
ABoVE Arctic-CAP Flights
May–Nov 2017
TVPRM Unconstrained
TVPRM Constrained
+ Additional Zero
Curtain Emissions and
Inland Water Fluxes
(ZC & IW)
NOAA BRW Tower
Sep–Apr 2012–2015
Aircraft and Tower
Year-round Observations
Simulated ΔCO2 [ppm]
Observed ΔCO2 [ppm]
slope = 0.90
R2 = 0.80
Jan
Apr
Jul
Oct
Jan
(a)
(b)
(c)
(d)

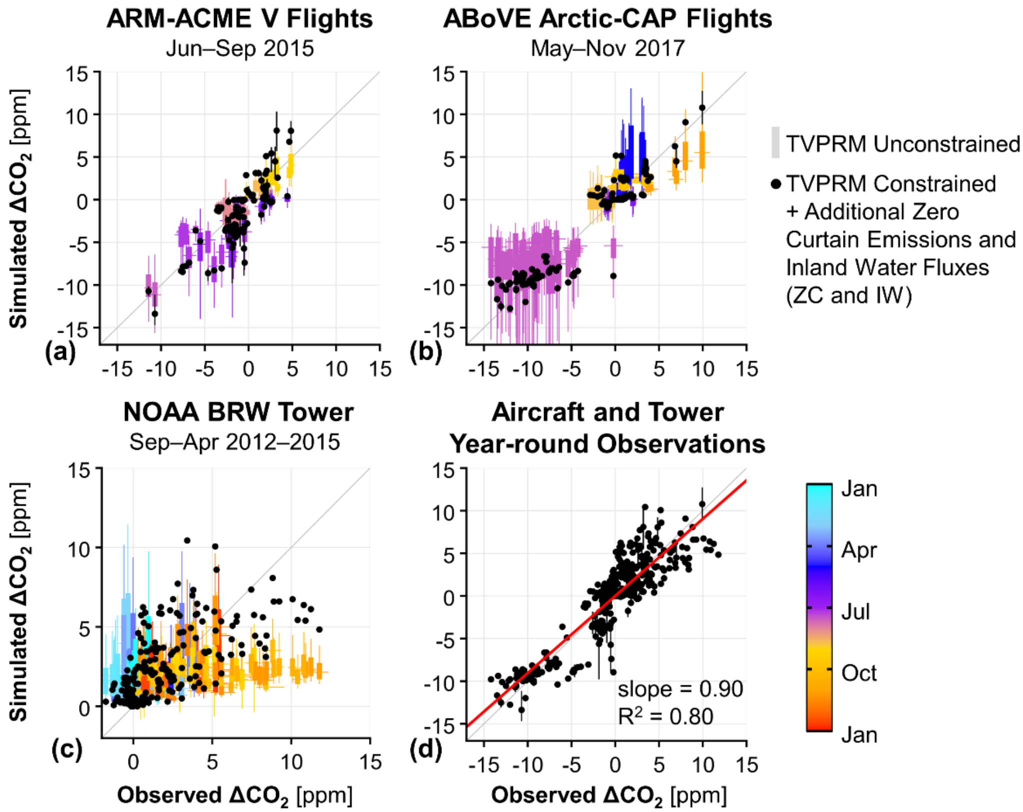

Figure 2. Aircraft and tower CO_2 concentration measurements constrain year-round simulated CO_2 fluxes on the Alaska North Slope. **(a)–(c)** Comparison of observed and simulated ΔCO_2 during the ARM-ACME V flight campaign **(a)**, during the ABoVE Arctic-CAP flight campaign **(b)**, and at the NOAA BRW tower **(c)** for air over the Alaska North Slope. Horizontal lines indicate range of uncertainty in the NOAA BRW tower ocean sector background calculation. Vertical boxes colored by month of the year represent 50% and whiskers represent 95% of ΔCO_2 values from all members of unconstrained TVPRM ensemble (see Sect. 2.4) from all binned points~~ and are colored by month of year~~. Black points show values from the constrained TVPRM member with additional zero-curtain emissions (ZC) and inland water fluxes (IW) (see Sect. 3.4). For **(a)**–**(b)**, observed values are vertically binned medians, and for constrained TVPRM member + ~~additional zero-curtain emissions (~~ZC~~)~~ and ~~inland water fluxes (~~IW~~)~~, vertical lines contain middle 95% of ΔCO_2 values from all binned points. **(d)** Combined comparison of observed and simulated ΔCO_2 for all aircraft and tower points using constrained TVPRM member + ZC and~~&~~ IW. Shown with linear best fit (red line), slope determined by ordinary least squares, and coefficient of determination (R^2) of all points (n = 455). 1:1 line shown in dark gray.

Given the large range of unconstrained representations of the regional CO_2 flux, the accuracy in simulating the aircraft observed ΔCO_2 varies between TVPRM ensemble members. For example, members using the RasterCAVM vegetation map, which places less coastal tundra area cover in the south (Fig. S5), produce a smaller mean July net CO_2 uptake flux (by ~1 μmol m^{-2} s^{-1}, Fig. S7a) throughout the southern North Slope than members using other vegetation maps (CAVM and ABoVE LC), and this placement consistently underestimates the net ΔCO_2 uptake during the growing season compared to the aircraft observations by 5–10 ppm (Fig. S8). Also, members driven by SIF products that integrate additional remote sensing and/or meteorological data (GOSIF and CSIF) better reflect the timing and magnitude of the peak season carbon uptake in tundra ecosystems than members produced by interpolated SIF retrievals (GOME-2 SIF product), which underestimate the observed CO_2 uptake during July (Fig. S8).

Using these comparisons, we identify less-representative ensemble members that generally underestimate the observed ΔCO_2 uptake during the growing season (RasterCAVM vegetation map and GOME-2 SIF product members). Removing these members from the TVPRM ensemble improves the collective performance of the remaining members during the growing season (Fig. S6), brings the median slope of agreement closer to 1 for both campaigns (improves from 0.53 to 0.64 and from 0.71 to 0.94 for ARM-ACME V and ABoVE Arctic-CAP, respectively), and reduces median NMB (–0.34 to –0.03) and median RMSE (3.12 to 2.73) for ABoVE Arctic-CAP.

3.1.2 Using tower-observed CO_2 enhancements

As seen with the September–November aircraft data, the observed ΔCO_2 at the NOAA BRW tower (Fig. 2c) indicate that the CO_2 source to the atmosphere increases substantially from September to peak in October and November (+12 ppm) before decreasing to near zero throughout the late cold season (January–April).

Most of the TVPRM ensemble members substantially underestimate the observed ΔCO_2 in the early cold season (September–December) as the soils freeze, and some simulations produce too much CO_2 in the late cold season when the soils are frozen (Fig. 2c). The cold season CO_2 flux differs greatest in magnitude and spatial extent between the ensemble members parameterized for the ICS and ICT inland tundra sites (Figs. 3a, S9–S10), with a net CO_2 flux difference of ~0.2 μmol m^{-2} s^{-1} throughout the region (Fig. S7b).

While the magnitude of CO_2 flux from ICS members better matches the observed ΔCO_2 in the early cold season than from other sites (Figs. 3b–3c, S11), the response to T_S ~~soil temperature~~ at ICS shows only a modest decrease in CO_2 flux between the early and late cold season (Fig. 3a, 32% decrease between October and March), resulting in an overestimate of the regional ΔCO_2 in the late cold season. The CO_2 flux response to T_S ~~soil temperature~~ for ICT members is similar to that for ICS but lower in magnitude, and the simulated ΔCO_2 from members of neither site performs well against the observations in both the early and late cold season. Therefore, ICS and ICT inland tundra responses to T_S ~~soil temperature~~ are not representative of the regional ΔCO_2 observed at the NOAA BRW tower throughout the entire cold season, and we remove those members from our TPVRM ensemble.

The observed net CO_2 fluxes at the IVO inland tundra and CMDL coastal tundra sites both show prolonged zero-curtain emissions (Fig. S1) and respond strongly to T_S ~~soil temperature~~ in the early cold season (Fig. S9). The stronger response of CO_2 fluxes to T_S ~~soil temperature~~ from the early to late cold season at IVO (Fig. 3a, 70% decrease by January) compared to at the Imnavait Creek sites produces TVPRM members that better represents the large regional decrease in ΔCO_2 observed on the North Slope (Fig. 3c). While all coastal tundra sites respond similarly to T_S ~~soil temperature~~ during the cold season, we determine that the CO_2 flux magnitude at CMDL is most consistent with the regional observations (Fig. S11). T_S~~Soil temperatures~~ from ERA5 remain warmer throughout the late cold season compared to those from NARR, which causes simulations using ERA5 T_s ~~soil temperatures~~ to overestimate CO_2 release during that time (Fig. S11). Unlike during the growing season, cold season CO_2 fluxes are not sensitive to the vegetation distribution and SIF products.

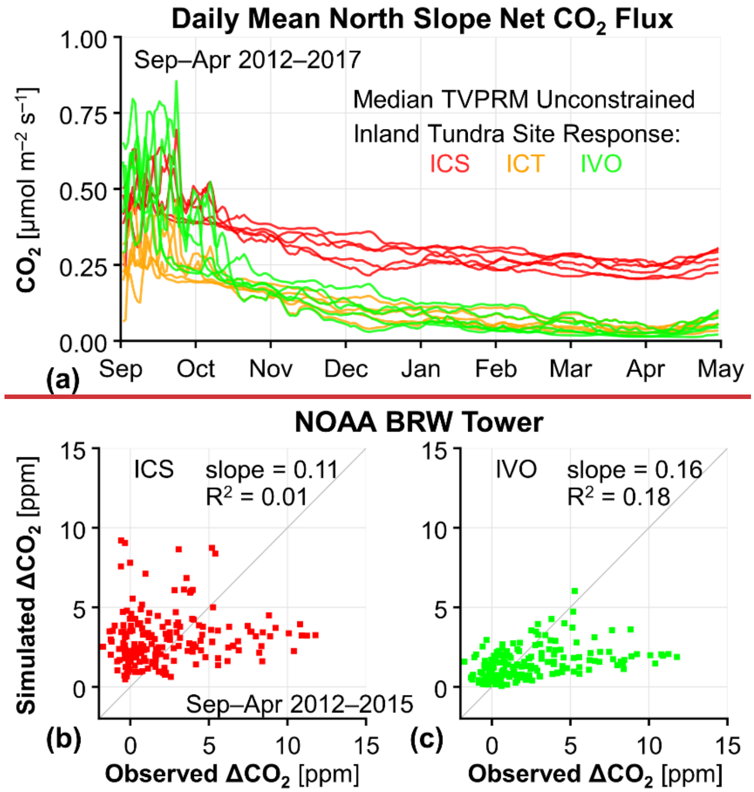
Daily Mean North Slope Net CO_2 Flux
Sep–Apr 2012–2017
Median TVPRM Unconstrained
Inland Tundra Site Response:
ICS ICT IVO
CO_2 [μmol m^{-2} s^{-1}]
1.00
0.75
0.50
0.25
0.00
Sep Oct Nov Dec Jan Feb Mar Apr May
(a)
NOAA BRW Tower
ICS slope = 0.11
R^2 = 0.01
IVO slope = 0.16
R^2 = 0.18
Simulated ΔCO_2 [ppm]
Sep–Apr 2012–2015
(b)
(c)
Observed ΔCO_2 [ppm]
Observed ΔCO_2 [ppm]
0 5 10 15

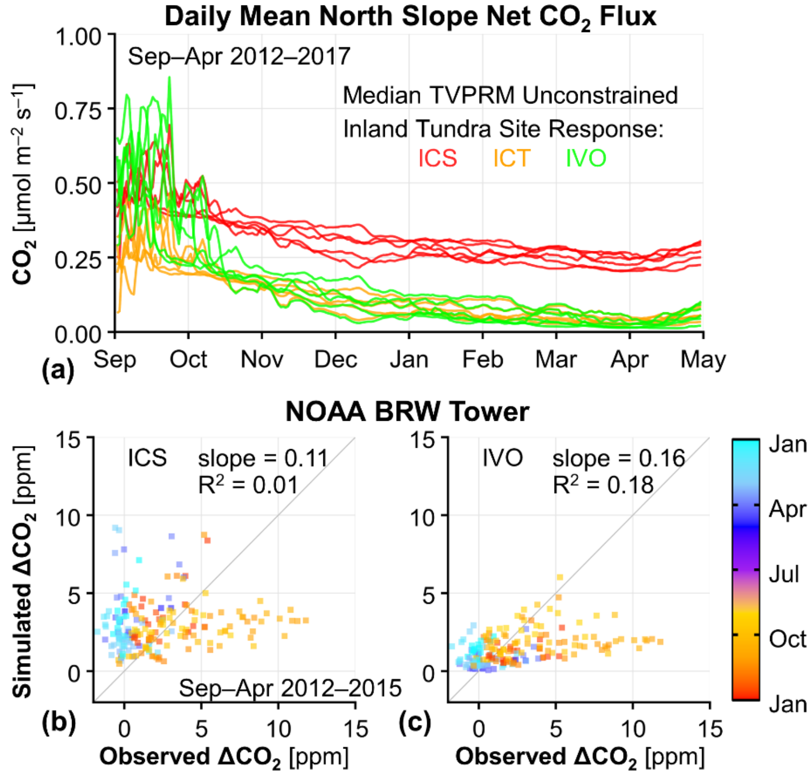

Figure 3. Cold season CO_2 emissions for inland tundra site parameterizations and comparison to tower observations. **(a)** Timeseries of simulated daily mean Alaska North Slope net CO_2 flux for the median of all unconstrained TVPRM ensemble members using each of three inland tundra site parameterizations: ICS (red), ICT (orange), and IVO (green). Yearly colored lines shown for Sep–Apr beginning in Sep 2012 and ending in Apr 2017. Same for all eight eddy flux sites shown in Fig. S9. **(b)**–**(c)** Comparison of observed and simulated ΔCO_2 at the NOAA BRW tower for air over the North Slope using the median of all unconstrained TVPRM ensemble members for the inland tundra site parameterizations at ICS (b~~, red~~) and IVO (c~~, green~~). All points colored by day of year. Shown with slope determined by ordinary least squares and coefficient of determination (R^2) of all points (n = 191). 1:1 line shown in dark gray.

Finally, we identify the TVPRM member that best matches the observed ΔCO_2: parameterized by IVO inland tundra and CMDL coastal tundra site responses, distributed by the ABoVE LC vegetation map, and driven by NARR reanalysis and the CSIF SIF product (referred to here as TVPRM Constrained, Figs. S6, S12). This constrained simulation estimates a mean regional CO_2 flux of 0.05 μmol m^{-2} s^{-1} for the late cold season in 2012–2015 and reproduces well the observed ΔCO_2 during this time (Fig. 4a). The late cold season NMB and RMSE against the observations at the NOAA BRW tower are reduced from 4.91 to 2.04 and from 1.94 to 1.30, respectively, for the constrained simulation compared to the median of the entire TVPRM ensemble (Fig. S12). However, the early cold season CO_2 emissions, with a mean regional CO_2 flux of 0.25 μmol m^{-2} s^{-1} for September–December (Fig. S13a), are still underestimated, with the simulated ΔCO_2 lower than the observed ΔCO_2 by ~5 ppm (Fig. 4a).

375

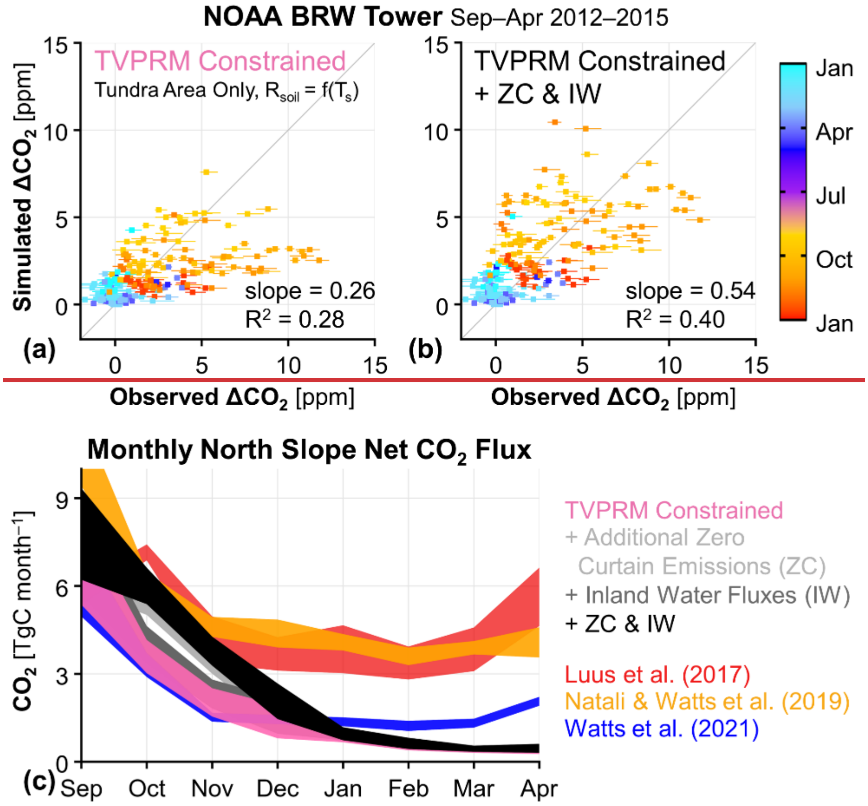

NOAA BRW Tower Sep–Apr 2012–2015
TVPRM Constrained
Tundra Area Only, $R_{soil} = f(T_s)$
slope = 0.26
R^2 = 0.28
(a)
TVPRM Constrained
+ ZC & IW
slope = 0.54
R^2 = 0.40
(b)
Simulated ΔCO_2 [ppm]
Observed ΔCO_2 [ppm]
Jan
Apr
Jul
Oct
Jan
Monthly North Slope Net CO_2 Flux
CO_2 [TgC month^{-1}]
TVPRM Constrained
+ Additional Zero Curtain Emissions (ZC)
+ Inland Water Fluxes (IW)
+ ZC & IW
Luus et al. (2017)
Natali & Watts et al. (2019)
Watts et al. (2021)
(c)
Sep Oct Nov Dec Jan Feb Mar Apr

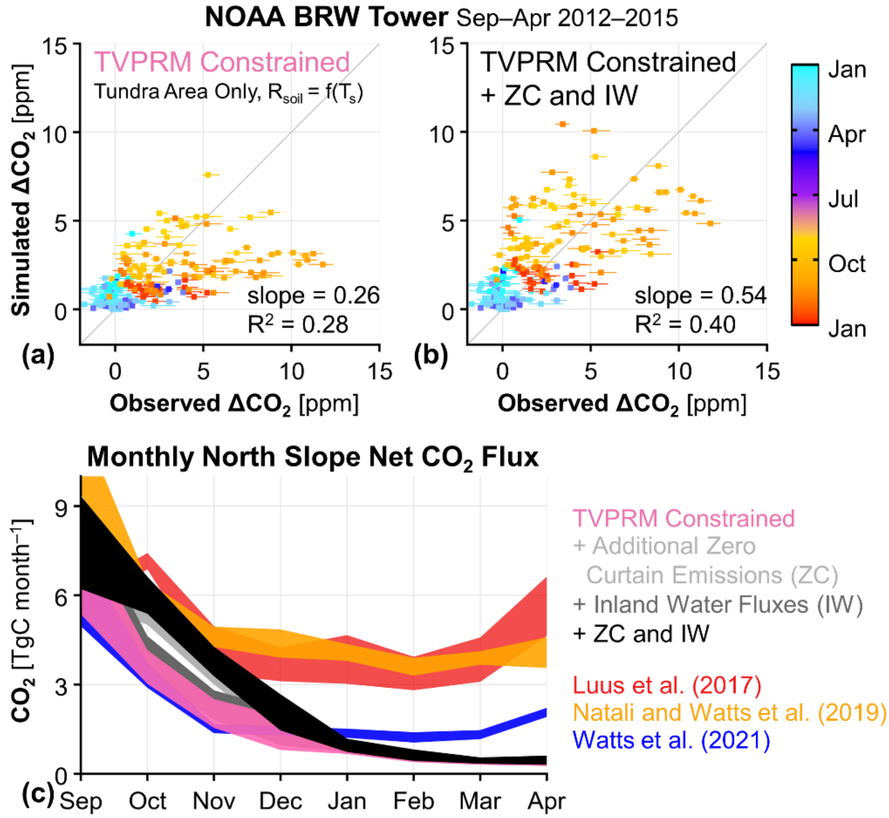

Figure 4. Tall tower atmospheric observations of the Alaska North Slope support early cold season emissions not driven by soil temperature (T_s) and present no evidence for elevated late cold season emissions. **(a)**–**(b)** Comparison of hourly cold season (Sep–Apr) observed and simulated ΔCO_2 at the NOAA BRW tower for the constrained TPVRM member, where soil respiration (R_{soil}) is determined only by ~~soil temperature (~~T_s~~)~~ **(a)** and for the constrained TVPRM member + additional zero-curtain emissions (ZC) and inland water fluxes (IW) **(b)**. Horizontal segments indicate range of uncertainty in the NOAA BRW tower ocean sector background calculation. Shown with slope determined by ordinary least squares and coefficient of determination (R^2) of all points (n = 191). 1:1 line shown in dark gray. **(c)** Monthly cold season total Alaska North Slope net CO_2 fluxes for various CO_2 flux models. TVPRM-based simulations and Natali and~~&~~ Watts et al. (2019) show values for 2012–2017, Luus et al. (2017) show 2012–2014, and Watts et al. (2021) show Sep 2016–Apr 2017. Ribbons represent range of all years, where applicable. Area of the North Slope domain used to calculate regional totals is 3.537×10^5 km^2.

3.2 Alternative T_s~~soil temperature~~ products and R_{soil} ~~respiration~~ parameterizations

To test the impact of reanalysis T_s~~soil temperature~~ on the early cold season CO_2 fluxes, we implement T_s~~soil temperatures~~ that ~~better account for the controls of more complex~~are more specifically developed to represent Alaska tundra permafrost soils during freeze-thaw processes ~~like soil moisture and snow cover~~ than the reanalysis products driving our constrained TPVRM member. A single layer of T_s~~soil temperature~~ at 8 cm depth from RS-PM (Fig. S14a) captures the magnitude and temporal behavior of the observed early cold season CO_2 fluxes slightly better than the constrained member (Figs. 4a, S12), which uses NARR reanalysis T_s~~soil temperature~~ and does not incorporate permafrost-model derived T_s~~soil temperature (Fig. S14a)~~. The RS-PM T_s~~soil temperature~~ extends CO_2 emission fluxes further into the cold season by up to a month, which is consistent with a better representation of the zero-curtain period, however, emissions remain higher throughout the late cold season than our atmospheric observation-constrained CO_2 fluxes (Fig. S15). We also test the implementation of a multi-layer fit driven by soil column temperature from RS-PM, but neither of these instances of remote sensing informed T_s~~soil temperatures~~ substantially improve the agreement of the ΔCO_2 at the NOAA BRW tower during the early cold season. Attempts to use alternative R_{soil}~~respiration~~ formulations based on T_s~~soil temperature~~, including Q_{10} relationships, also fail to reproduce the observed elevated CO_2 fluxes during the cold season.

3.3 Evaluation of other CO_2 flux models during the cold season

More early cold season (September–December) CO_2 flux into the atmosphere is observed at the NOAA BRW tower than is emitted by our constrained empirical simulation member, and these observations also indicate low late cold season (January–April) CO_2 emissions. We compare our constrained CO_2 fluxes to several other representations of gridded CO_2 flux on the North Slope (Table S3~~2~~) and find that difficulty in simulating the magnitude and timing of the observed ΔCO_2 throughout the cold season is not unique to the constrained fluxes from our study.

The net CO_2 fluxes from Luus et al. (2017) are similar to the constrained TVPRM member during the growing season (Fig. S16), but release more than three times as much CO_2 into the atmosphere throughout the late cold season (Fig. 4c). This large late cold season CO_2 flux leads to a large overestimate compared to the observed ΔCO_2 (Fig. S14b). The optimization employed by Commane et al. (2017) increases the September–October CO_2 flux to a range that matches our observations at the NOAA BRW tower. However, Commane et al. (2017) did not optimize the cold season fluxes from November to March, but reverted to Luus et al. (2017) fluxes during this time, thus producing late cold season fluxes that are too large. Overall, Commane et al. (2017) projected a regional total cold season CO_2 source of 37–40 TgC for 2012–2014, which is more than twice as high as our constrained TVPRM member CO_2 flux (15–18 TgC) for those years.

Carbon dioxide fluxes from work by Natali and~~&~~ Watts et al. (2019), a cold season model developed for the global high latitude permafrost region, are similar to our constrained TVPRM member in September, but the fluxes remain high throughout the cold season (Fig. 4c) similarly to Luus et al. (2017), for a range of total cold season CO_2 flux of 40–43 TgC for 2012–2017. This sustained CO_2 release also leads to an overestimation in the ΔCO_2 in the late cold season for this region (Fig. S14c). Tao et al. (2021) also show that the cold season CO_2 fluxes of Natali and~~&~~ Watts et al. (2019) are high compared to their model. More recent work by Watts et al. (2021), using observations from new Soil Respiration Station monitoring sites in Alaska, produces cold season CO_2 fluxes more similar to our constrained CO_2 fluxes, with an underestimate in the simulated ΔCO_2 during the early cold season (Fig. S14d), for a total cold season CO_2 flux of 18 TgC for September 2016 to April 2017.

3.4 Sources of missing CO_2 fluxes

None of the flux products discussed above, including our TVPRM ensemble, account for any potential CO_2 fluxes during the zero-curtain period that are not driven by T_s~~soil temperature~~ or are from areas on the terrestrial-aquatic interface. To account for these processes, we first add an additional CO_2 flux with zero-curtain timing to our constrained CO_2 flux (TVPRM) member from both inland and coastal tundra areas that consists of 0.25 μmol m^{-2} s^{-1} for October with a reduction to zero by the end of

December. This peak additional CO_2 flux is within the daily variability of the observed CO_2 flux at the IVO and CMDL eddy flux sites during the zero-curtain period (Fig. S9) and the reduction into December is consistent with these observations. ~~and~~ The additional zero-curtain flux improves the ability of the model to reproduce the observed ΔCO_2 at the NOAA BRW tower (slope = 0.46, R^2 = 0.41). We also apply the coastal tundra site ecosystem parameterization used in our constrained TVPRM member to all areas of inland water on the North Slope, which account for 4% of the domain according to the ABoVE LC map (Fig. S5) and were previously set to zero CO_2 flux ~~(Fig. S5)~~. Representing these aquatic areas with biogenic CO_2 fluxes consistent with coastal tundra ecosystems is one simple way to bridge the terrestrial-aquatic gap in tundra ecosystem models, where portions of aquatic systems on the land-water gradient (i.e., the edges) may be more likely to respond to the environment as coastal tundra than with the zero-flux assumed by water area. The ice phenology for areas of inland water producing CO_2 flux is then considered to be similar to that of the freeze-thaw timing in coastal tundra soils. ~~and~~Adding these coastal tundra fluxes to inland water areas also improves the performance of our model (slope = 0.32, R^2 = 0.30 against NOAA BRW tower observations). The magnitude of additional zero-curtain flux suggested here and the portion of inland water represented with coastal tundra site parameterizations produce the best statistical comparison for a range of choices tested (Fig. S17).

Together, adding these zero-curtain (ZC) and inland water (IW) CO_2 fluxes to our constrained simulation (referred to as TVPRM Constrained + ZC and~~&~~ IW) increases the mean regional CO_2 flux in early cold season by 70% (0.18 µmol m^{-2} s^{-1}, Fig. S13b) and results in a large improvement to our comparison of ΔCO_2 at the NOAA BRW tower (slope = 0.54, R^2 = 0.40, Figs. 4b, S12) and across the region using airborne data, especially during the November ABoVE Arctic-CAP flights (Figs. 2, S6). The year-round comparison using all available aircraft and tower observations shows these net CO_2 fluxes are now representative of the region (slope = 0.90, R^2 = 0.80, Fig. 2d). As a result, the North Slope regional total cold season CO_2 flux increases by 6 TgC (~38%) to 20–24 TgC for 2012–2017 compared to the constrained empirical CO_2 flux model member.

3.5 Alaska North Slope annual net CO_2 flux

The median Alaska North Slope annual net CO_2 flux from the TVPRM ensemble (–5 TgC yr^{-1}) for 2012–2017 is consistent with the previous multi-model comparison (Fisher et al., 2014), but we find a much smaller range in regional CO_2 flux values (26 TgC yr^{-1} to –29 TgC yr^{-1} for 95% of TVPRM members) (Fig. S18). The largest contribution to this ensemble range comes from the difference in parameterizations determined for the ICS and ICT inland tundra sites, with TVPRM members using ICS trending toward a net CO_2 source, while ICT trends toward net CO_2 uptake. The distribution of inland and coastal tundra throughout the region represented by the vegetation maps also has a noticeable impact on the sign of the net CO_2 flux, with members using the RasterCAVM more likely to release net CO_2 into the atmosphere than members using the other maps. There is also little interannual variability in the unconstrained TVPRM ensemble, with only 2014 moving toward a net CO_2 source, consistent with Tao et al. (2021) for these years.

Our best quantification of the annual net CO_2 flux for the North Slope informed by atmospheric observations, TVPRM Constrained + ZC and~~&~~ IW, indicates that the region is a small net sink for 2013 (–5 TgC yr^{-1}) and 2015 (–6 TgC yr^{-1}) and a small net source for 2012 (+6 TgC yr^{-1}), 2014 (+6 TgC yr^{-1}), 2016 (+2 TgC yr^{-1}), and 2017 (+2 TgC yr^{-1}) (Fig. 5a). We estimate a 10% uncertainty in the net annual CO_2 flux based on the slope from our final comparison with the year-round observations (Fig. 2d). The year-round net CO_2 fluxes from Luus et al. (2017) (driven with NARR meteorology, monthly GOME-2 SIF, and CAVM vegetation map) indicate the North Slope to be a strong annual net CO_2 source for 2012–2014 (+9 TgC yr^{-1} to +15 TgC yr^{-1}, Fig. S18) and are inconsistent with our results. Our results are more consistent with Tao et al. (2021), but we find a smaller range in the magnitude of net CO_2 flux over the same years and more years trending toward a net CO_2 source.

467

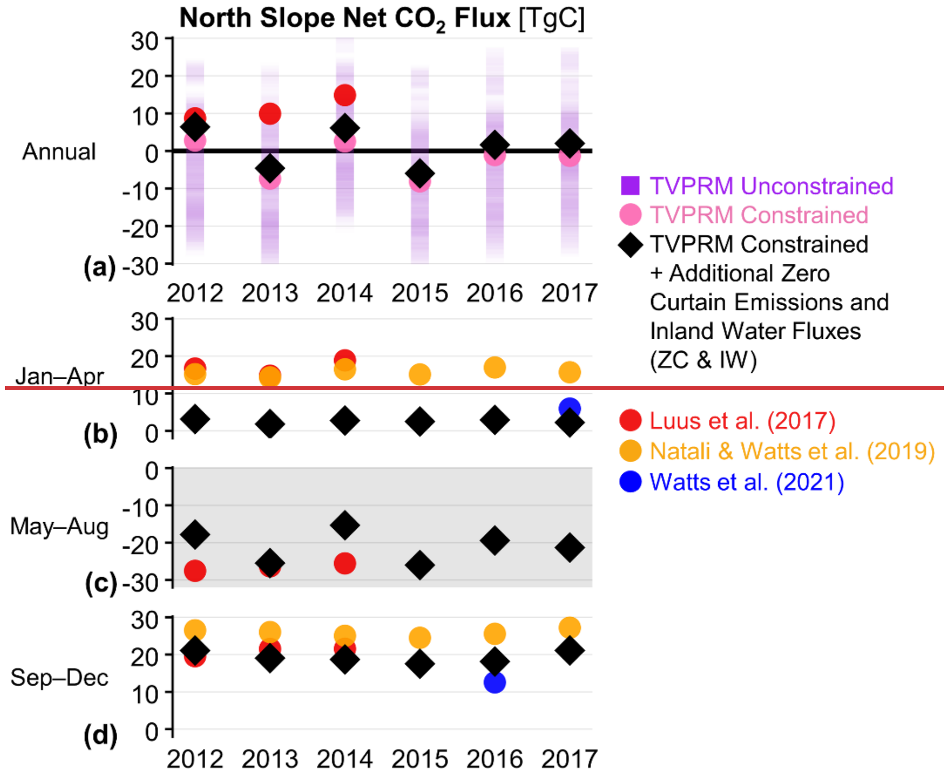

North Slope Net CO_2 Flux [TgC]
Annual
Jan–Apr
May–Aug
Sep–Dec
(a)
(b)
(c)
(d)
30
20
10
0
-10
-20
-30
2012 2013 2014 2015 2016 2017
TVPRM Unconstrained
TVPRM Constrained
TVPRM Constrained + Additional Zero Curtain Emissions and Inland Water Fluxes (ZC & IW)
Luus et al. (2017)
Natali & Watts et al. (2019)
Watts et al. (2021)

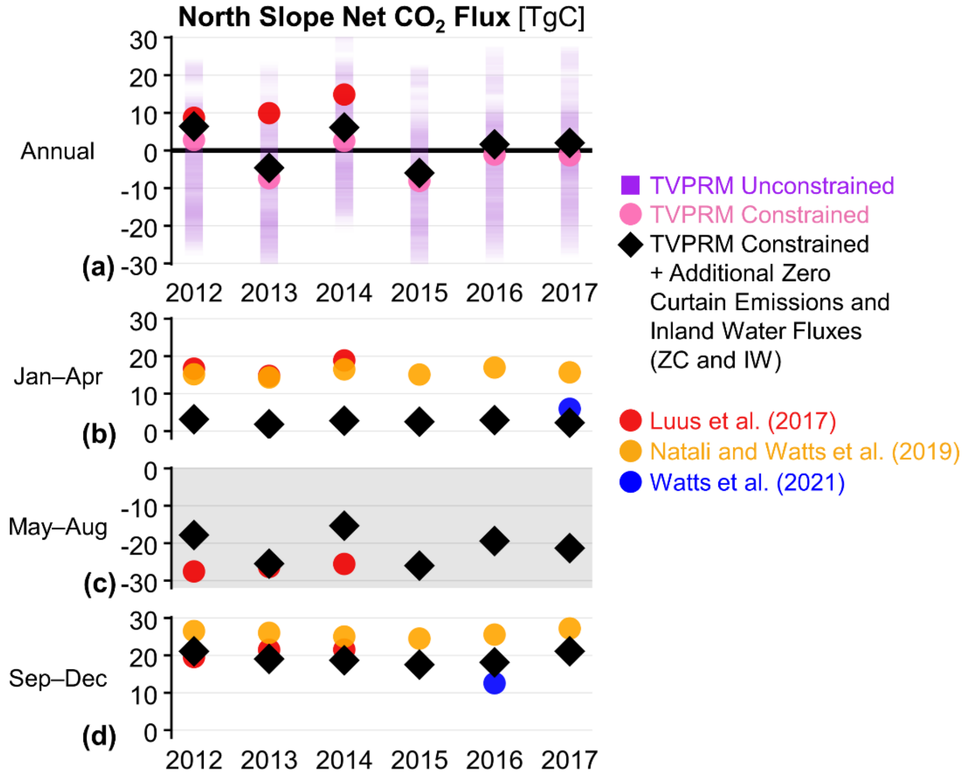

Figure 5. Annual and seasonal Alaska North Slope net CO_2 flux constrained by aircraft and tower observations. **(a)** Annual, **(b)** late cold season (Jan–Apr), **(c)** growing season (May–Aug), and **(d)** early cold season (Sep–Dec) total Alaska North Slope net CO_2 fluxes for various CO_2 flux models for 2012–2017 as in Fig. 4. Purple squares indicate middle 95% of all TVPRM ensemble members.

We find that the regional net growing season CO_2 uptake and the cold season emissions on the North Slope are comparable in magnitude, so the net balance could depend on small perturbations in either flux. However, the regional cold season CO_2 emissions for these years were relatively similar from year to year: 18–21 TgC for the early cold season (Fig. 5d), diminishing to only 2–3 TgC for the late cold season (Fig. 5b). Therefore, the interannual variability of the regional carbon balance is largely driven by fluctuating net growing season CO_2 fluxes during these years: greater net growing season uptake in 2013 and 2015 than in 2012, 2014, 2016, and 2017 (Fig. 5c).

4. Discussion

4.1 Tundra ecosystem growing season net CO_2 fluxes

The good performance of the TVPRM ensemble against the atmospheric observations during the growing season indicates that the tundra ecosystems of the Alaska North Slope respond to light and heat as quantified by PAR, T_s, and T_a ~~expected given previous knowledge~~, and that the net CO_2 flux is largely controlled by the simple R_{soil}, R_{plant}, and GPP relationships in the empirical model over this time.

The growing season of each year determines the sign of the regional annual net CO_2 flux during our study period, with 2013 and 2015 being strong net sinks and 2014 being the strongest net source. The relative magnitude of each component of the net CO_2 flux during the growing season (i.e., R_{soil}, R_{plant}, GPP) varies from year-to-year (Table S7) and helps explain the interannual variability in the net source or sink status of the North Slope. Growing season 2015 was very warm, dry, and sunny in Alaska and resulted in extreme biomass burning activity outside of the North Slope (Table S1). High regional mean T_a and PAR (Table S8) and low accumulated precipitation (Table S9) in NARR confirm this was the case for North Slope as well, with high T_a and PAR contributing to a very high GPP. The growing season SIF signal from the CSIF product, which determines the seasonal cycle and relative magnitude of photosynthetic activity, is also large in 2015 (Table S8), further enhancing GPP. This year and others with a larger GPP component of NEE correspond to growing seasons with stronger SIF signals, which is an indicator of increased productivity and consistent with previous studies (e.g., Magney et al., 2019; Sun et al., 2017). While fairly high T_a and T_s in 2015 also result in high R_{soil} and R_{plant}, respectively, this elevated respiration is not enough to offset the very high GPP and results in a large net CO_2 sink. In contrast, the summer of 2014 was cool, wet, and cloudy, and the North Slope experienced very low T_a, PAR, and SIF signal, producing very low GPP. Lower-than-normal T_a also results in very low R_{plant}, but as with 2015, this is not enough to offset the extremely low uptake resulting in a large net CO_2 source for 2014. In 2013, the other growing season with a strong net CO_2 sink, moderately high GPP combines with moderately low R_{plant} and very low R_{soil}. Extremely low T_s causes this very low R_{soil}, which, relative to moderate T_a and PAR, is likely a result of above-average lingering snowpack into May (Table S9). This lingering snowpack is perhaps surprising given that the mean snowpack for the proceeding cold season was not particularly deep. The important impact that snow cover and the timing of snowmelt has on T_s and carbon response in tundra ecosystems has been recently emphasized (e.g., Kim et al., 2021), and is supported by our work, which shows that the prevalence of snow in the spring may determine the sign of the regional net CO_2 for an entire year.

The regional net CO_2 flux is highly sensitive, however, to the distribution of tundra vegetation types (upland v. coastal) throughout the North Slope during the growing season. ~~Since c~~Coastal tundra takes up more CO_2 for a given unit PAR compared to inland tundra, based on the relationships between observed site-level net CO_2 flux and PAR in this study (TVPRM parameters, Fig. S1), which could be evidence for an adaptation to lower light levels. This difference is consistent with ~~(~~Luus et al.~~,~~ (2017), who calculated greater uptake at "wetland" sites like Atqasuk and Barrow than at "graminoid tundra" sites like Ivotuk and Imnavait when all driver inputs are constant~~,~~ and with ~~(~~Mbufong et al.~~,~~ (2014), who also found that peak growing season net uptake for constant light is greater at Barrow than at Ivotuk. The stronger CO_2 uptake response of coastal tundra to light is important to consider due to the fact that the vegetation distributions assessed here with more coastal tundra to the south (CAVM (Walker et al., 2005), ABoVE LC (Wang et al., 2020)) better agree with the atmospheric observations. When considering the ability of coastal tundra to take up CO_2 when moved toward the south, ~~(~~Patankar et al.~~,~~ (2013) saw that tundra plants exposed to additional intense light did not respond with additional uptake. ~~suggests~~ Therefore, while the ecosystem response of the southern North Slope is more consistent with coastal ecosystems, it seems possible that these areas are misclassified in either our simplified two-tundra type scheme or in the vegetation maps themselves. The~~is~~ ~~result~~ large variability in net CO_2 flux calculated by using the different maps~~also~~ supports the importance of accurate ecosystem type locations in upscaling eddy flux measurements and highlights the need for improved vegetation mapping and classification schemes in the Arctic ecology research community.

~~The seasonal cycle of photosynthetic activity, represented in the TVPRM ensemble by SIF, also strongly impacts the growing season regional net CO_2 flux. Our study years with greater net CO_2 uptake correspond to growing seasons with stronger SIF signals, which is related to increased productivity, and consistent with previous studies (e.g., Magney et al., 2019; Sun et al., 2017). (Kim et al., 2021)Although there is not a consistent correlation with increases in T_a air temperature and PAR during these years, the larger uptake may be due to a combination of these and/or other drivers not accounted for explicitly in our empirical simulation that are represented by SIF.~~

4.2 Regional-scale cold season CO_2 emissions

Observations across scales, at the in-situ eddy flux towers, the NOAA BRW tower, and from aircraft, consistently show signs of large early cold season CO_2 emissions from ecosystems on the Alaska North Slope. However, there is no evidence of widespread elevated emissions in this region during the late cold season, contrary to other studies (Commane et al., 2017; Natali and~~&~~ Watts et al., 2019). The TVPRM ensemble parameterizations using terrestrial eddy flux sites and the fluxes from other terrestrial CO_2 models cannot reproduce both the observed magnitude and across-season timing of these cold season CO_2 emissions.

The largest differences in the net CO_2 flux between TVPRM ensemble members result from the contrasting site conditions driving the ICS and ICT R_{soil} ~~respiration~~ parameterizations during the cold season. When taken separately by cold season segment, ICS members perform quite well against observations at the NOAA BRW tower for early cold season and ICT members perform well for the late cold season. The contrasting performance between site parameterizations is due to the topographic and hydrologic conditions, which are quite heterogeneous over a short distance and influence the plant communities and carbon storage, at each site. The ecosystems sampled by the ICS tower are seasonally inundated and retain a deep layer of organic soil that can be respired in greater amounts longer into the early cold season, while the well-drained hillslope at ICT does not allow for accumulation of organic matter in the same way (Euskirchen et al., 2017; Larson et al., 2021). While varying topography and soil inundation throughout the North Slope means that each of these site relationships is likely to be representative of many other locations in the region with similar conditions, ~~T~~the early-to-late cold season reduction in CO_2 fluxes at these sites is not consistent with the observed regional atmospheric trend, however, and we remove the members parameterized by them from the ensemble. ~~While i~~Individual eddy flux site parameterizations may reproduce regional CO_2 fluxes for a given season, but it is important to consider their response to drivers across multiple seasons when scaling from the site-level to regional domains.

The observed cold season CO_2 flux pattern on the North Slope may be unique to tundra ecosystems of this region. For example, the CO_2 fluxes from Natali and~~&~~ Watts et al. (2019) and Watts et al. (2021) both incorporate measurements from the North Slope. However, Natali and~~&~~ Watts et al. (2019) used boosted regression trees trained on belowground respiration measurements from across the pan-Arctic tundra and boreal zones, which may not be representative for our study region. The fluxes from Watts et al. (2021) are based on respiration measurements from throughout only Alaska and northwest Canada and conform better to local conditions. The evaluation of these CO_2 fluxes against atmospheric CO_2 measurements also produces results that are more consistent with our TVPRM ensemble determined by North Slope eddy flux tower measurements.

We find that the atmospheric observations are best matched by biogenic CO_2 fluxes that include an additional CO_2 source from tundra ecosystems during the zero-curtain period that are independent from T_s~~soil temperature~~ variability and year-round net CO_2 fluxes from areas of inland water. The additional zero-curtain flux represents large-scale emission events not directly timed ~~related~~ to microbial activity and root respiration controlled by T_s~~soil temperature~~, but could be related to the delayed physical release of previously produced CO_2 from soil through the snowpack as the soil layers remain unfrozen (Bowling and Massman, 2011). The Alaska North Slope also has many water bodies distributed throughout the coastal tundra region, and the extent to which carbon cycles between small, shallow ponds and their surrounding terrestrial components is unclear (Magnússon et al., 2020). The biogenic CO_2 fluxes in these areas are likely driven by ecosystem-scale CO_2 fluxes from both coastal tundra and small ponds (Holgerson and Raymond, 2016; Tan et al., 2017) and their impact on the regional net CO_2 flux, via both emissions and uptake, may be significant (Elder et al., 2018; Beckebanze et al., 2022). Only by adding fluxes that match observed zero-curtain CO_2 emission pulses and by approximating net CO_2 fluxes in aquatic areas can we reproduce the observed ΔCO_2 magnitude in both early and late cold season. The resulting seasonal change between the early and late cold season is consistent with the extended duration of the observed regional-scale zero curtain. The simplistic approximations suggested here are not inconsistent with the existing uncertainties in tundra CO_2 flux modeling and demonstrate the importance of considering these additional CO_2 fluxes and their mechanisms for future study.

4.3 Future state of net CO_2 flux on the Alaska North Slope

As the Arctic warms rapidly, the competition between the growing and cold season Arctic CO_2 fluxes will determine the net biogenic CO_2 flux into the atmosphere. Warming T_a~~air temperature~~ warms soils, thaws permafrost, increases active layer thickness and has extended the duration of the zero curtain from weeks to over 100 days (Romanovsky and Osterkamp, 2000; Schuur et al., 2015; Zona et al., 2016), all of which increase cold season CO_2 emissions. The warming may also increase net growing season uptake, but the severe light limitation at high northern latitudes limits the extent of the growing season, especially on the North Slope (Zhang et al., 2020). The future of CO_2 fluxes from inland waters and wetlands in the Arctic is uncertain, but some studies suggest CO_2 emissions from lakes may increase (Bayer et al., 2019). The culmination of these effects will likely push the North Slope into a consistent net source in the future. However, observations at the NOAA BRW tower during our study period do not show elevated late cold season CO_2 emissions, so the North Slope was not a consistent net source through 2017. Accordingly, care must be taken to accurately represent CO_2 fluxes from Arctic ecosystems during both the early and late cold season when calculating the annual net CO_2 budget. TVPRM could be used with projections of meteorology and SIF to calculate the future net CO_2 balance for this region, but we caution against overuse of the model using current parameters, as the flux-driver relationships in the rapidly warming Arctic ecosystems are changing so quickly that we would not assume accuracy into the future. While we can constrain the annual net CO_2 budget with existing data, the Arctic is rapidly changing and needs constant monitoring. The~~se~~ following recommendations would provide more detailed spatial and seasonal constraints and up-to-date information on the processes driving CO_2 fluxes across the region.

4.3.1 Future observation efforts

Our results motivate~~motive~~ the need for a more extensive network of CO_2 eddy flux towers operating year-round, alongside sensors for soil moisture and T_s~~soil temperature~~ profiles throughout the active layer to better understand the mechanisms driving year-round and especially early cold season CO_2 fluxes. Noting that automated or semi-automated monitoring systems for aquatic environments currently do not exist for the North Slope or other high latitude regions, this sensor network should be distributed throughout poorly sampled ecosystem types, particularly along wetness gradients that span mixed terrestrial-aquatic environments. The results in this study also support the need for additional continuous CO_2 concentration measurements at tall towers across the North Slope (including away from the coast) to increase coverage of observed ΔCO_2 during all seasons and to better constrain the regional background. Airborne measurements of both CO_2 concentrations and CO_2 fluxes remain valuable to sample areas less accessible via ground-based measurements, but a large-scale flight campaign in the region has not occurred since 2017. Any additional flights should be targeted as early before, and as late after, the growing season as possible. Satellites that rely on reflected sunlight to detect CO_2 have increasingly been used to constrain CO_2 budgets in the northern latitudes (e.g., (Byrne et al., (2022)), but data is very limited in the cold season, especially in far-northern regions like the North Slope. ~~While we can constrain the annual net CO_2 budget with existing data, the Arctic is rapidly changing and needs constant monitoring. These recommendations would provide more detailed spatial and seasonal constraints and up-to-date information on the processes driving CO_2 fluxes across the region.~~

4.3.2 Future modeling efforts

The large initial range of potential regional net CO_2 flux values we found for the Alaska North Slope indicates a large sensitivity to choices and assumptions made when scaling eddy flux observations from the site- to regional- scale. The most important of these choices are the representation of the upland tundra, particularly for the response of R_{soil} to T_s during the cold season, and the distribution of vegetation types throughout the domain. Future tundra CO_2 modeling efforts should focus on using site-level data that is the most consistent with regional-scale fluxes, rather than incorporating data from all available sites. Consistency and accuracy in classification schemes used in vegetation maps must also be addressed. As we have shown with the atmospheric observations, not all model scenarios have equal likelihood to be true, and the mean of the model ensemble is not necessarily the most likely or most consistent with the atmosphere. Using these atmospheric observations is uncertain, however, due to potential errors in the transport modeling, which are difficult to quantify. Atmospheric modeling of remote areas such as the Alaska North Slope requires further evaluation and improvement. Further, increasing model temporal resolution should be considered as the importance of the zero-curtain and snow cover to the net CO_2 flux of tundra ecosystems is recognized, both of which vary on the order of days and weeks, rather than months.

5. Conclusions

Observed atmospheric concentrations from aircraft and towers are a powerful tool that provide a regional constraint on the many combinations of possible CO_2 flux parameterizations and distributions of tundra ecosystems on the North Slope of Alaska. We find that the annual regional net CO_2 flux on the North Slope in not a consistent net source or sink, but instead varies between –6 and +6 TgC yr^{-1} for 2012–2017. We can also identify ecosystem relationships and driver combinations that best represent both local CO_2 flux patterns and regional atmospheric CO_2 enhancements. The simulated regional net CO_2 flux is highly sensitive to assumptions made while scaling up eddy flux observations, especially the ecosystem response to T_s~~soil temperature~~ of tundra during the cold season and the spatial distribution of tundra types across the North Slope. Additionally, scaling methods that average observations from multiple eddy covariance flux sites should consider which sites are most representative of the regional impact of the biosphere on the atmosphere using integrative top-down observations.

This work shows that year-round measurements of atmospheric CO_2 concentrations and fluxes across heterogeneous terrestrial and aquatic ecosystems are needed to represent the drivers of CO_2 fluxes from Arctic regions. Arctic ecosystems have the potential to accelerate warming if vast stores of carbon are released or buffer warming if increasing carbon uptake from vegetation occurs. All components of Arctic tundra ecosystems must be fully incorporated into earth system models to improve projections of future climate warming and associated carbon cycle feedbacks.

Data availability

Data that support the findings of this study are available as listed below:
TVPRM NEE for all ensemble simulations: https://doi.org/10.3334/ORNLDAAC/1920.
ICS, ICT, and ICH eddy flux tower observations: http://aon.iab.uaf.edu/data.
IVO, ATQ, BES, BEO, and CMDL eddy flux tower observations: https://doi.org/10.18739/A2X34MS1B.
NOAA BRW tower observations: https://www.esrl.noaa.gov/gmd/dv/data/?site=brw.
ARM-ACME V aircraft observations: https://www.osti.gov/dataexplorer/biblio/dataset/1346549.
ABoVE Arctic-CAP aircraft observations: https://doi.org/10.3334/ORNLDAAC/1658.
NARR meteorology: https://psl.noaa.gov/data/gridded/data.narr.html.
ERA5 meteorology: https://www.ecmwf.int/en/forecasts/dataset/ecmwf-reanalysis-v5.
GOME-2 SIF: https://avdc.gsfc.nasa.gov/pub/data/satellite/MetOp/GOME_F/.
GOSIF: https://globalecology.unh.edu/data/GOSIF.html.
CSIF: http://doi.org/10.6084/m9.figshare.6387494.

CAVM vegetation map: https://www.geobotany.uaf.edu/cavm/.

RasterCAVM vegetation map: https://dx.doi.org/10.17632/c4xj5rv6kv.1.

ABoVE LC vegetation map: https://doi.org/10.3334/ORNLDAAC/1691.

RS-PM T_s~~soil temperature~~: available from authors upon request.

NOAA BRW tower and ARM-ACME V aircraft campaign WRF-STILT footprints: https://doi.org/10.3334/ORNLDAAC/1431, particle trajectories: https://doi.org/10.3334/ORNLDAAC/1430.

ABoVE Arctic-CAP aircraft campaign WRF-STILT footprints: https://doi.org/10.3334/ORNLDAAC/1896, particle trajectories: https://doi.org/10.3334/ORNLDAAC/1895.

Luus et al. (2017) fluxes: https://doi.org/10.3334/ORNLDAAC/1314.

Commane et al. (2017) optimized fluxes: https://doi.org/10.3334/ORNLDAAC/1389.

Natali and~~&~~ Watts et al. (2019) fluxes: https://doi.org/10.3334/ORNLDAAC/1683.

Watts et al. (2021) fluxes: https://doi.org/10.3334/ORNLDAAC/1935.

Author contributions

LDS and RC designed the study. KAA, ESE, JPG, AK, WCO, and DZ provided eddy covariance flux tower data. SCB, KM, and CS provided aircraft concentration data. JMH and MEM provided WRF-STILT particle files and footprints. YY provided RS-PM T_s ~~soil temperature~~ data. JDW provided Watts et al. (2021) cold season belowground CO_2 fluxes. LDS developed and evaluated TVPRM net CO_2 fluxes against observations. RC, EJLL, JWM, and JDW assisted the analysis. LDS wrote the paper. All co-authors contributed to the preparation of the manuscript.

Competing interests

Authors declare that they have no competing interests.

Acknowledgments

We would like to acknowledge that the Alaskan North Slope is home to multiple Alaska Native nations, including the Nunamiut, Gwich'in, Koyukuk, and Iñupiaq peoples. We support and honor the place-based knowledge of Indigenous Peoples and recognize their ancestral and contemporary stewardship of their homelands that we research. LDS and RC are supported by research funding from the Department of Earth and Environmental Sciences at Columbia University and the NASA ABoVE grant #NNX17AC61A. LDS is addtionally supported by the National Science Foundation (NSF) Office of Polar Programs grant #1848620. EJRL and JWM are supported by NASA ABoVE grant #NNX17AE75G. JDW is supported by NASA ABoVE grant #80NSSC19M0209 and NASA grant #NNH17ZDA001N-NIP. Part of the research was carried out at the Jet Propulsion Laboratory, California Institute of Technology, under a contract with NASA (80NM0018D0004). Imnavait Creek flux towers are funded under grants from the NSF Office of Polar Programs, 1503912 and 0632264. Resources supporting JMH and WRF-STILT modeling were provided by NASA grant #NNX17AE75G, #NNX17AC61A, and the NASA High-End Computing (HEC) Program through the NASA Advanced Supercomputing (NAS) Division at Ames Research Center. We thank the R Project community for analysis and plotting tools, especially the ggplot2, ggpattern, magick, anytime, lubridate, raster, and cowplot packages. NCEP Reanalysis data provided by the NOAA/OAR/ESRL PSL, Boulder, Colorado, USA. Some of the data products used in this paper were acquired for the CARVE, a NASA Earth Ventures Sub-orbital (EV-S1) investigation.

References

Arndt, K. A., Oechel, W. C., Goodrich, J. P., Bailey, B. A., Kalhori, A., Hashemi, J., Sweeney, C., and Zona, D.: Sensitivity of Methane Emissions to Later Soil Freezing in Arctic Tundra Ecosystems, J. Geophys. Res. Biogeosci., 124, 2595–2609, https://doi.org/10.1029/2019JG005242, 2019.

Arndt, K. A., Lipson, D. A., Hashemi, J., Oechel, W. C., and Zona, D.: Snow melt stimulates ecosystem respiration in Arctic ecosystems, Global Change Biol., 26, 5042–5051, https://doi.org/10.1111/gcb.15193, 2020.

Bayer, T. K., Gustafsson, E., Brakebusch, M., and Beer, C.: Future Carbon Emission From Boreal and Permafrost Lakes Are Sensitive to Catchment Organic Carbon Loads, J. Geophys. Res. Biogeosci., 124, 1827–1848, https://doi.org/10.1029/2018JG004978, 2019.

Beckebanze, L., Rehder, Z., Holl, D., Wille, C., Mirbach, C., and Kutzbach, L.: Ignoring carbon emissions from thermokarst ponds results in overestimation of tundra net carbon uptake, Biogeosciences, 19, 1225–1244, https://doi.org/10.5194/bg-19-1225-2022, 2022.

Biraud, S., Mei, F., Flynn, C., Hubbe, J., Long, C., Matthews, A., Pekour, M., Sedlacek, A., Springston, S., Tomlinson, J., and Chand, D.: Campaign datasets for ARM Airborne Carbon Measurements (ARM-ACME-V), Oak Ridge National Lab. (ORNL), Oak Ridge, TN (United States). Atmospheric Radiation Measurement (ARM) Archive, https://doi.org/10.5439/1346549, 2016.

Bowling, D. R. and Massman, W. J.: Persistent wind-induced enhancement of diffusive CO2 transport in a mountain forest snowpack, J. Geophys. Res. Biogeosci., 116, G04006, https://doi.org/10.1029/2011JG001722, 2011.

Box, J. E., Colgan, W. T., Christensen, T. R., Schmidt, N. M., Lund, M., Parmentier, F.-J. W., Brown, R., Bhatt, U. S., Euskirchen, E. S., Romanovsky, V. E., Walsh, J. E., Overland, J. E., Wang, M., Corell, R. W., Meier, W. N., Wouters, B., Mernild, S., M\aard, J., Pawlak, J., and Olsen, M. S.: Key indicators of Arctic climate change: 1971–2017, Environ. Res. Lett., 14, 045010, https://doi.org/10.1088/1748-9326/aafc1b, 2019.

Byrne, B., Liu, J., Yi, Y., Chatterjee, A., Basu, S., Cheng, R., Doughty, R., Chevallier, F., Bowman, K. W., Parazoo, N. C., Crisp, D., Li, X., Xiao, J., Sitch, S., Guenet, B., Deng, F., Johnson, M. S., Philip, S., McGuire, P. C., and Miller, C. E.: Multi-year observations reveal a larger than expected autumn respiration signal across northeast Eurasia, Biogeosciences, 19, 4779–4799, https://doi.org/10.5194/bg-19-4779-2022, 2022.

Chang, R. Y.-W., Miller, C. E., Dinardo, S. J., Karion, A., Sweeney, C., Daube, B. C., Henderson, J. M., Mountain, M. E., Eluszkiewicz, J., Miller, J. B., Bruhwiler, L. M. P., and Wofsy, S. C.: Methane emissions from Alaska in 2012 from CARVE airborne observations, PNAS, 111, 16694–16699, https://doi.org/10.1073/pnas.1412953111, 2014.

Commane, R., Lindaas, J., Benmergui, J., Luus, K. A., Chang, R. Y.-W., Daube, B. C., Euskirchen, E. S., Henderson, J. M., Karion, A., Miller, J. B., Miller, S. M., Parazoo, N. C., Randerson, J. T., Sweeney, C., Tans, P., Thoning, K., Veraverbeke, S., Miller, C. E., and Wofsy, S. C.: Carbon dioxide sources from Alaska driven by increasing early winter respiration from Arctic tundra, PNAS, 114, 5361–5366, https://doi.org/10.1073/pnas.1618567114, 2017.

Elder, C. D., Xu, X., Walker, J., Schnell, J. L., Hinkel, K. M., Townsend-Small, A., Arp, C. D., Pohlman, J. W., Gaglioti, B. V., and Czimczik, C. I.: Greenhouse gas emissions from diverse Arctic Alaskan lakes are dominated by young carbon, Nature Clim. Change, 8, 166–171, https://doi.org/10.1038/s41558-017-0066-9, 2018.

Euskirchen, E. S., Bret-Harte, M. S., Scott, G. J., Edgar, C., and Shaver, G. R.: Seasonal patterns of carbon dioxide and water fluxes in three representative tundra ecosystems in northern Alaska, Ecosphere, 3, art4, https://doi.org/10.1890/ES11-00202.1, 2012.

Euskirchen, E. S., Bret-Harte, M. S., Shaver, G. R., Edgar, C. W., and Romanovsky, V. E.: Long-Term Release of Carbon Dioxide from Arctic Tundra Ecosystems in Alaska, Ecosystems, 20, 960–974, https://doi.org/10.1007/s10021-016-0085-9, 2017.

Fisher, J. B., Sikka, M., Oechel, W. C., Huntzinger, D. N., Melton, J. R., Koven, C. D., Ahlström, A., Arain, M. A., Baker, I., Chen, J. M., Ciais, P., Davidson, C., Dietze, M., El-Masri, B., Hayes, D., Huntingford, C., Jain, A. K., Levy, P. E., Lomas, M. R., Poulter, B., Price, D., Sahoo, A. K., Schaefer, K., Tian, H., Tomelleri, E., Verbeeck, H., Viovy, N., Wania, R., Zeng, N., and Miller, C. E.: Carbon cycle uncertainty in the Alaskan Arctic, Biogeosciences, 11, 4271–4288, https://doi.org/10.5194/bg-11-4271-2014, 2014.

Goodrich, J. P., Oechel, W. C., Gioli, B., Moreaux, V., Murphy, P. C., Burba, G., and Zona, D.: Impact of different eddy covariance sensors, site set-up, and maintenance on the annual balance of CO_2 and CH_4 in the harsh Arctic environment, Agr. Forest Meteorol., 228–229, 239–251, https://doi.org/10.1016/j.agrformet.2016.07.008, 2016.

Hartery, S., Commane, R., Lindaas, J., Sweeney, C., Henderson, J., Mountain, M., Steiner, N., McDonald, K., Dinardo, S. J., Miller, C. E., Wofsy, S. C., and Chang, R. Y.-W.: Estimating regional-scale methane flux and budgets using CARVE aircraft measurements over Alaska, Atmos. Chem. Phys., 18, 185–202, https://doi.org/10.5194/acp-18-185-2018, 2018.

Henderson, J. M., Eluszkiewicz, J., Mountain, M. E., Nehrkorn, T., Chang, R. Y.-W., Karion, A., Miller, J. B., Sweeney, C., Steiner, N., Wofsy, S. C., and Miller, C. E.: Atmospheric transport simulations in support of the Carbon in Arctic Reservoirs Vulnerability Experiment (CARVE), Atmos. Chem. Phys., 15, 4093–4116, https://doi.org/10.5194/acp-15-4093-2015, 2015.

Hersbach, H., Bell, B., Berrisford, P., Hirahara, S., Horányi, A., Muñoz-Sabater, J., Nicolas, J., Peubey, C., Radu, R., Schepers, D., Simmons, A., Soci, C., Abdalla, S., Abellan, X., Balsamo, G., Bechtold, P., Biavati, G., Bidlot, J., Bonavita, M., Chiara, G. D., Dahlgren, P., Dee, D., Diamantakis, M., Dragani, R., Flemming, J., Forbes, R., Fuentes, M., Geer, A., Haimberger, L., Healy, S., Hogan, R. J., Hólm, E., Janisková, M., Keeley, S., Laloyaux, P., Lopez, P., Lupu, C., Radnoti, G., Rosnay, P. de, Rozum, I., Vamborg, F., Villaume, S., and Thépaut, J.-N.: The ERA5 global reanalysis, Q. J. Roy. Meteorol. Soc., 146, 1999–2049, https://doi.org/10.1002/qj.3803, 2020.

Holgerson, M. A. and Raymond, P. A.: Large contribution to inland water CO_2 and CH_4 emissions from very small ponds, Nat. Geosci., 9, 222–226, https://doi.org/10.1038/ngeo2654, 2016.

Hugelius, G., Strauss, J., Zubrzycki, S., Harden, J. W., Schuur, E. a. G., Ping, C.-L., Schirrmeister, L., Grosse, G., Michaelson, G. J., Koven, C. D., O'Donnell, J. A., Elberling, B., Mishra, U., Camill, P., Yu, Z., Palmtag, J., and Kuhry, P.: Estimated stocks of circumpolar permafrost carbon with quantified uncertainty ranges and identified data gaps, Biogeosciences, 11, 6573–6593, https://doi.org/10.5194/bg-11-6573-2014, 2014.

Jeong, S.-J., Bloom, A. A., Schimel, D., Sweeney, C., Parazoo, N. C., Medvigy, D., Schaepman-Strub, G., Zheng, C., Schwalm, C. R., Huntzinger, D. N., Michalak, A. M., and Miller, C. E.: Accelerating rates of Arctic carbon cycling revealed by long-term atmospheric CO2 measurements, Sci. Adv., 4, eaao1167, https://doi.org/10.1126/sciadv.aao1167, 2018.

Joiner, J., Yoshida, Y., Guanter, L., and Middleton, E. M.: New methods for the retrieval of chlorophyll red fluorescence from hyperspectral satellite instruments: simulations and application to GOME-2 and SCIAMACHY, Atmos. Meas. Tech., 9, 3939–3967, https://doi.org/10.5194/amt-9-3939-2016, 2016.

Karion, A., Sweeney, C., Kort, E. A., Shepson, P. B., Brewer, A., Cambaliza, M., Conley, S. A., Davis, K., Deng, A., Hardesty, M., Herndon, S. C., Lauvaux, T., Lavoie, T., Lyon, D., Newberger, T., Pétron, G., Rella, C., Smith, M., Wolter, S., Yacovitch, T. I., and Tans, P.: Aircraft-Based Estimate of Total Methane Emissions from the Barnett Shale Region, Environ. Sci. Technol., 49, 8124–8131, https://doi.org/10.1021/acs.est.5b00217, 2015.

Kim, J., Kim, Y., Zona, D., Oechel, W., Park, S.-J., Lee, B.-Y., Yi, Y., Erb, A., and Schaaf, C. L.: Carbon response of tundra ecosystems to advancing greenup and snowmelt in Alaska, Nat. Commun., 12, 6879, https://doi.org/10.1038/s41467-021-26876-7, 2021.

Kim, Y., Kimball, J. S., Zhang, K., and McDonald, K. C.: Satellite detection of increasing Northern Hemisphere non-frozen seasons from 1979 to 2008: Implications for regional vegetation growth, Remote Sens. Environ., 121, 472–487, https://doi.org/10.1016/j.rse.2012.02.014, 2012.

Kittler, F., Eugster, W., Foken, T., Heimann, M., Kolle, O., and Göckede, M.: High-quality eddy-covariance CO2 budgets under cold climate conditions, J. Geophys. Res. Biogeosci., 122, 2064–2084, https://doi.org/10.1002/2017JG003830, 2017.

Larson, E. J. L., Schiferl, L. D., Commane, R., Munger, J. W., Trugman, A. T., Ise, T., Euskirchen, E. S., Wofsy, S., and Moorcroft, P. M.: The changing carbon balance of tundra ecosystems: results from a vertically-resolved peatland biosphere model, Environ. Res. Lett., 17, 014019, https://doi.org/10.1088/1748-9326/ac4070, 2021.

Li, X. and Xiao, J.: A Global, 0.05-Degree Product of Solar-Induced Chlorophyll Fluorescence Derived from OCO-2, MODIS, and Reanalysis Data, Remote Sens., 11, 517, https://doi.org/10.3390/rs11050517, 2019.

Luus, K. A., Commane, R., Parazoo, N. C., Benmergui, J., Euskirchen, E. S., Frankenberg, C., Joiner, J., Lindaas, J., Miller, C. E., Oechel, W. C., Zona, D., Wofsy, S., and Lin, J. C.: Tundra photosynthesis captured by satellite-observed solar-induced chlorophyll fluorescence, Geophys. Res. Lett., 44, 2016GL070842, https://doi.org/10.1002/2016GL070842, 2017.

Magney, T. S., Bowling, D. R., Logan, B. A., Grossmann, K., Stutz, J., Blanken, P. D., Burns, S. P., Cheng, R., Garcia, M. A., Köhler, P., Lopez, S., Parazoo, N. C., Raczka, B., Schimel, D., and Frankenberg, C.: Mechanistic evidence for tracking the seasonality of photosynthesis with solar-induced fluorescence, PNAS, 116, 11640–11645, https://doi.org/10.1073/pnas.1900278116, 2019.

Magnússon, R. Í., Limpens, J., van Huissteden, J., Kleijn, D., Maximov, T. C., Rotbarth, R., Sass-Klaassen, U., and Heijmans, M. M. P. D.: Rapid Vegetation Succession and Coupled Permafrost Dynamics in Arctic Thaw Ponds in the Siberian Lowland Tundra, J. Geophys. Res. Biogeosci., 125, 2019JG005618, https://doi.org/10.1029/2019JG005618, 2020.

Mbufong, H. N., Lund, M., Aurela, M., Christensen, T. R., Eugster, W., Friborg, T., Hansen, B. U., Humphreys, E. R., Jackowicz-Korczynski, M., Kutzbach, L., Lafleur, P. M., Oechel, W. C., Parmentier, F. J. W., Rasse, D. P., Rocha, A. V., Sachs, T., van der Molen, M. K., and Tamstorf, M. P.: Assessing the spatial variability in peak season CO_2 exchange characteristics across the Arctic tundra using a light response curve parameterization, Biogeosciences, 11, 4897–4912, https://doi.org/10.5194/bg-11-4897-2014, 2014.

Meredith, M., Sommerkorn, M., Cassotta, S., Derksen, C., Ekaykin, A., Hollowed, A., Kofinas, G., Mackintosh, A., Melbourne-Thomas, J., Muelbert, M. M. C., Ottersen, G., Pritchard, H., and Schuur, E. A. G.: Polar Regions, in: IPCC Special Report on the Ocean and Cryosphere in a Changing Climate, edited by: Pörtner, H.-O., Roberts, D. C., Masson-Delmotte, V., Zhai, P., Tignor, M., Poloczanska, E., Mintenbeck, K., Alegría, A., Nicolai, M., Okem, A., Petzold, J., Rama, B., and Weyer, N. M., 2019.

Mesinger, F., DiMego, G., Kalnay, E., Mitchell, K., Shafran, P. C., Ebisuzaki, W., Jović, D., Woollen, J., Rogers, E., Berbery, E. H., Ek, M. B., Fan, Y., Grumbine, R., Higgins, W., Li, H., Lin, Y., Manikin, G., Parrish, D., and Shi, W.: North American Regional Reanalysis, B. Am. Meteorol. Soc., 87, 343–360, https://doi.org/10.1175/BAMS-87-3-343, 2006.

Miller, S. M., Miller, C. E., Commane, R., Chang, R. Y.-W., Dinardo, S. J., Henderson, J. M., Karion, A., Lindaas, J., Melton, J. R., Miller, J. B., Sweeney, C., Wofsy, S. C., and Michalak, A. M.: A multiyear estimate of methane fluxes in Alaska from CARVE atmospheric observations, Global Biogeochem. Cycles, 30, 1441–1453, https://doi.org/10.1002/2016GB005419, 2016.

Natali, S. M., Watts, J. D., Rogers, B. M., Potter, S., Ludwig, S. M., Selbmann, A.-K., Sullivan, P. F., Abbott, B. W., Arndt, K. A., Birch, L., Björkman, M. P., Bloom, A. A., Celis, G., Christensen, T. R., Christiansen, C. T., Commane, R., Cooper, E. J., Crill, P., Czimczik, C., Davydov, S., Du, J., Egan, J. E., Elberling, B., Euskirchen, E. S., Friborg, T., Genet, H., Göckede, M., Goodrich, J. P., Grogan, P., Helbig, M., Jafarov, E. E., Jastrow, J. D., Kalhori, A. A. M., Kim, Y., Kimball, J. S., Kutzbach, L., Lara, M. J., Larsen, K. S., Lee, B.-Y., Liu, Z., Loranty, M. M., Lund, M., Lupascu, M., Madani, N., Malhotra, A., Matamala, R., McFarland, J., McGuire, A. D., Michelsen, A., Minions, C., Oechel, W. C., Olefeldt, D., Parmentier, F.-J. W., Pirk, N., Poulter, B., Quinton, W., Rezanezhad, F., Risk, D., Sachs, T., Schaefer, K., Schmidt, N. M., Schuur, E. A. G., Semenchuk, P. R., Shaver, G., Sonnentag, O., Starr, G., Treat, C. C., Waldrop, M. P., Wang, Y., Welker, J., Wille, C., Xu, X., Zhang, Z., Zhuang, Q., and Zona, D.: Large loss of CO 2 in winter observed across the northern permafrost region, Nat. Clim. Change, 9, 852–857, https://doi.org/10.1038/s41558-019-0592-8, 2019.

Oechel, W. C., Laskowski, C. A., Burba, G., Gioli, B., and Kalhori, A. A. M.: Annual patterns and budget of CO2 flux in an Arctic tussock tundra ecosystem, J. Geophys. Res. Biogeosci., 119, 323–339, https://doi.org/10.1002/2013JG002431, 2014.

Outcalt, S. I., Nelson, F. E., and Hinkel, K. M.: The zero-curtain effect: Heat and mass transfer across an isothermal region in freezing soil, Water Resour. Res., 26, 1509–1516, https://doi.org/10.1029/WR026i007p01509, 1990.

Pallandt, M. M. T. A., Kumar, J., Mauritz, M., Schuur, E. A. G., Virkkala, A.-M., Celis, G., Hoffman, F. M., and Göckede, M.: Representativeness assessment of the pan-Arctic eddy covariance site network and optimized future enhancements, Biogeosciences, 19, 559–583, https://doi.org/10.5194/bg-19-559-2022, 2022.

Patankar, R., Mortazavi, B., Oberbauer, S. F., and Starr, G.: Diurnal patterns of gas-exchange and metabolic pools in tundra plants during three phases of the arctic growing season, Ecol. Evol., 3, 375–388, https://doi.org/10.1002/ece3.467, 2013.

Porcar-Castell, A., Tyystjärvi, E., Atherton, J., van der Tol, C., Flexas, J., Pfündel, E. E., Moreno, J., Frankenberg, C., and Berry, J. A.: Linking chlorophyll a fluorescence to photosynthesis for remote sensing applications: mechanisms and challenges, J. Exp. Bot., 65, 4065–4095, https://doi.org/10.1093/jxb/eru191, 2014.

Raynolds, M. K., Walker, D. A., Balser, A., Bay, C., Campbell, M., Cherosov, M. M., Daniëls, F. J. A., Eidesen, P. B., Ermokhina, K. A., Frost, G. V., Jedrzejek, B., Jorgenson, M. T., Kennedy, B. E., Kholod, S. S., Lavrinenko, I. A., Lavrinenko, O. V., Magnússon, B., Matveyeva, N. V., Metúsalemsson, S., Nilsen, L., Olthof, I., Pospelov, I. N., Pospelova, E. B., Pouliot, D., Razzhivin, V., Schaepman-Strub, G., Šibík, J., Telyatnikov, M. Yu., and Troeva, E.: A raster version of the Circumpolar Arctic Vegetation Map (CAVM), Remote Sens. Environ., 232, 111297, https://doi.org/10.1016/j.rse.2019.111297, 2019.

Romanovsky, V. E. and Osterkamp, T. E.: Effects of unfrozen water on heat and mass transport processes in the active layer and permafrost, Permafrost Periglac., 11, 219–239, https://doi.org/10.1002/1099-1530(200007/09)11:3<219::AID-PPP352>3.0.CO;2-7, 2000.

Schuur, E. A. G., McGuire, A. D., Schädel, C., Grosse, G., Harden, J. W., Hayes, D. J., Hugelius, G., Koven, C. D., Kuhry, P., Lawrence, D. M., Natali, S. M., Olefeldt, D., Romanovsky, V. E., Schaefer, K., Turetsky, M. R., Treat, C. C., and Vonk, J. E.: Climate change and the permafrost carbon feedback, Nature, 520, 171–179, https://doi.org/10.1038/nature14338, 2015.

Sun, Y., Frankenberg, C., Wood, J. D., Schimel, D. S., Jung, M., Guanter, L., Drewry, D. T., Verma, M., Porcar-Castell, A., Griffis, T. J., Gu, L., Magney, T. S., Köhler, P., Evans, B., and Yuen, K.: OCO-2 advances photosynthesis observation from space via solar-induced chlorophyll fluorescence, Science, 358, eaam5747, https://doi.org/10.1126/science.aam5747, 2017.

Sweeney, C. and McKain, K.: ABoVE: Atmospheric Profiles of CO, CO2 and CH4 Concentrations from Arctic-CAP, 2017, ORNL DAAC, https://doi.org/10.3334/ORNLDAAC/1658, 2019.

Sweeney, C., Dlugokencky, E., Miller, C. E., Wofsy, S., Karion, A., Dinardo, S., Chang, R. Y.-W., Miller, J. B., Bruhwiler, L., Crotwell, A. M., Newberger, T., McKain, K., Stone, R. S., Wolter, S. E., Lang, P. E., and Tans, P.: No significant increase in long-term CH4 emissions on North Slope of Alaska despite significant increase in air temperature, Geophys. Res. Lett., 43, 6604–6611, https://doi.org/10.1002/2016GL069292, 2016.

Sweeney, C., Chatterjee, A., Wolter, S., McKain, K., Bogue, R., Conley, S., Newberger, T., Hu, L., Ott, L., Poulter, B., Schiferl, L., Weir, B., Zhang, Z., and Miller, C. E.: Using atmospheric trace gas vertical profiles to evaluate model fluxes: a case study of Arctic-CAP observations and GEOS simulations for the ABoVE domain, Atmos. Chem. Phys., 22, 6347–6364, https://doi.org/10.5194/acp-22-6347-2022, 2022.

Tadić, J. M., Miller, S., Yadav, V., and Biraud, S. C.: Greenhouse gas fluxes from Alaska's North Slope inferred from the Airborne Carbon Measurements Campaign (ACME-V), Atmos. Environ., 118239, https://doi.org/10.1016/j.atmosenv.2021.118239, 2021.

Tan, Z., Zhuang, Q., Shurpali, N. J., Marushchak, M. E., Biasi, C., Eugster, W., and Anthony, K. W.: Modeling CO2 emissions from Arctic lakes: Model development and site-level study, J. Adv. Model. Earth Syst., 9, 2190–2213, https://doi.org/10.1002/2017MS001028, 2017.

Tao, J., Zhu, Q., Riley, W. J., and Neumann, R. B.: Warm-season net CO$\less$sub$\greater$2$\less$/sub$\greater$ uptake outweighs cold-season emissions over Alaskan North Slope tundra under current and RCP8.5 climate, Environ. Res. Lett., 16, 055012, https://doi.org/10.1088/1748-9326/abf6f5, 2021.

Walker, D. A., Raynolds, M. K., Daniëls, F. J. A., Einarsson, E., Elvebakk, A., Gould, W. A., Katenin, A. E., Kholod, S. S., Markon, C. J., Melnikov, E. S., Moskalenko, N. G., Talbot, S. S., Yurtsev, B. A. (†), and Team, T. other members of the C.: The Circumpolar Arctic vegetation map, J. Veg. Sci., 16, 267–282, https://doi.org/10.1111/j.1654-1103.2005.tb02365.x, 2005.

Wang, J. A., Sulla-Menashe, D., Woodcock, C. E., Sonnentag, O., Keeling, R. F., and Friedl, M. A.: Extensive land cover change across Arctic–Boreal Northwestern North America from disturbance and climate forcing, Global Change Biol., 26, 807–822, https://doi.org/10.1111/gcb.14804, 2020.

Watts, J. D., Natali, S. M., Minions, C., Risk, D., Arndt, K., Zona, D., Euskirchen, E. S., Rocha, A. V., Sonnentag, O., Helbig, M., Kalhori, A., Oechel, W., Ikawa, H., Ueyama, M., Suzuki, R., Kobayashi, H., Celis, G., Schuur, E. A. G., Humphreys, E., Kim, Y., Lee, B.-Y., Goetz, S., Madani, N., Schiferl, L. D., Commane, R., Kimball, J. S., Liu, Z., Torn, M. S., Potter, S., Wang, J. A., Jorgenson, M. T., Xiao, J., Li, X., and Edgar, C.: Soil respiration strongly offsets carbon uptake in Alaska and Northwest Canada, Environ. Res. Lett., 16, 084051, https://doi.org/10.1088/1748-9326/ac1222, 2021.

Worthy, D. E. J., Chan, E., Ishizawa, M., Chan, D., Poss, C., Dlugokencky, E. J., Maksyutov, S., and Levin, I.: Decreasing anthropogenic methane emissions in Europe and Siberia inferred from continuous carbon dioxide and methane observations at Alert, Canada, J. Geophys. Res. Atmos., 114, https://doi.org/10.1029/2008JD011239, 2009.

Yang, X., Tang, J., Mustard, J. F., Lee, J.-E., Rossini, M., Joiner, J., Munger, J. W., Kornfeld, A., and Richardson, A. D.: Solar-induced chlorophyll fluorescence that correlates with canopy photosynthesis on diurnal and seasonal scales in a temperate deciduous forest, Geophys. Res. Lett., 42, 2977–2987, https://doi.org/10.1002/2015GL063201, 2015.

Yi, Y., Kimball, J. S., Chen, R. H., Moghaddam, M., Reichle, R. H., Mishra, U., Zona, D., and Oechel, W. C.: Characterizing permafrost active layer dynamics and sensitivity to landscape spatial heterogeneity in Alaska, Cryosphere, 12, 145–161, https://doi.org/10.5194/tc-12-145-2018, 2018.

Yi, Y., Kimball, J. S., Chen, R. H., Moghaddam, M., and Miller, C. E.: Sensitivity of active-layer freezing process to snow cover in Arctic Alaska, Cryosphere, 13, 197–218, https://doi.org/10.5194/tc-13-197-2019, 2019.

Zhang, Y., Joiner, J., Alemohammad, S. H., Zhou, S., and Gentine, P.: A global spatially contiguous solar-induced fluorescence (CSIF) dataset using neural networks, Biogeosciences, 15, 5779–5800, https://doi.org/10.5194/bg-15-5779-2018, 2018.

Zhang, Y., Commane, R., Zhou, S., Williams, A. P., and Gentine, P.: Light limitation regulates the response of autumn terrestrial carbon uptake to warming, Nat. Clim. Change, 10, 739–743, https://doi.org/10.1038/s41558-020-0806-0, 2020.

Zona, D., Gioli, B., Commane, R., Lindaas, J., Wofsy, S. C., Miller, C. E., Dinardo, S. J., Dengel, S., Sweeney, C., Karion, A., Chang, R. Y.-W., Henderson, J. M., Murphy, P. C., Goodrich, J. P., Moreaux, V., Liljedahl, A., Watts, J. D., Kimball, J. S., Lipson, D. A., and Oechel, W. C.: Cold season emissions dominate the Arctic tundra methane budget, PNAS, 113, 40–45, https://doi.org/10.1073/pnas.1516017113, 2016.

Supplement of

Using atmospheric observations to quantify annual biogenic carbon dioxide fluxes on the Alaska North Slope

Luke D. Schiferl, Jennifer D. Watts, Erik J. L. Larson, Kyle A. Arndt, Sébastien C. Biraud, Eugénie S. Euskirchen, Jordan P. Goodrich, John M. Henderson, Aram Kalhori, Kathryn McKain, Marikate E. Mountain, J. William Munger, Walter C. Oechel, Colm Sweeney, Yonghong Yi, Donatella Zona, and Róisín Commane

Correspondence to: Luke D. Schiferl (schiferl@ldeo.columbia.edu)

S1 Determining Tundra Vegetation Photosynthesis and Respiration Model (TVPRM) variable parameters using observed net CO_2 flux

The TPVRM variable parameters (α_s [units: μmol CO_2 m^{-2} s^{-1} °C^{-1}], β_s [μmol CO_2 m^{-2} s^{-1}], α_a [μmol CO_2 m^{-2} s^{-1} °C^{-1}], β_a [μmol CO_2 m^{-2} s^{-1}], λ [μmol CO_2 m^{-2} s^{-1} (μmol photon m^{-2} s^{-1} mW m^{-2} nm^{-1} sr^{-1})$^{-1}$], and PAR_0 [μmol photon m^{-2} s^{-1}] are calculated for each 365-day period using a moving window (i.e., day 1–365, day 2–366, day 3–367, etc.) for 2013 to 2017 as follows:

Step 1: *Linear regression of observed net CO_2 flux against soil temperature (T_s) during non-growing season to determine α_s and β_s and calculate soil respiration (R_{soil}).* Daily mean T_s and the corresponding daily mean observed net CO_2 flux during potential non-growing days (daily maximum air temperature (T_a) < 0°C) when SIF = 0 and 50% of the half-hours have observed net CO_2 flux are identified and sorted into 5% bins by ordering the daily mean T_s. Regression is performed on the 20 median observed net CO_2 flux and T_s values calculated from these bins.~~, determined by 5% bins of ordered daily mean T_s and the corresponding daily mean observed net CO_2 flux, from the potential non-growing days (daily maximum air temperature (T_a) < 0°C) when SIF = 0 and 50% of the half-hours have observed net CO_2 flux.~~ Daily values are used here to account for the lack of variability in T_s from reanalysis products on sub-daily timescales. The binning approach distributes the influence of low-end T_s values more evenly in the regression, which is needed because the distribution of T_s values is non-normal, with a majority of points just below 0°C during the long zero-curtain period.

Step 2: *Linear regression of observed net CO_2 flux against T_a during growing-season night to determine α_a and β_a and calculate plant respiration (R_{plant}).* Half-hourly T_a and the corresponding half-hourly observed net CO_2 flux with R_{soil} (calculated in step 1) removed during potential growing days (daily minimum T_a > 0°C) when solar-induced chlorophyll fluorescence (SIF) > 0 and photosynthetically active radiation (PAR) <= 4 μmol photon m^{-2} s^{-1} are identified and sorted into 5% bins by ordering the half-hourly T_a. Regression is performed on the 20 median observed net CO_2 flux with R_{soil} ~~(calculated in step 1)~~ removed and T_a values calculated from these bins.~~, determined by 5% bins of ordered half-hourly T_a and the corresponding half-hourly observed net CO_2 flux with R_{soil} removed, from the potential growing days (daily minimum T_a >~~

~~0°C) when solar-induced chlorophyll fluorescence (SIF) > 0 and photosynthetically active radiation (PAR) <= 4 µmol photon m^{-2} s^{-1}.~~ The binning approach distributes the influence of T_a values more evenly in the regression, which is needed because distribution of values is sporadic and variable as data from the light-limited growing season is limited to August and the number of total points available is only ~10% of those used in the R_{soil} fit.

Step 3: *Nonlinear fitting of observed net CO_2 flux against PAR, SIF, and T_a during growing-season day to determine λ and PAR_0 and calculate gross primary productivity (GPP).* Fitting is performed using nonlinear least squares (nls) on the half-hourly observed net CO_2 flux with R_{soil} and R_{plant} (calculated in steps 1 and 2, respectively) removed and half-hourly PAR, SIF (constant daily value) and T_a (used to calculate the temperature scalar (T_{scale}) from the potential growing days when SIF > 0 and PAR > 4 µmol photon m^{-2} s^{-1}. Initial values for nls are PAR_0 = 240 and λ = 0.04, which were reported as shrub tundra parameter values by ~~(~~Luus et al.~~,~~ (2017).

Each 365-day period must have valid data (observed net CO_2 flux, reanalyzed T_a, T_s and PAR, and derived SIF) for 70% of potential growing days and 50% of potential non-growing days in order for variable parameters to be calculated. This requirement is most often failed due to gaps in the observed net CO_2 flux. In order to mitigate unrealistic observed non-growing season uptake outside of noise, prior to step 1, we remove half-hourly observed net CO_2 flux values during 24-hour periods on non-growing days when 50% of half-hours have observed net CO_2 flux and both 50% and the mean of those observed net CO_2 flux values are negative. For each step, data are removed when net CO_2 flux values are outside of three standard deviations of the mean.

The moving window method accounts for variability in both day-to-day data availability and year-to-year ecosystem response to environmental drivers (parameterization). The median value for each variable parameter from the set of valid 365-day periods is used in the site-level net CO_2 flux evaluation (see Sect. S4, Fig. S4) and regional scaling. These median variable parameters are determined for each combination of input reanalysis meteorology and SIF product at each eddy covariance flux tower site.

The main components of the procedures for steps 1-3 above (i.e., linear regressions respiration, non-linear regression for GPP) largely follow that of the previous version of this empirical CO_2 flux model described by ~~(~~Luus et al.~~,~~ (2017). However, instead of using snow cover as the indicator of T_a-driven total respiration (no snow) or T_s-driven total respiration (snow), as in ~~(~~Luus et al.~~,~~ (2017), we separate respiration into R_{soil} and R_{plant} components, which explicitly represent heterotrophic and autotrophic respiration communities, respectively. R_{soil} is now applied year-round, with R_{plant} applied during the growing season as determined by SIF. This change also simplifies the required model inputs to only reanalysis data and SIF.

The threshold criteria described above for performing a regression calculation during a particular window and for filtering data used in the regressions were chosen to balance maintaining representativeness of the various regressions (i.e., data is available from throughout the entire time period) and keeping enough data to be useful for a stable fit (i.e., non-growing season data is more limited). The methods for determining the TPVRM parameters described here also result in the best version of the model compared to observations after many development iterations.

S2 Meteorological reanalysis and other T_s ~~soil temperature~~ products used by TVPRM

Meteorological reanalysis products used by TPVRM are shown in Table S4~~3~~. Downward shortwave radiation product (dswrf, ssrd) values are converted to PAR using a conversion factor of 1.98. Meteorology values are linearly interpolated to half-hourly (T_a, PAR) and averaged to daily (T_s) for model parameter calculation and site-level net CO_2 flux evaluation. NARR values are linearly interpolated to hourly for regional simulations. Site-level calculations are made using values from the meteorological product gridbox corresponding to site location. Meteorological product horizontal resolution is maintained for regional simulations.

For TVPRM simulations driven by T_s from the Remote Sensing driven Permafrost Model (RS-PM (Yi et al., 2018, 2019)), we linearly interpolate RS-PM T_s from 8 day to daily values and horizontally regrid from 1 km to match the other meteorological data by averaging all native pixel center points within each meteorological reanalysis product gridbox. When sub-daily RS-PM T_s is needed to calculate the simulated net CO_2 flux, we apply a constant value. We tested the use of all RS-PM T_s depths from 1 cm to 105 cm and found varying performance, with T_s from deeper layers improving the TVPRM performance at sites with greater soil thickness. For consistent comparison to NARR, we use RS-PM T_s at 8 cm depth in our analysis here.

We also tested using multi-layer fit driven by soil column temperature. In this approach, we summed the degrees above a freezing threshold (-0.75°C at IVO, -5°C at CMDL) representing the zero-curtain time period for each layer, multiplied by the layer thickness. This column sum temperature above freezing was used in place of the single layer T_s above in the same linear fit process to determine parameters which represent R_{soil}. While likely more realistic in driving R_{soil} than a single layer approach, applying the multi-layer sum to our constrained TVPRM member did not result in significantly higher early cold season (Sep–Dec) CO_2 emissions needed to match the observations since both cases match well to the eddy flux measurements.

S3 SIF products used by TVPRM

SIF products used by TPVRM are shown in Table S5~~4~~. GOSIF and CSIF are linearly interpolated to daily values and horizontally regridded by averaging all native pixel center points within each meteorological reanalysis product gridbox. Any resulting negative values for all products are set to 0. Site-level SIF values correspond to the site latitude (GOME-2) or site location within a meteorology gridbox (GOSIF, CSIF). Regional simulation GOME-2 values correspond to the meteorology gridbox center point latitude.

S4 Evaluation of site-level net CO_2 flux against observations

We calculate the TVPRM net CO_2 flux at half-hourly time resolution using the median variable parameters determined above for each eddy flux site for each combination of reanalysis meteorology and SIF product. We then evaluate the simulated net CO_2 flux against the observed net CO_2 flux for each eddy flux site over various averaging lengths (half-hour, one day, two weeks) for various timeframes (year-round, growing season, non-growing season). Elements of this evaluation are shown in Fig. S4. For this evaluation, we calculated the coefficient of determination (R^2) as the square of the Pearson correlation coefficient for all points. The slope (m) is determined by ordinary least squares using the median of each 10% bin of ordered observed and corresponding simulated net CO_2 flux. The normalized mean bias (NMB) of all points is defined as $\frac{\sum(\text{simulated} - \text{observed})}{\sum \text{observed}}$. The root-mean-square error (RMSE) of all points is defined as $\sqrt{(\text{simulated} - \text{observed})^2}$.

Generally, site-level TVPRM performance is greater (higher correlation, slope closer to 1, lower bias and error) in the growing season compared to the non-growing season. Performance improves in all seasons as the timescale of averaging is lengthened, with the non-growing season notably better on the two-week scale, as T_s ~~soil temperatures~~ does not fluctuate much on the half-hourly to daily scale. Intersite performance is more variable compared to the model performance trends across seasons and timescales. The relative quality of model performance at each site is likely due to the data availability for that site for a given averaging length or timeframe.

S5 Scaling TVPRM from site-level to regional net CO_2 flux

To scale from site-level to regional net CO_2 flux, we first calculate the hourly TVPRM net CO_2 flux at each meteorological gridbox for each median variable parameter set from the eight eddy flux sites. The regional simulated net CO_2 flux at each gridbox is then determined by weighting the site-specific net CO_2 flux by the fraction of each vegetation type within that gridbox based on the classifications of inland tundra, coastal tundra, other land, inland water, and ocean. For each regional simulation, we assume all inland tundra is represented by the parameterization from one of four sites (ICS, ICH, ICT, IVO) and all coastal tundra is represented by one of the remaining sites (ATQ, BES, BEO, CMDL). This method allows for separation and testing of distinct site-level responses within each group. Figure S1 shows the distinct response of TVPRM using variable parameters from these two groups as demonstrated by the cross-site evaluation. Net CO_2 fluxes from other land, inland water, and ocean areas are set to 0.

The vegetation maps used to determine the fraction of each classification are described in Table S6~~5~~. We group CAVM and RasterCAVM classifications for graminoid and shrub tundra into our inland tundra classification, with wetland tundra classifications used as coastal tundra. Barren, glacier, and ice/snow classifications are set to other land, and water classifications remain separate for inland water and ocean. ABoVE LC classifications are grouped into our classification scheme by vegetation description and spatial distribution. CAVM and RasterCAVM are proportionally scaled to match ABoVE LC for other land, inland water, and ocean, so inland and coastal tundra are the only variations between the vegetation maps. Figure S5 shows the distribution and percentage of these grouped classifications within our North Slope domain.

Spatial distribution maps throughout this study are produced by rasterizing native NARR and ERA5 gridboxes to 1 km boxes on the NASA Arctic-Boreal Vulnerability Experiment (ABoVE) standard projection and grid (https://above.nasa.gov/implementation_plan/standard_projection.html) and aggregating these boxes to 30 km, consistent with the native spatial resolution. Regional flux values are calculated using gridbox fluxes on native resolution.

Supplemental Figures

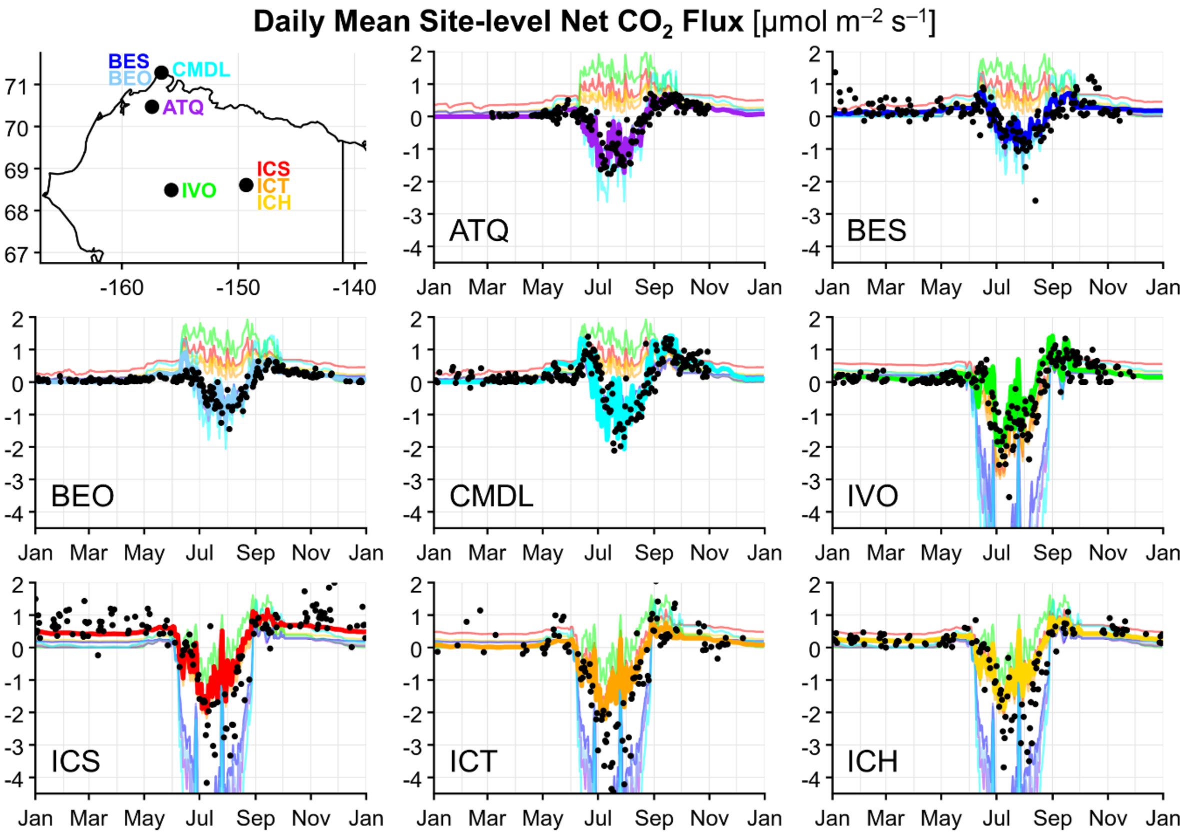

Figure S1. Timeseries of daily mean site-level net CO_2 flux for 2014 at eddy flux measurement sites on the Alaska North Slope (top left panel) used to determine TVPRM parameters. For the cross-site evaluation, each site panel uses the meteorology and SIF at that site to calculate the TVPRM simulated net CO_2 flux using the parameters determined for all sites, with the colored lines corresponding to the sites in the top left panel. ~~Colored lines shows TVPRM simulated net CO_2 flux using parameters for each of the eight sites that is~~ Here we show TVPRM net CO_2 flux driven by NARR meteorology and the CSIF SIF product, ~~at each site location (individual panes). Lines for~~ where the net CO_2 flux for corresponding ~~matching~~ site parameters and locations are highlighted using lines with heavier weight. Black dots show observed net CO_2 flux at each site. ~~Locations of eddy flux measurement sites on the Alaska North Slope shown in upper left.~~

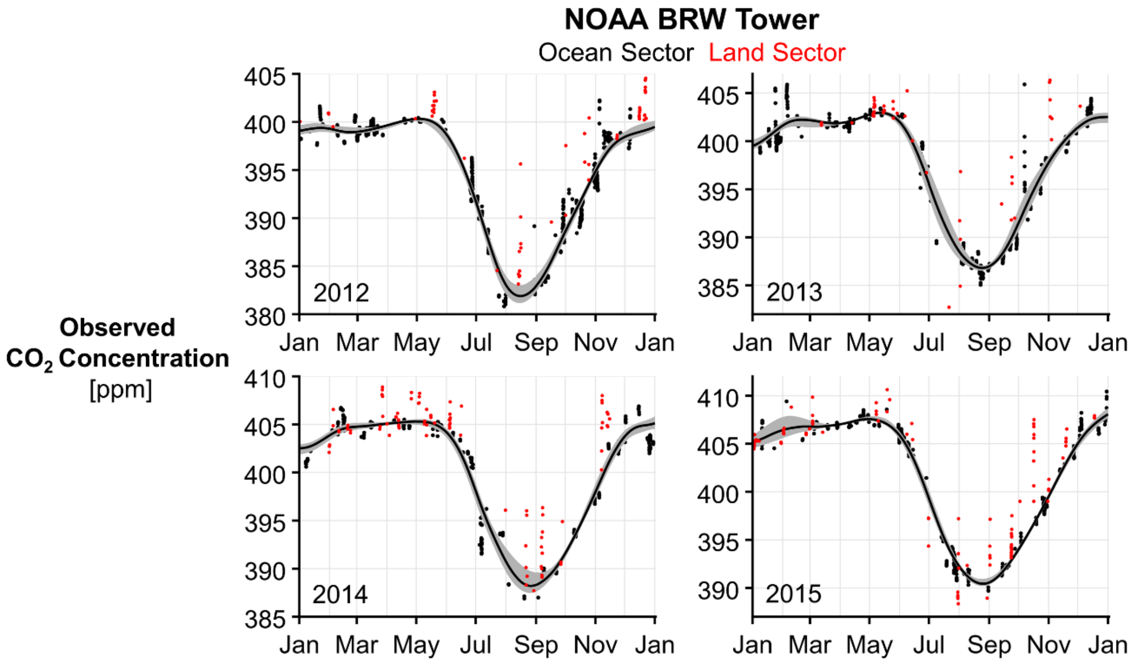

Figure S2. Timeseries of calculated NOAA BRW tower ocean sector CO_2 background concentration (black line) for 2012–2015. Uncertainty (95% of results) determined by varying start time of spline fit and repeatedly randomly removing 50% of used points shown by gray ribbon. Black dots indicate ocean sector hourly observations used in spline fit, and red dots indicate land sector hourly observations used in model evaluation (Figs. 2c–2d, 3b–3c, 4a, 4c, S11, S14).

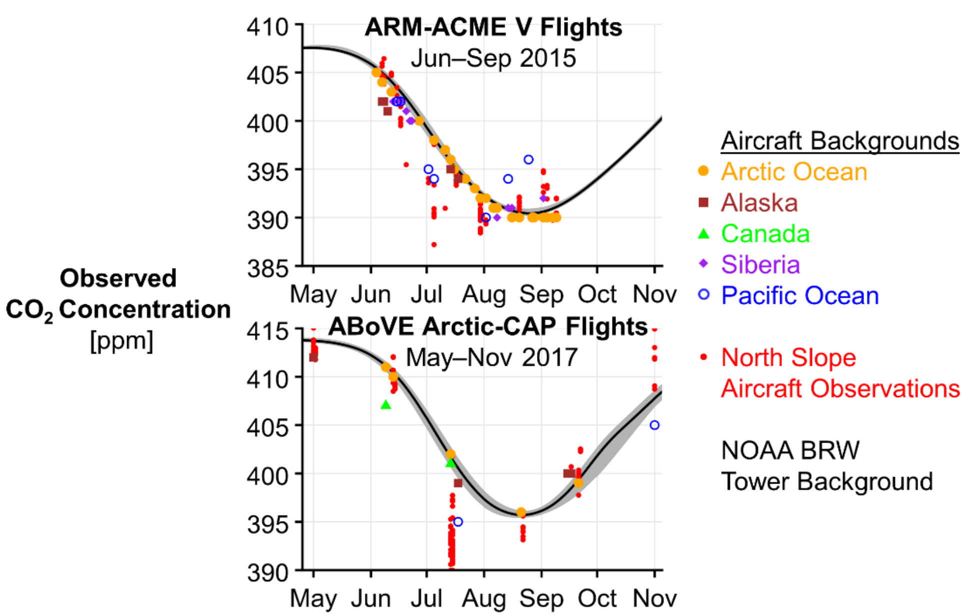

Figure S3. Timeseries of CO_2 background concentration determined using aircraft observations without Alaska North Slope surface influence for the ARM-ACME V and ABoVE Arctic-CAP flight campaigns. Various colored symbols indicate the background source region. Red dots show aircraft observations used in model evaluation (Figs. 2a–2b, 2d, S8). NOAA BRW tower ocean sector background (median and uncertainty) also shown as in Fig. S2.

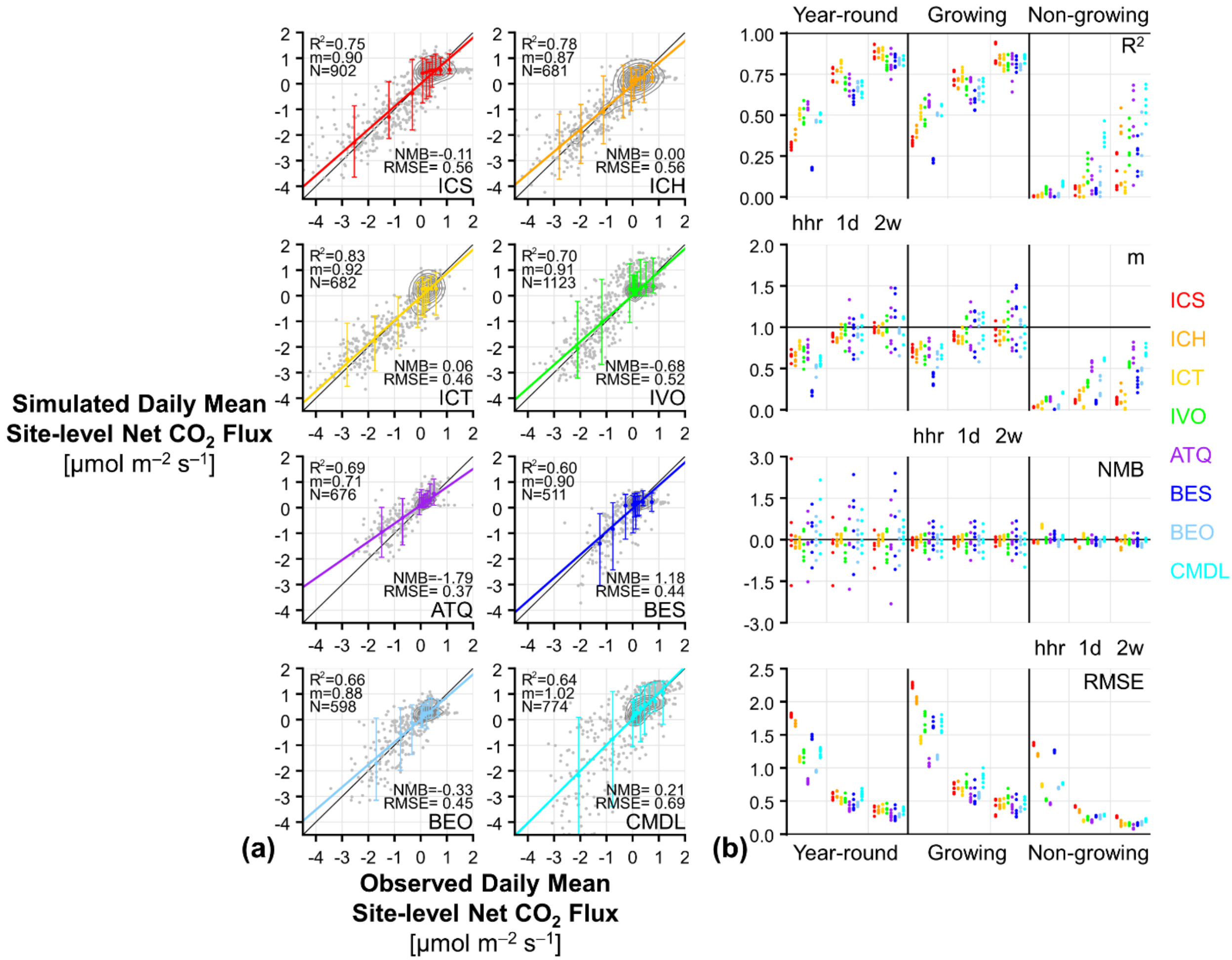

Figure S4. (a) Comparison of observed and simulated TPVRM daily mean site-level net CO_2 flux (gray dots) for 2013-2017 at eddy flux measurement sites used to determine TVPRM parameters, where TVPRM is driven by ERA5 meteorology and the CSIF SIF product. In each comparison, contours contain 10% of all points, and vertical bars indicate 95% distribution and colored dots indicate median of simulated values within each 10% bin of observations. Statistics shown for each comparison include coefficient of determination of all points (R^2), slope (m) determined by ordinary least squares using median of each 10% bin of observations, number of points (N), normalized mean bias (NMB) of all points, and root-mean-square error (RMSE) of all points. 1:1 line shown in dark gray. **(b)** Comparison statistics as in **(a)** for various TVPRM environmental drivers (six combinations of NARR and ERA5 meteorology with GOME-2, GOSIF, and CSIF SIF) over various averaging lengths (half-hour (hhr), one day (1d), two weeks (2w)) for various timeframes (year-round, growing season, non-growing season). Optimal value for each statistic shown as horizontal black line.

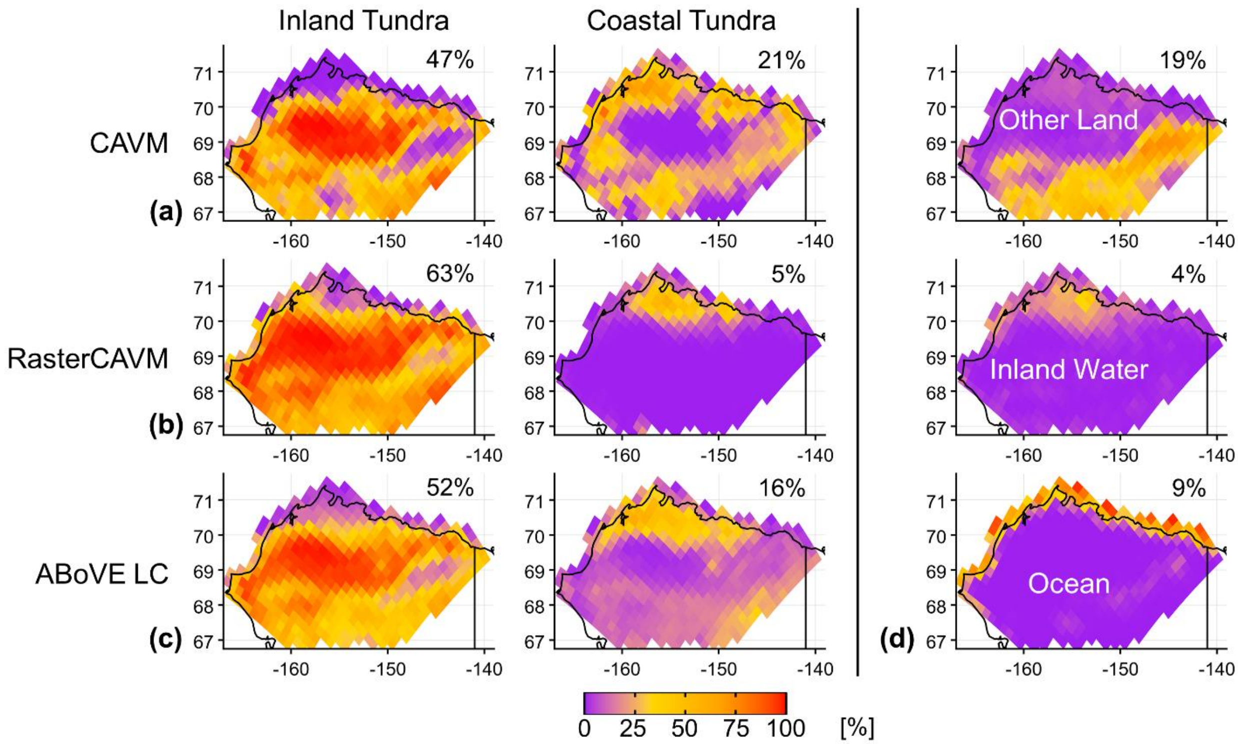

Figure S5. Spatial distribution of **(a)–(c)** inland and coastal tundra classification for (a) CAVM, (b) RasterCAVM, and (c) ABoVE LC vegetation maps and (d) other land, inland water, and ocean classifications for ABoVE LC vegetation map. Percentage of Alaska North Slope domain represented by each classification in upper right.

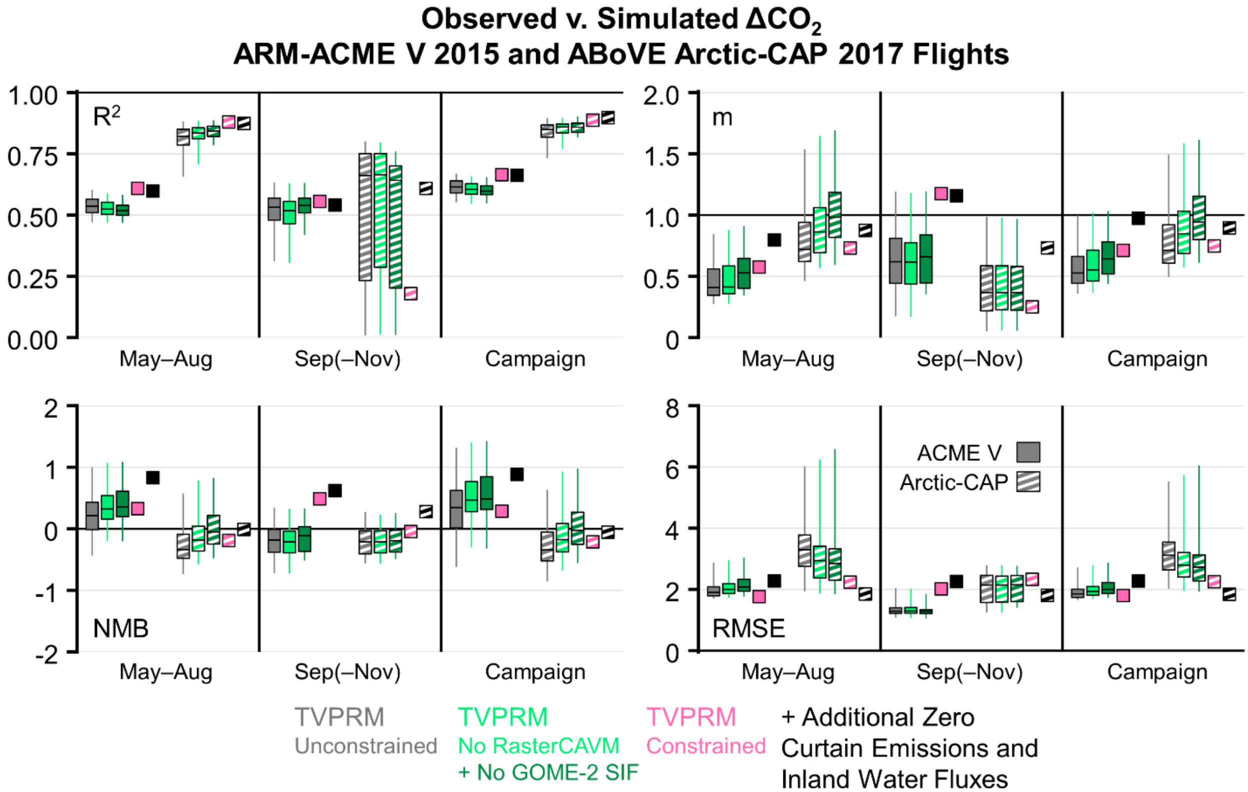

Figure S6. Statistics for comparison of observed and simulated ΔCO_2 during the ARM-ACME V and (solid fill) ABoVE Arctic-CAP (striped fill) aircraft campaign for various segments of the TVPRM ensemble (see legend) for various timeframes (growing season (May–Aug), early cold season (Sep(–Nov, ABoVE Arctic-CAP only)), entire campaign). Each comparison includes the coefficient of determination of all points (R^2), slope (m) determined by ordinary least squares using median of each 10% bin of observations, normalized mean bias (NMB) of all points, and root-mean-square error (RMSE) of all points. Optimal value for each statistic shown as horizontal black line.

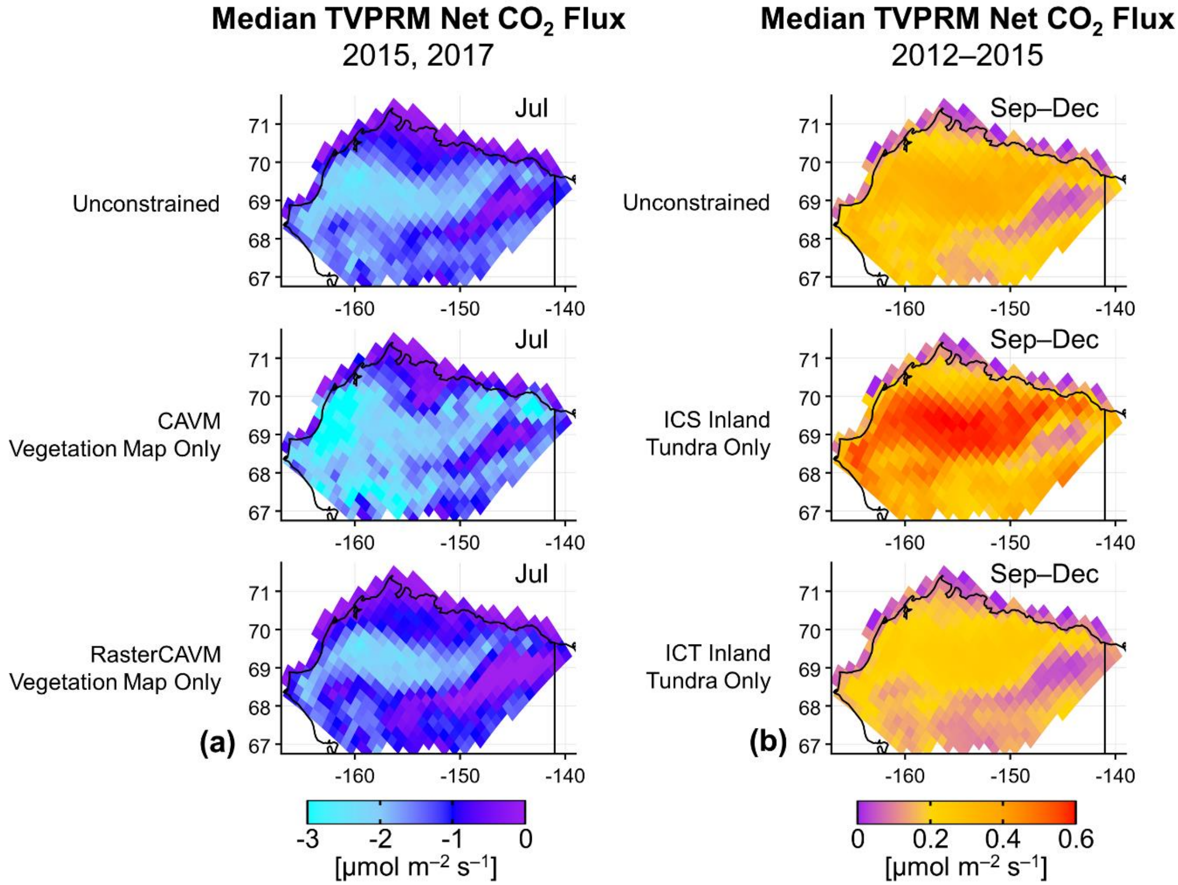

Figure S7. (a) Spatial distribution of mean July TVPRM net CO_2 flux for 2015 and 2017. Median value is shown for multiple TPVRM members using all vegetation maps (top), only CAVM vegetation map (middle), and only RasterCAVM vegetation map (bottom). Colors are saturated at –3 µmol m^{-2} s^{-1}. (b) Spatial distribution of mean Sep–Dec TVPRM net CO_2 flux for 2012–2015. Median value is shown for multiple TVPRM members using all inland site parameterizations (top), only ICS inland site parameterization (middle), and only ICT inland site parameterization (bottom). Colors are saturated at 0.6 µmol m^{-2} s^{-1}.

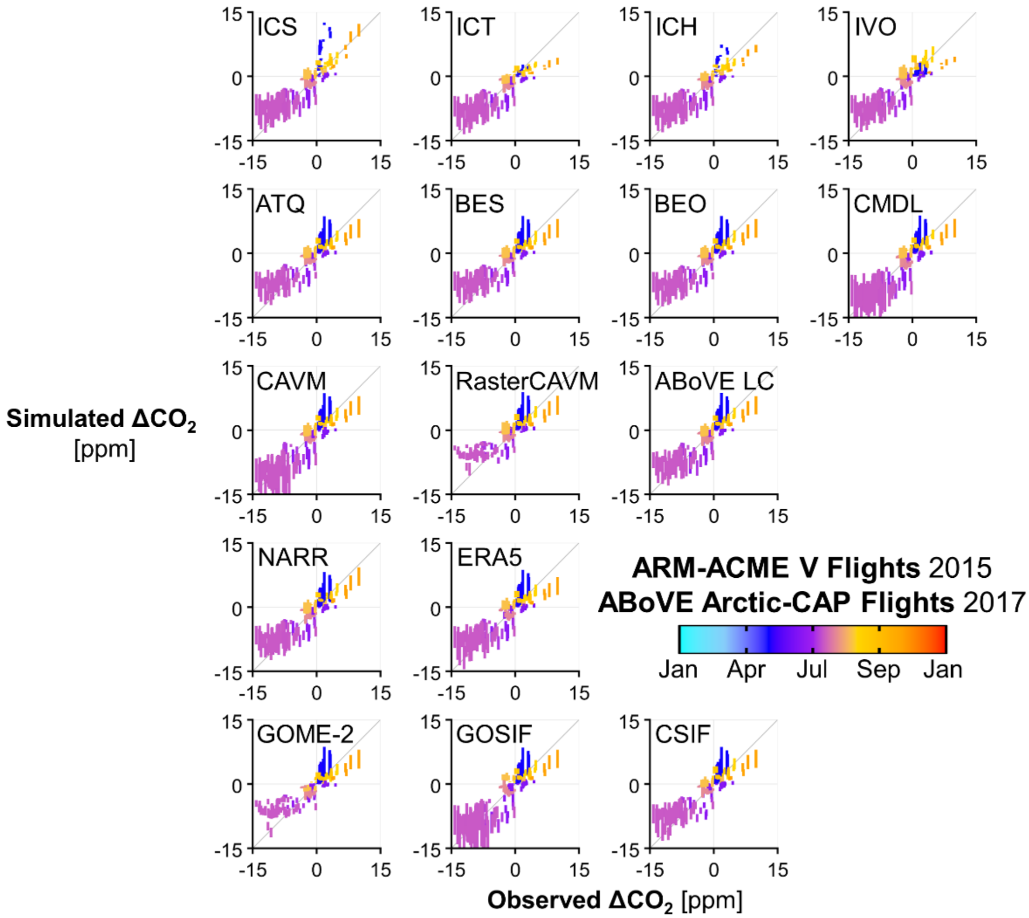

Figure S8. Comparison of vertically binned median observed and TVPRM simulated ΔCO_2 during the ARM-ACME V and ABoVE Arctic-CAP flight campaigns over the Alaska North Slope isolated for each model parameterization or driver. All points colored by day of year. Vertical boxes represent 50% of ΔCO_2 values from remaining TVPRM members from all binned points. 1:1 line shown in dark gray.

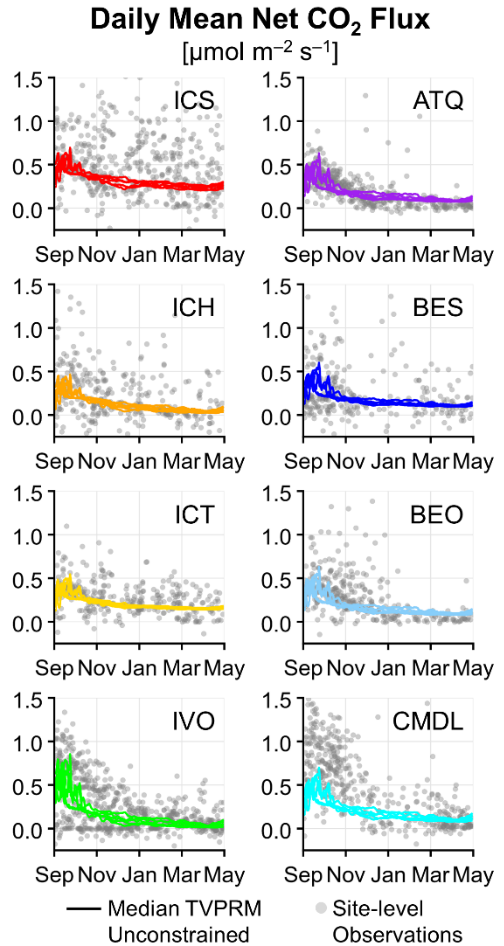

Figure S9. Observed daily mean site-level (grey points) and simulated daily mean Alaska North Slope (colored lines) net CO_2 flux at eight eddy flux sites for cold seasons (Sep–Apr) of 2012–2017. Simulated net CO_2 flux is for the median of all unconstrained TVPRM ensemble members using the observation-derived parameterizations from that eddy flux site.

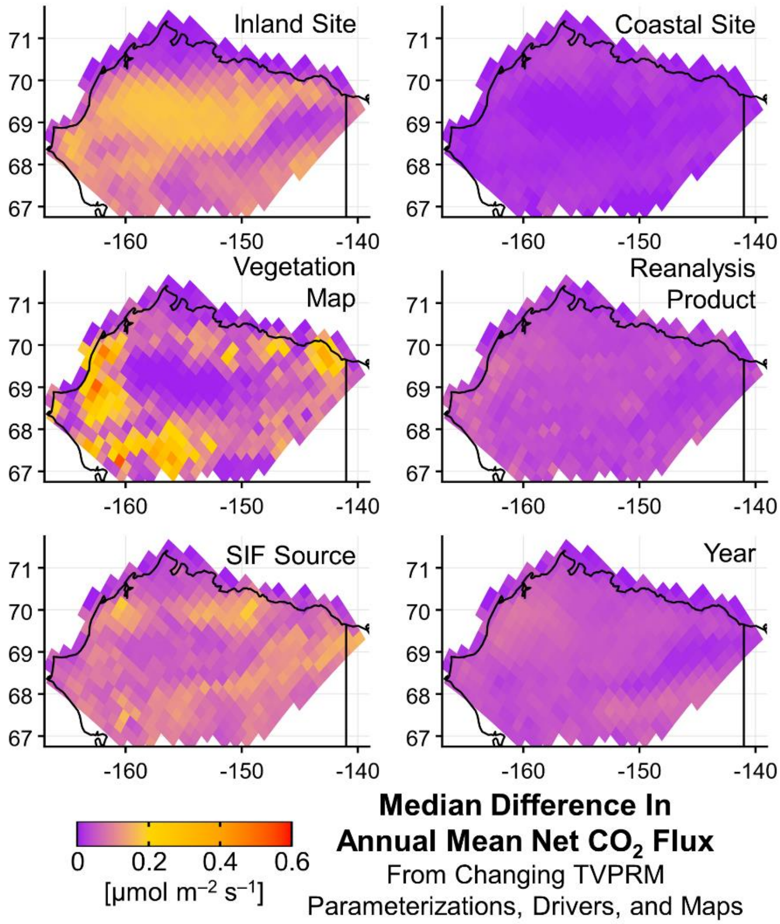

Figure S10. Spatial distribution of median difference in annual mean net CO_2 flux change driven by changing unconstrained TVPRM ensemble site-level parameterizations, environmental drivers, and vegetation distributions for 2012–2017 on the Alaska North Slope. Colors are saturated at 0.6 μmol m^{-2} s^{-1}.

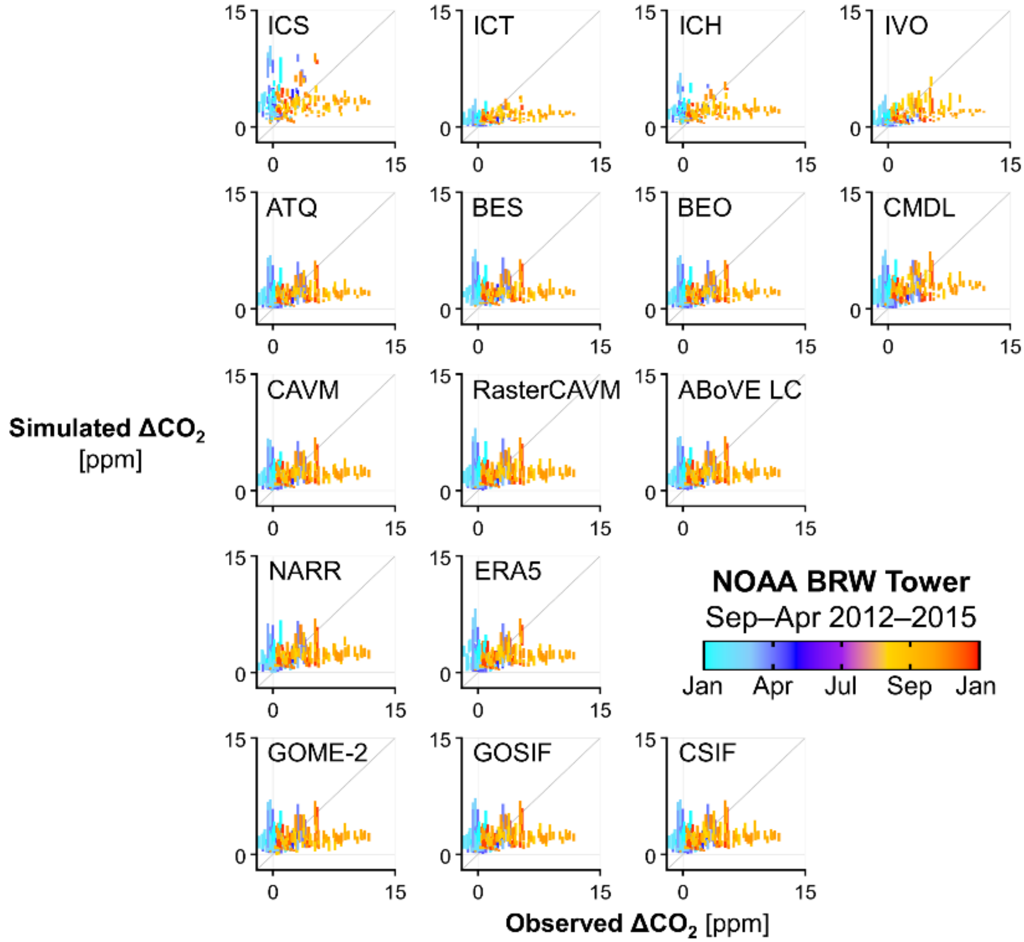

Figure S11. Comparison of hourly cold season (Sep–Apr) observed and TVPRM simulated ΔCO_2 at the NOAA BRW tower isolated for each model parameterization or driver. All points colored by day of year. Vertical boxes represent 50% of ΔCO_2 values from remaining TVPRM members. 1:1 line shown in dark gray.

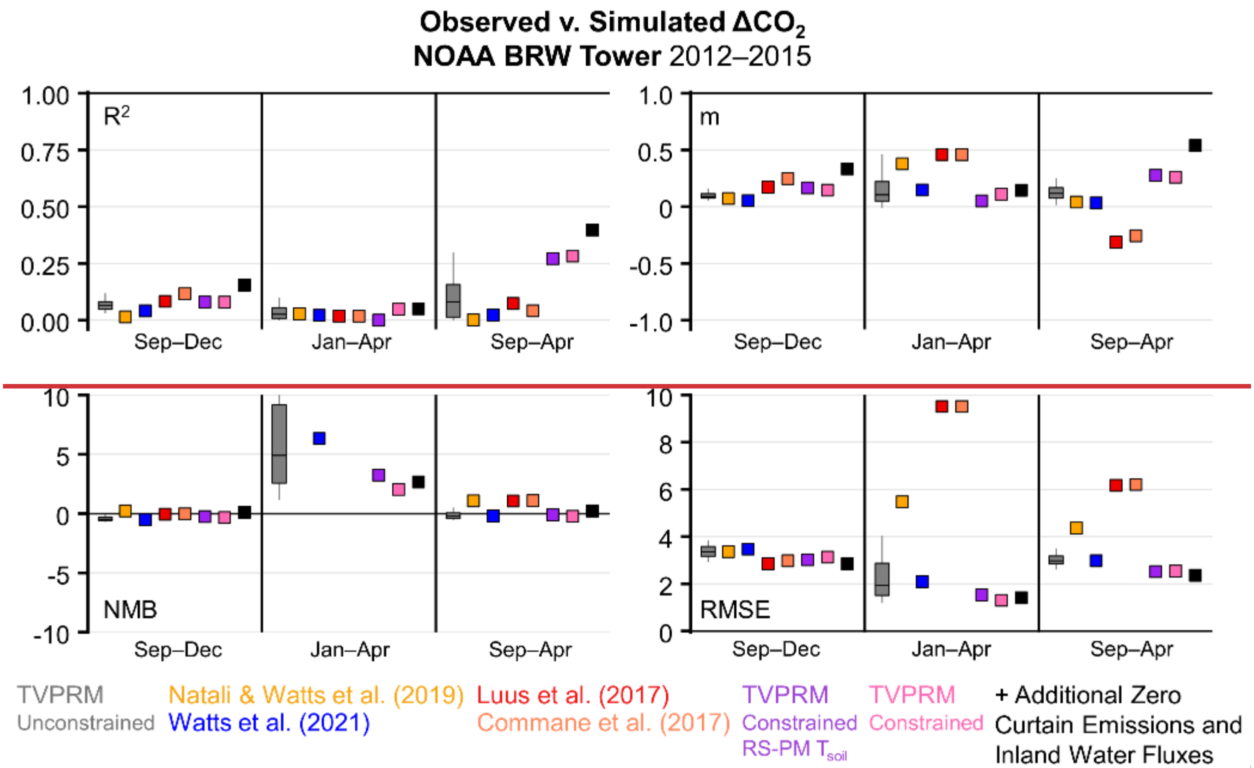
Observed v. Simulated ΔCO2
NOAA BRW Tower 2012–2015
R2
m
NMB
RMSE
Sep–Dec
Jan–Apr
Sep–Apr
TVPRM Unconstrained
Natali & Watts et al. (2019)
Watts et al. (2021)
Luus et al. (2017)
Commane et al. (2017)
TVPRM Constrained RS-PM Tsoil
TVPRM Constrained
+ Additional Zero Curtain Emissions and Inland Water Fluxes

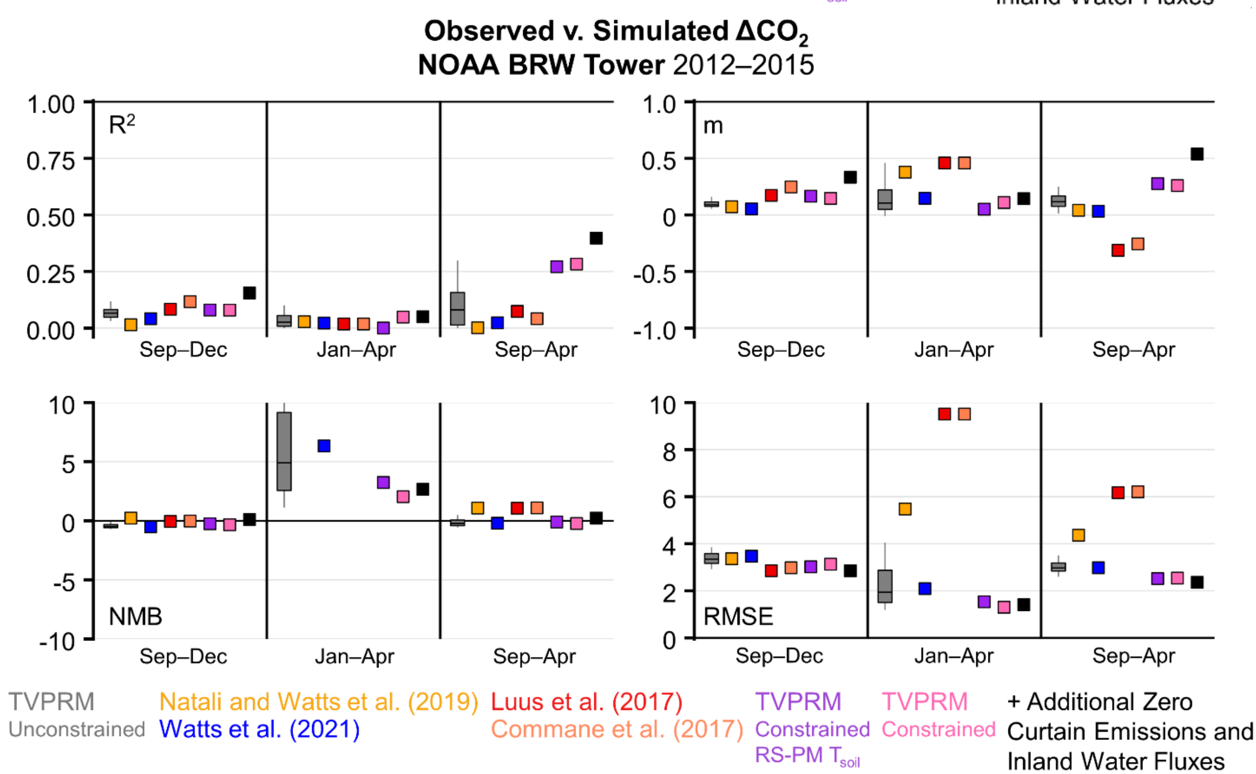
Observed v. Simulated ΔCO2
NOAA BRW Tower 2012–2015
R2
m
NMB
RMSE
Sep–Dec
Jan–Apr
Sep–Apr
TVPRM Unconstrained
Natali and Watts et al. (2019)
Watts et al. (2021)
Luus et al. (2017)
Commane et al. (2017)
TVPRM Constrained RS-PM Tsoil
TVPRM Constrained
+ Additional Zero Curtain Emissions and Inland Water Fluxes

Figure S12. Statistics for comparison of observed and simulated ΔCO_2 at the NOAA BRW tower for various CO_2 flux models (see legend) for various timeframes (early cold season (Sep–Dec), late cold season (Jan–Apr), entire cold season (Sep–Apr)). Each comparison includes the coefficient of determination of all points (R^2), slope (m) determined by ordinary least squares using median of each 10% bin of observations, normalized mean bias (NMB) of all points, and root-mean-square error (RMSE) of all points. Optimal value for each statistic shown as horizontal black line.

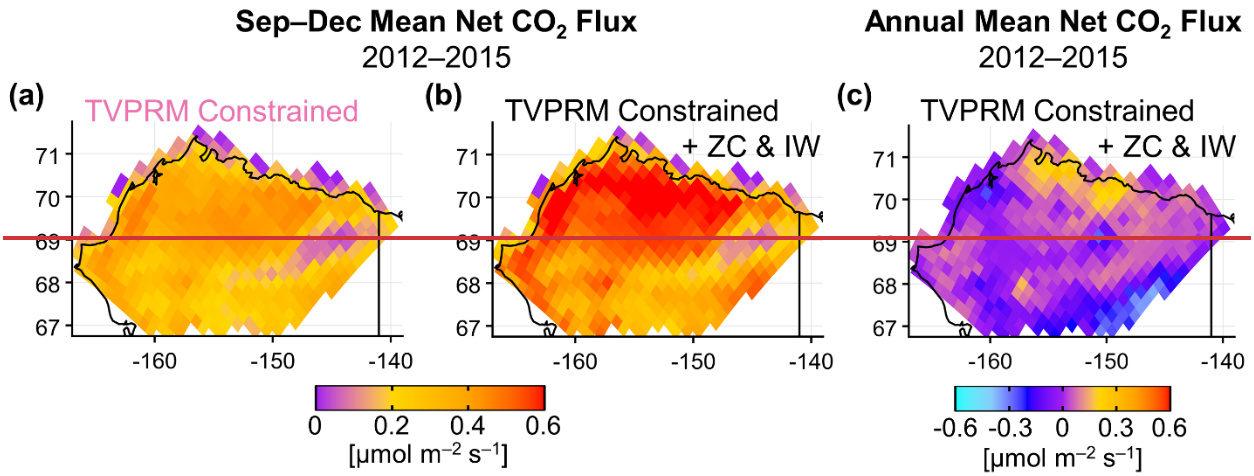

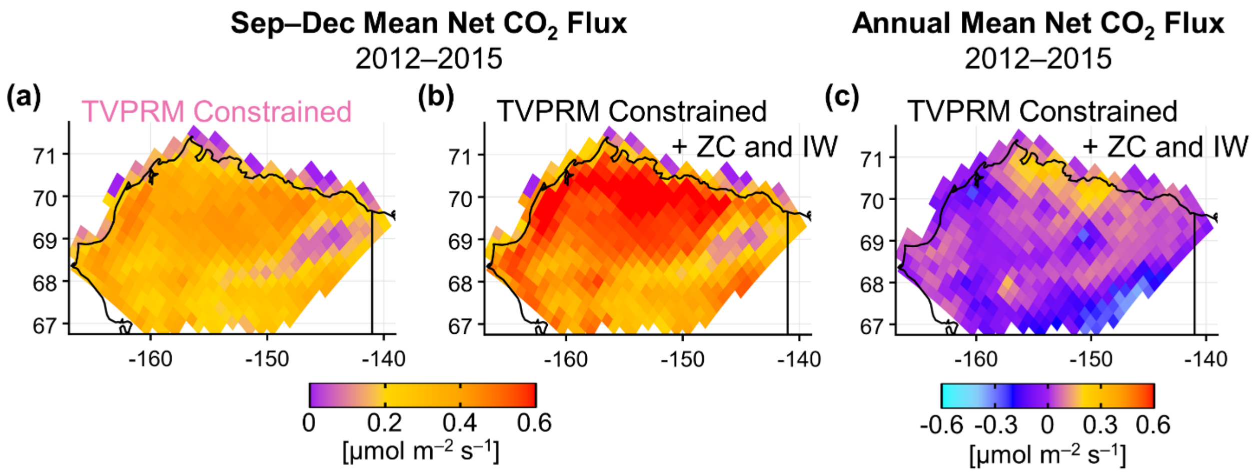

Figure S13. (a)–(b) Spatial distribution of early cold season (Sep–Dec) mean TVPRM net CO_2 flux for 2012–2015 for constrained TVPRM member + additional zero-curtain emissions (ZC) and inland water fluxes (IW). Colors are saturated at 0.6 μmol m^{-2} s^{-1}. (c) Spatial distribution of annual mean constrained TVPRM member + ZC and~~&~~ IW net CO_2 flux for 2012–2015. Colors are saturated at +/–0.6 μmol m^{-2} s^{-1}.

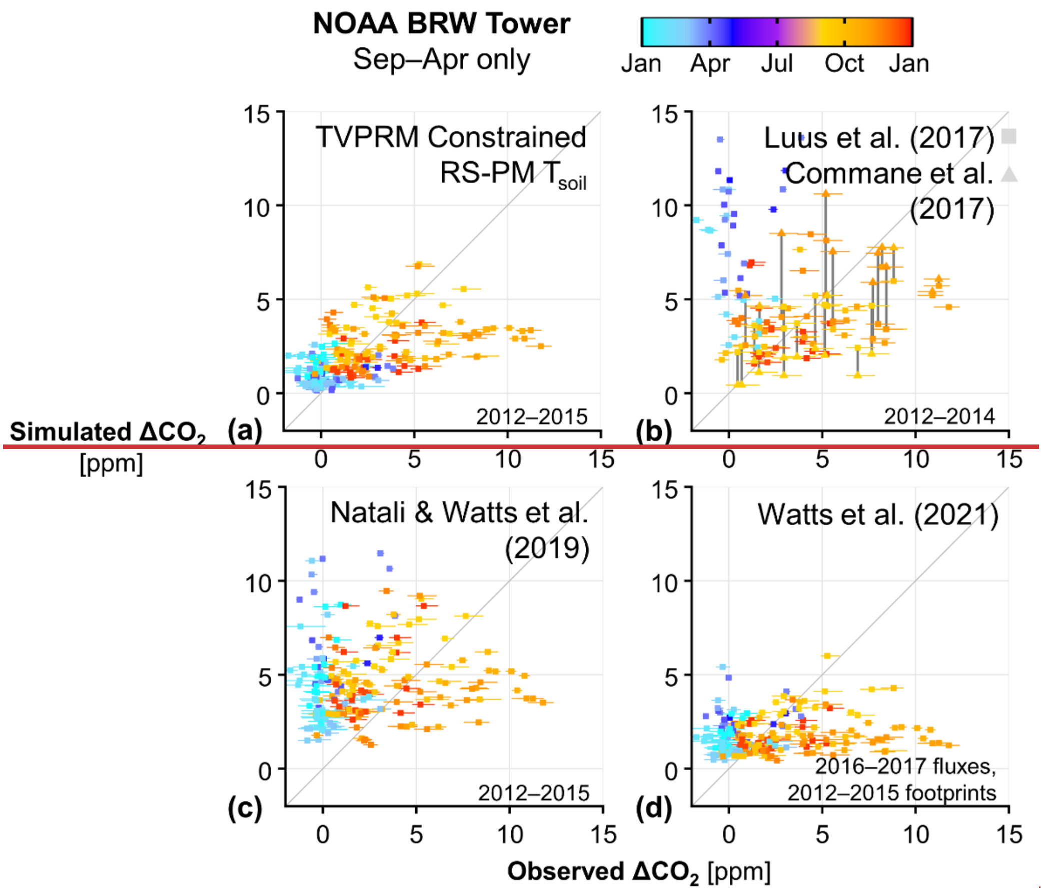
NOAA BRW Tower
Sep–Apr only
Jan Apr Jul Oct Jan
TVPRM Constrained
RS-PM T_{soil}
2012–2015
(a)
Luus et al. (2017)
Commane et al. (2017)
2012–2014
(b)
Natali & Watts et al. (2019)
2012–2015
(c)
Watts et al. (2021)
2016–2017 fluxes, 2012–2015 footprints
(d)
Simulated ΔCO_2 [ppm]
Observed ΔCO_2 [ppm]

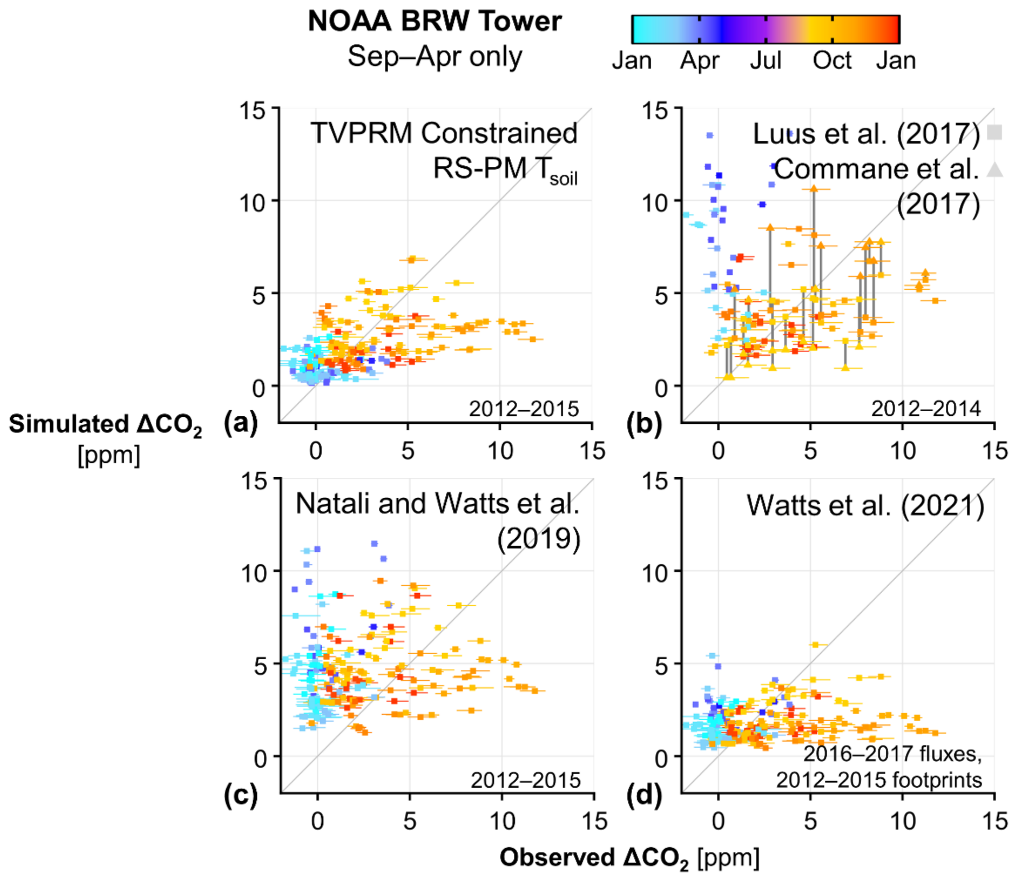

Figure S14. Comparison of hourly cold season (Sep–Apr) observed and simulated ΔCO_2 at the NOAA BRW tower using various CO_2 flux models and timeframes. All points colored by day of year. Horizontal segments indicate range of uncertainty in the BRW tower ocean sector background calculation. For (b), vertical gray bars connect corresponding points in the net CO_2 flux model values from Luus et al. (2017) and Commane et al. (2017). 1:1 line shown in dark gray.

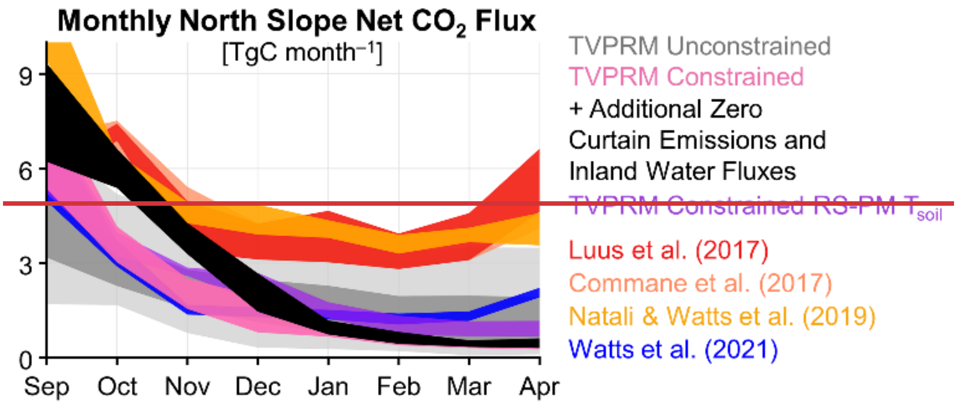

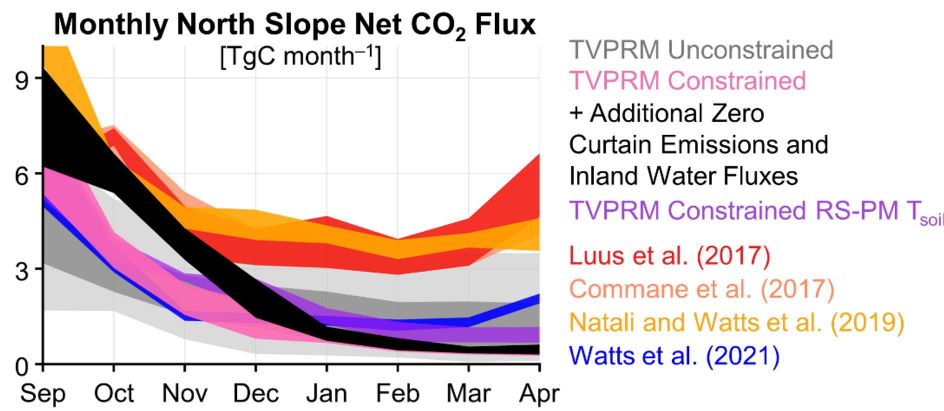

Figure S15. Monthly cold season total Alaska North Slope CO_2 fluxes for various CO_2 flux models shown in Figs. 4 and S14. The net CO_2 fluxes from the TVPRM ensemble and members and from Natali and~~&~~ Watts et al. (2019) show values for 2012–2017, from Luus et al. (2017) and Commane et al. (2017) show 2012–2014, and from Watts et al. (2021) show Sep 2016–Apr 2017. Ribbons represent range of all years, where applicable, except for unconstrained TVPRM ensemble, where dark gray ribbon represents 50% and light gray ribbon represents 95% of CO_2 flux values from all members for 2012–2017. Area of North Slope domain used to calculate regional totals is 3.537×10^5 km^2.

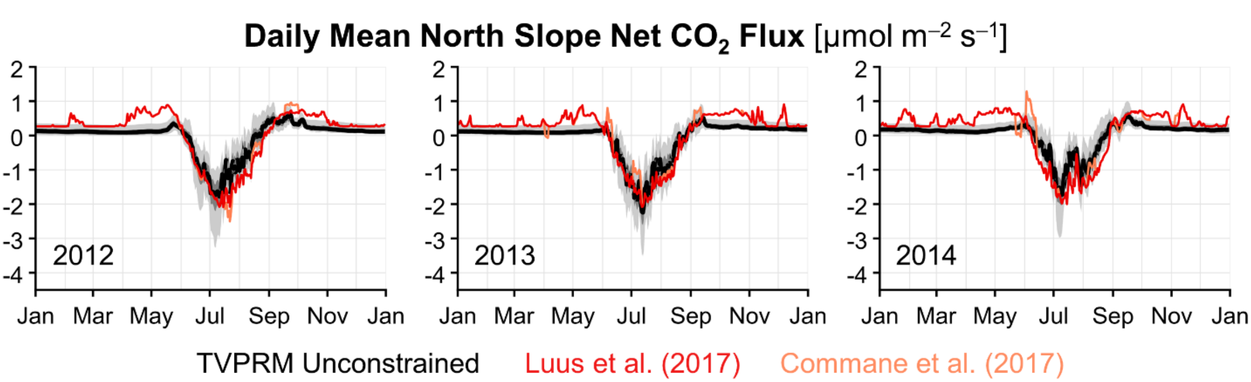

Figure S16. Timeseries of simulated daily mean Alaska North Slope net CO_2 flux for 2012–2014. Black line indicates median, dark gray ribbon represents 50%, and light gray ribbon represents 95% of daily mean net CO_2 flux values from all members of unconstrained TVPRM ensemble. Light red and dark red lines indicate daily mean net CO_2 flux values from Luus et al. (2017) and Commane et al. (2017), respectively.

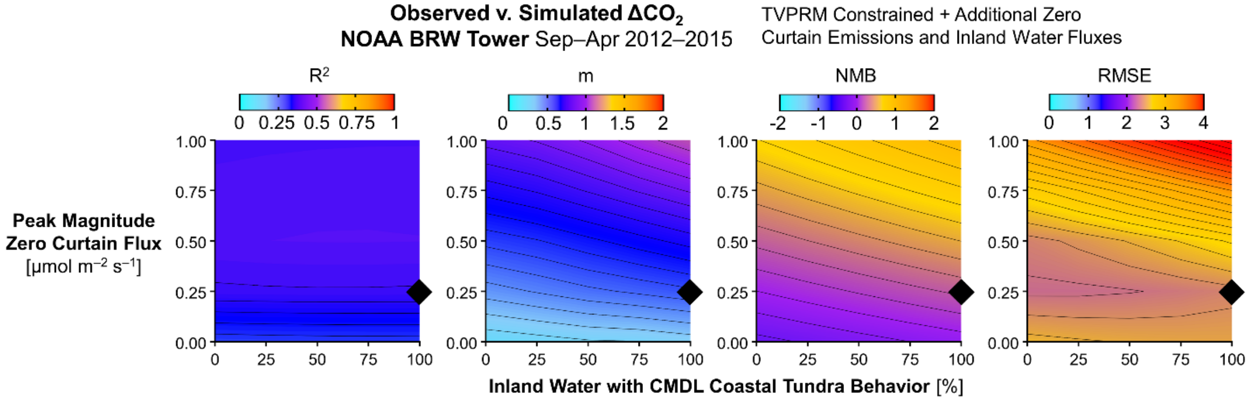

Figure S17. Statistics for comparison of observed and simulated ΔCO_2 at the NOAA BRW tower for the cold season (Sep–Apr) as calculated in Fig. S12. Simulated ΔCO_2 is determined using the constrained TVPRM member with varying amounts of inland water (IW) area represented as CMDL coastal tundra site parameterization (horizontal axis) and additional peak zero curtain (ZC) flux (vertical axis). Black diamonds indicate best performing combination and choice for ZC+IW formulation. Colors are saturated at shown colorbar endpoints.

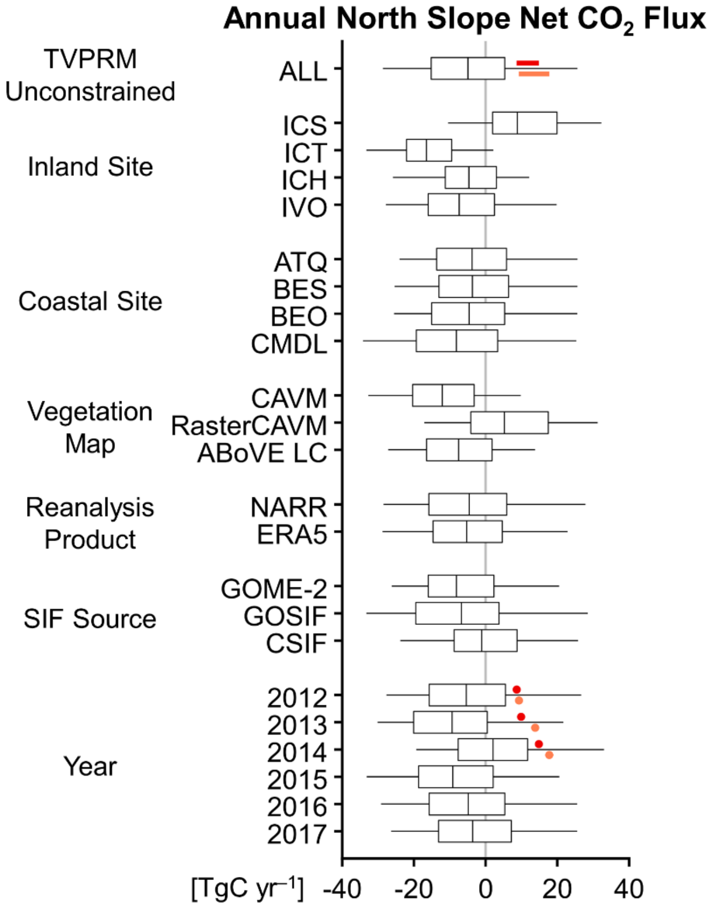

Figure S18. Range of annual North Slope net CO_2 flux from the TVPRM ensemble determined by various ecological parameterizations, environmental drivers, and vegetation distributions for 2012–2017 (black) and from the net CO_2 flux models by Luus et al. (2017) (dark red) and Commane et al. (2017) (light red) for 2012–2014. For each site parameterization or driver, boxes represent 50% and whiskers represent 95% of the net CO_2 flux from all TVPRM members included in that category. Area of North Slope domain used to calculate regional totals is 3.537×10^5 km^2.

Supplemental Tables

Table S1. Annual and seasonal CO2 emission totals from anthropogenic and biomass burning sources and area burned in the Alaska North Slope and all of Alaska for 2012–2017. Annual anthropogenic emissions are from EDGAR, the Emissions Database for Global Atmospheric Research v7.0 (https://edgar.jrc.ec.europa.eu/dataset_ghg70). Monthly biomass burning emissions are from GFED, Global Fire Emissions Database v4 (https://globalfiredata.org/pages/data/#emissions). Area burned data is from the Alaska Interagency Coordination Center via UAF SNAP tool (https://snap.uaf.edu/tools/daily-fire-tally).

Dataset	Domain	2012	2013	2014	2015	2016	2017	Jun-Sep 2015	May-Nov 2017
Anthropogenic CO_2 Emissions [TgC]	North Slope	0.73	0.74	0.78	0.82	0.77	0.79		
	Alaska	7.7	7.7	7.8	8.2	8.3	8.4		
Biomass Burning CO_2 Emissions [TgC]	North Slope	0.23	0.12	0.00	0.12	0.34	0.07	0.12	0.07
	Alaska	0.97	6.7	1.7	28	1.9	7.6	28	7.6
Area Burned [million acres]	Alaska		1.3		5.1	0.50	0.65	5.1	0.65

Table S2~~1~~. Alaska North Slope eddy covariance flux sites measuring net CO_2 flux for 2013-2017 used in this study. See Figs. 1c and S1 for map of site locations. ATQ, BES, BEO, CMDL, and IVO are further described by Zona et al. (2016) and Arndt et al. (2020). ICS, ICT, and ICH are further described by Euskirchen et al. (2012) and Euskirchen et al. (2017).

Site ID	Name	Ecosystem / TVPRM Group	Vegetation	Data Coverage (month/year)
ATQ	Atqasuk	Wet polygonised tundra / coastal	Water sedge, dwarf shrub	09/2013–11/2013, 02/2014–10/2014, 02/2015–01/2016, 07/2016, 09/2016–04/2017, 06/2017–07/2017, 09/2017–12/2017
BES	Barrow Biocomplexity Experiment, South	Wetland tundra / coastal	Sedge, moss	07/2013–11/2014, 02/2015–10/2015, 07/2016–01/2017, 05/2017–07/2017
BEO	Barrow Environmental Observatory	Wet polygonised tundra / coastal	Graminoid grass, sedge	09/2013–01/2015, 06/2015–02/2016, 04/2016–07/2016, 07/2017–12/2017
CMDL	Barrow Climate Monitoring and Diagnostics Laboratory	Moist tundra / coastal	Graminoid grass, lichen	10/2013–10/2014, 02/2015–05/2015, 07/2015–09/2017, 11/2017–12/2017
IVO	Ivotuk	Tussock tundra / inland	Tussock-forming sedge, moss	06/2013–11/2014, 02/2015–12/2017
ICS	Imnavait Creek Wet Sedge	Wet sedge tundra / inland	Water sedge, swarf deciduous shrub, moss	01/2013–12/2017

ICH	Imnavait Creek Heath Tundra	Dry heath tundra / inland	Dwarf evergreen shrub, deciduous shrub, lichen	01/2013–12/2016, 03/2017–12/2017
ICT	Imnavait Creek Tussock Tundra	Moist acidic tussock tundra / inland	Tussock-forming sedge, deciduous dwarf shrub, evergreen dwarf shrub	01/2013–12/2014, 04/2015–12/2017

Table S3~~2~~. Previously developed CO_2 flux models used in this study.

Model ID	Model Resolution / Years	Model Details
Luus et al. (2017)	1/4° × 1/6° spatial, 3 hourly temporal / 2012–2014	Similar to TPVRM, using monthly SIF values and alternative eddy flux sites and methods to calculate variable parameters. Accounts for both boreal and tundra ecosystems.
Commane et al. (2017)	0.5° spatial, 3 hourly temporal / 2012–2014	Luus et al. (2017) optimized based on observations from the Carbon in Arctic Reservoirs Vulnerability Experiment (CARVE) flight campaign. Reverts to Luus et al. (2017) for time periods without flights.
Natali and~~&~~ Watts et al. (2019)	25 km spatial, monthly temporal / 2012–2015	Synthesis of pan-Arctic winter in situ CO_2 flux observations and environmental drivers using boosted regression tree machine learning.
Watts et al. (2021)	300 m spatial, monthly temporal / 2016–2017	Integration of Alaskan and northwest Canadian belowground CO_2 flux observations and satellite data using random forest machine learning.

Table S4~~3~~. Reanalysis meteorology products for 2012-2017 used by TVPRM in this study.

Met ID	Product Name	Product Resolution	Product Variable used in TVPRM		
			T_a	T_s	PAR
NARR	NOAA North American Regional Reanalysis Mesinger et al. (2006)	~30 km spatial, 3 hourly temporal	air.2m	tsoil (10 cm)	dswrf
ERA5	ECMWF Reanalysis, fifth generation Hersbach et al. (2020)	~31 km spatial, hourly temporal	t2m	stl2 (7–28 cm)	ssrd

Table S5~~4~~. SIF products for 2012-2017 used by TVPRM in this study.

SIF ID	Product Name	Product Resolution	Product Details
GOME-2	Interpolated GOME-2 SIF (created for this study) [GOME-2: Global Ozone Monitoring Experiment-2]	0.01° latitudinal, daily temporal	Discrete GOME-2 SIF v27 retrievals (Joiner et al., 2016), normalized by solar zenith angle, averaged by center point into overlapping 0.5° latitudinal bins across the North Slope domain. Temporal interpolation within each bin and latitudinal interpolation across bins applied using loess fit smoothing.
GOSIF	Global 'OCO-2' SIF (Li and Xiao, 2019) [OCO-2: Orbiting Carbon Observatory-2]	0.05° spatial, 8 day temporal	Aggregated OCO-2 soundings combined with MODIS enhanced vegetation index and MERRA-2 PAR, vapor pressure deficit, and air temperature to create a higher resolution gridded SIF product using multivariate linear regression.
CSIF	Contiguous SIF (Zhang et al., 2018)	0.05° spatial, 4 day temporal	Aggregated OCO-2 soundings combined with MODIS surface reflectance to create a higher resolution gridded SIF product using a neural network.

Table S6~~5~~. Vegetation maps used by TVPRM in this study.

Map ID	Map Name	Map Resolution / Year	Map Classification Details
CAVM	Circumpolar Arctic Vegetation Map (Walker et al., 2005)	14 km polygons, 8 km linear features / satellite data from 1993 and 1995, developed in 2003	15 classification units based on plant growth forms, roughly separated by summer temperature and soil moisture. Polygon classification from combination of satellite, vegetation, temperature, topographic, and geologic data.
RasterCAVM	Raster version of CAVM (Raynolds et al., 2019)	1 km spatial / satellite data as in CAVM, additional data from 2000–2009	Classification as in CAVM, redistributed at higher resolution based on unsupervised classification using satellite and elevation data.
ABoVE LC	Landsat-derived Annual Dominant Land Cover across ABoVE Core Domain (Wang et al., 2020)	30 m spatial / 2014 [ABoVE: Arctic-Boreal Vulnerability Experiment]	15 classification units based on semi-supervised classification using satellite, climate, and topographic data

Table S7. Alaska North Slope growing season (May–Aug) net CO_2 flux by component for the TVPRM Constrained + ZC and IW scenario for 2012–2017.

Flux Component	2012	2013	2014	2015	2016	2017
R_{soil} [TgC]	18	16	17	18	18	17
R_{plant} [TgC]	33	30	28	33	33	30
GPP [TgC]	69	71	60	77	71	68
NEE [TgC]	-18	-25	-15	-25	-19	-21

Table S8. Alaska North Slope growing season (May-Aug) mean TVPRM drivers used in the TVPRM Constrained + ZC and IW scenario for 2012–2017, where the mean uses model gridboxes with a total ABoVE LC ocean and other land fraction of less than 0.5 (see Fig. S5).

Driver	2012	2013	2014	2015	2016	2017
NARR Ta [°C]	7.4	6.6	6.2	7.5	7.8	6.8
NARR T_{scale} [0-1]	0.67	0.61	0.58	0.65	0.65	0.58
NARR Ts [°C]	2.6	0.68	1.3	2.4	2.7	1.5
NARR PAR [μmol photon m^{-2} s^{-1}]	484	478	466	495	497	507
CSIF SIF product [mW m^{-2} nm^{-1} sr^{-1}]	0.17	0.18	0.16	0.19	0.18	0.18

Table S9. Alaska North Slope growing season (May-Aug) mean additional select NARR Variables for 2012–2017, where the mean uses model gridboxes with a total ABoVE LC ocean and other land fraction of less than 0.5 (see Fig. S5).

Variable	2012	2013	2014	2015	2016	2017
NARR 3hr accumulated precipitation [kg m^{-2}]	0.19	0.21	0.20	0.15	0.16	0.16
NARR soil moisture content [kg m^{-2}]	688	745	755	747	733	734
NARR snow depth [m]	0.046	0.076	0.032	0.030	0.026	0.040
NARR snow cover fraction [0-1]	0.15	0.20	0.16	0.12	0.11	0.17
NARR snow depth [m] during proceeding Sep-Apr	0.42	0.35	0.36	0.38	0.35	0.38
NARR snow cover fraction [0-1] during proceeding Sep-Apr	0.81	0.78	0.79	0.83	0.87	0.78

Supplemental References

Arndt, K. A., Lipson, D. A., Hashemi, J., Oechel, W. C., and Zona, D.: Snow melt stimulates ecosystem respiration in Arctic ecosystems, Global Change Biol., 26, 5042–5051, https://doi.org/10.1111/gcb.15193, 2020.

Commane, R., Lindaas, J., Benmergui, J., Luus, K. A., Chang, R. Y.-W., Daube, B. C., Euskirchen, E. S., Henderson, J. M., Karion, A., Miller, J. B., Miller, S. M., Parazoo, N. C., Randerson, J. T., Sweeney, C., Tans, P., Thoning, K., Veraverbeke, S., Miller, C. E., and Wofsy, S. C.: Carbon dioxide sources from Alaska driven by increasing early winter respiration from Arctic tundra, PNAS, 114, 5361–5366, https://doi.org/10.1073/pnas.1618567114, 2017.

Euskirchen, E. S., Bret-Harte, M. S., Scott, G. J., Edgar, C., and Shaver, G. R.: Seasonal patterns of carbon dioxide and water fluxes in three representative tundra ecosystems in northern Alaska, Ecosphere, 3, art4, https://doi.org/10.1890/ES11-00202.1, 2012.

Euskirchen, E. S., Bret-Harte, M. S., Shaver, G. R., Edgar, C. W., and Romanovsky, V. E.: Long-Term Release of Carbon Dioxide from Arctic Tundra Ecosystems in Alaska, Ecosystems, 20, 960–974, https://doi.org/10.1007/s10021-016-0085-9, 2017.

Hersbach, H., Bell, B., Berrisford, P., Hirahara, S., Horányi, A., Muñoz-Sabater, J., Nicolas, J., Peubey, C., Radu, R., Schepers, D., Simmons, A., Soci, C., Abdalla, S., Abellan, X., Balsamo, G., Bechtold, P., Biavati, G., Bidlot, J., Bonavita, M., Chiara, G. D., Dahlgren, P., Dee, D., Diamantakis, M., Dragani, R., Flemming, J., Forbes, R., Fuentes, M., Geer, A., Haimberger, L., Healy, S., Hogan, R. J., Hólm, E., Janisková, M., Keeley, S., Laloyaux, P., Lopez, P., Lupu, C., Radnoti, G., Rosnay, P. de, Rozum, I., Vamborg, F., Villaume, S., and Thépaut, J.-N.: The ERA5 global reanalysis, Q. J. Roy. Meteorol. Soc., 146, 1999–2049, https://doi.org/10.1002/qj.3803, 2020.

Joiner, J., Yoshida, Y., Guanter, L., and Middleton, E. M.: New methods for the retrieval of chlorophyll red fluorescence from hyperspectral satellite instruments: simulations and application to GOME-2 and SCIAMACHY, Atmos. Meas. Tech., 9, 3939–3967, https://doi.org/10.5194/amt-9-3939-2016, 2016.

Li, X. and Xiao, J.: A Global, 0.05-Degree Product of Solar-Induced Chlorophyll Fluorescence Derived from OCO-2, MODIS, and Reanalysis Data, Remote Sens., 11, 517, https://doi.org/10.3390/rs11050517, 2019.

Luus, K. A., Commane, R., Parazoo, N. C., Benmergui, J., Euskirchen, E. S., Frankenberg, C., Joiner, J., Lindaas, J., Miller, C. E., Oechel, W. C., Zona, D., Wofsy, S., and Lin, J. C.: Tundra photosynthesis captured by satellite-observed solar-induced chlorophyll fluorescence, Geophys. Res. Lett., 44, 2016GL070842, https://doi.org/10.1002/2016GL070842, 2017.

Mesinger, F., DiMego, G., Kalnay, E., Mitchell, K., Shafran, P. C., Ebisuzaki, W., Jović, D., Woollen, J., Rogers, E., Berbery, E. H., Ek, M. B., Fan, Y., Grumbine, R., Higgins, W., Li, H., Lin, Y., Manikin, G., Parrish, D., and Shi, W.: North American Regional Reanalysis, B. Am. Meteorol. Soc., 87, 343–360, https://doi.org/10.1175/BAMS-87-3-343, 2006.

Natali, S. M., Watts, J. D., Rogers, B. M., Potter, S., Ludwig, S. M., Selbmann, A.-K., Sullivan, P. F., Abbott, B. W., Arndt, K. A., Birch, L., Björkman, M. P., Bloom, A. A., Celis, G., Christensen, T. R., Christiansen, C. T., Commane, R., Cooper, E. J., Crill, P., Czimczik, C., Davydov, S., Du, J., Egan, J. E., Elberling, B., Euskirchen, E. S., Friborg, T., Genet, H., Göckede, M., Goodrich, J. P., Grogan, P., Helbig, M., Jafarov, E. E., Jastrow, J. D., Kalhori, A. A. M., Kim, Y., Kimball, J. S., Kutzbach, L., Lara, M. J., Larsen, K. S., Lee, B.-Y., Liu, Z., Loranty, M. M., Lund, M., Lupascu, M., Madani, N., Malhotra, A., Matamala, R., McFarland, J., McGuire, A. D., Michelsen, A., Minions, C., Oechel, W. C., Olefeldt, D., Parmentier, F.-J. W., Pirk, N., Poulter, B., Quinton, W., Rezanezhad, F., Risk, D., Sachs, T., Schaefer, K., Schmidt, N. M., Schuur, E. A. G., Semenchuk, P. R., Shaver, G., Sonnentag, O., Starr, G., Treat, C. C., Waldrop, M. P., Wang, Y., Welker, J., Wille, C., Xu, X., Zhang, Z., Zhuang, Q., and Zona, D.: Large loss of CO 2 in winter observed across the northern permafrost region, Nat. Clim. Change, 9, 852–857, https://doi.org/10.1038/s41558-019-0592-8, 2019.

Raynolds, M. K., Walker, D. A., Balser, A., Bay, C., Campbell, M., Cherosov, M. M., Daniëls, F. J. A., Eidesen, P. B., Ermokhina, K. A., Frost, G. V., Jedrzejek, B., Jorgenson, M. T., Kennedy, B. E., Kholod, S. S., Lavrinenko, I. A., Lavrinenko, O. V., Magnússon, B., Matveyeva, N. V., Metúsalemsson, S., Nilsen, L., Olthof, I., Pospelov, I. N., Pospelova, E. B., Pouliot, D., Razzhivin, V., Schaepman-Strub, G., Šibík, J., Telyatnikov, M. Yu., and Troeva, E.: A raster version of the Circumpolar Arctic Vegetation Map (CAVM), Remote Sens. Environ., 232, 111297, https://doi.org/10.1016/j.rse.2019.111297, 2019.

Walker, D. A., Raynolds, M. K., Daniëls, F. J. A., Einarsson, E., Elvebakk, A., Gould, W. A., Katenin, A. E., Kholod, S. S., Markon, C. J., Melnikov, E. S., Moskalenko, N. G., Talbot, S. S., Yurtsev, B. A. (†), and Team, T. other members of the C.: The Circumpolar Arctic vegetation map, J. Veg. Sci., 16, 267–282, https://doi.org/10.1111/j.1654-1103.2005.tb02365.x, 2005.

Wang, J. A., Sulla-Menashe, D., Woodcock, C. E., Sonnentag, O., Keeling, R. F., and Friedl, M. A.: Extensive land cover change across Arctic–Boreal Northwestern North America from disturbance and climate forcing, Global Change Biol., 26, 807–822, https://doi.org/10.1111/gcb.14804, 2020.

Watts, J. D., Natali, S. M., Minions, C., Risk, D., Arndt, K., Zona, D., Euskirchen, E. S., Rocha, A. V., Sonnentag, O., Helbig, M., Kalhori, A., Oechel, W., Ikawa, H., Ueyama, M., Suzuki, R., Kobayashi, H., Celis, G., Schuur, E. A. G., Humphreys, E., Kim, Y., Lee, B.-Y., Goetz, S., Madani, N., Schiferl, L. D., Commane, R., Kimball, J. S., Liu, Z., Torn, M. S., Potter, S., Wang, J. A., Jorgenson, M. T., Xiao, J., Li, X., and Edgar, C.: Soil respiration strongly offsets carbon uptake in Alaska and Northwest Canada, Environ. Res. Lett., 16, 084051, https://doi.org/10.1088/1748-9326/ac1222, 2021.

Yi, Y., Kimball, J. S., Chen, R. H., Moghaddam, M., Reichle, R. H., Mishra, U., Zona, D., and Oechel, W. C.: Characterizing permafrost active layer dynamics and sensitivity to landscape spatial heterogeneity in Alaska, Cryosphere, 12, 145–161, https://doi.org/10.5194/tc-12-145-2018, 2018.

Yi, Y., Kimball, J. S., Chen, R. H., Moghaddam, M., and Miller, C. E.: Sensitivity of active-layer freezing process to snow cover in Arctic Alaska, Cryosphere, 13, 197–218, https://doi.org/10.5194/tc-13-197-2019, 2019.

Zhang, Y., Joiner, J., Alemohammad, S. H., Zhou, S., and Gentine, P.: A global spatially contiguous solar-induced fluorescence (CSIF) dataset using neural networks, Biogeosciences, 15, 5779–5800, https://doi.org/10.5194/bg-15-5779-2018, 2018.

Zona, D., Gioli, B., Commane, R., Lindaas, J., Wofsy, S. C., Miller, C. E., Dinardo, S. J., Dengel, S., Sweeney, C., Karion, A., Chang, R. Y.-W., Henderson, J. M., Murphy, P. C., Goodrich, J. P., Moreaux, V., Liljedahl, A., Watts, J. D., Kimball, J. S., Lipson, D. A., and Oechel, W. C.: Cold season emissions dominate the Arctic tundra methane budget, PNAS, 113, 40–45, https://doi.org/10.1073/pnas.1516017113, 2016.